DIELECTRIC SHIMMING

EXPLOITING DIELECTRIC INTERACTIONS IN HIGH FIELD MRI

Wyger M. Brink

Colophon

Cover design: Maarten den Breeijen
Printed by: Gildeprint Drukkerijen, The Netherlands

DIELECTRIC SHIMMING

EXPLOITING DIELECTRIC INTERACTIONS IN HIGH FIELD MRI

Proefschrift

ter verkrijging van
de graad van Doctor aan de Universiteit Leiden,
op gezag van Rector Magnificus prof. mr. C.J.J.M. Stolker,
volgens besluit van het College voor Promoties
te verdedigen op woensdag 27 januari 2016
klokke 13.45 uur

door

Wyger Maurits Brink

geboren te Berghem
in 1987

Promotor:	Prof. dr. A.G. Webb
Copromotor:	Prof. dr. P. Börnert
Oppositiecommissie:	Prof. dr. C.M. Collins (NYU School of Medicine, USA) Prof. dr. M.E. Ladd (German Cancer Research Center, Heidelberg) Prof. dr. H.J. Lamb Prof. dr. ir. B.P.F. Lelieveldt Dr. F.T. Wiggers-de Bruïne Dr. ir. R.F. Remis (Delft University of Technology)

The work presented in this thesis was carried out at the C.J. Gorter Center, department of Radiology at the Leiden University Medical Center.

Financial support for the printing of this thesis was kindly provided by Philips Healthcare, the Netherlands.

It always seems impossible until it's done.

Nelson Mandela (1918-2013)

CONTENTS

Chapter 1 **General Introduction** 1

Part I Dielectric Shimming Applications

Chapter 2 **Dual-Channel Transmit MRI: A Review** 17

Chapter 3 **High Permittivity Pads for Cardiac MRI** 43

Chapter 4 **Effects on SAR during RF-Shimming at 3T** 61

Chapter 5 **Passive RF Shimming in the Thighs at 3T** 75

Chapter 6 **High Spatial Resolution MRI of the Inner Ear at 7T** 89

Part II Applied Electromagnetics in the context of MRI

Chapter 7 **Ventricular B_1^+ perturbation at 7T** 107

Chapter 8 **A Forward Model Analysis of Dielectric Shimming** 117

Chapter 9 **A Theoretical Approach on Dielectric Shimming** 125

Chapter 10 **Summary and General Discussion** 145

Nederlandse samenvatting 153

List of Publications 155

Curriculum Vitæ 157

Acknowledgements 159

CHAPTER 1

GENERAL INTRODUCTION

1

1.1. GENERAL INTRODUCTION

Magnetic resonance imaging (MRI) is a well-established diagnostic imaging modality, most valued for yielding soft-tissue contrast without introducing harmful ionizing radiation. With the wide variety of existing MR techniques, many different types of information can be obtained to study tissue structure, function or probe metabolism in vivo.

Ever since the introduction of MRI in the late 1970s, there has been an incentive to operate at a higher static magnetic field (B_0) strength. Increasing B_0 inherently increases the amount of magnetization that contributes to the signal, thereby increasing the potential signal-to-noise ratio (SNR). The increased SNR can be exchanged for a reduced acquisition time, for example by reducing the number of signal averages, or for an increased spatial resolution in order to better depict small anatomical features. In MR spectroscopy, the increased field strength improves the spectral separation of metabolites and the increased SNR allows for a reduced voxel size, thereby improving the spectral quality and specificity.

Currently, 1.5 Tesla (T) is the standard field strength for clinical body imaging. Recent technological advances have also prepared 3T systems for routine clinical body imaging. Systems operating at even higher field strengths are emerging, ranging from whole body MR systems at 7T up to neuroimaging systems at 11.7T. These have the potential of yielding unique information in various functional areas and pathological conditions.

1.1.1. RF CHALLENGES IN HIGH FIELD MRI

The potential gains when moving to a higher field strength are however often offset by an increased appearance of image artifacts, caused by the interactions between the subject and the radiofrequency (RF) fields to which he is exposed. These interactions lead to a shortening of the RF wavelength as the static field strength and corresponding Larmor frequency increase. Then, as the RF wavelength approaches the dimensions of the body part which is being examined, areas of constructive and destructive interference occur within the body, leading to undesirable spatial variations in signal intensity and tissue contrast. This phenomenon presents a fundamental challenge to the operation of MR systems at high field strengths.

Another critical factor that increases substantially with field strength is the RF induced heating of tissue, which ultimately limits the speed of MR acquisitions in vivo. An increased tissue temperature can cause an unwanted heat sensation and physiological stress, and can ultimately lead to irreversible cellular damage. The RF power entering the subject is therefore subject to stringent safety limits, defined in terms of the specific absorption rate (SAR).

1.1.2. DIELECTRIC SHIMMING

The approach ventured in this thesis to address these RF challenges is termed “dielectric shimming”. In this method, the subject is surrounded by a distribution of dielectric materials which perturb the RF field such that the sensitivity in a selected region is improved. A commonly used dielectric material is constructed from a very dense aqueous suspension of calcium or barium titanate powder, which is then heat sealed to form a flexible pad. Examples of such pads and their positioning in a 7T MR system set up for neuroimaging is shown in Fig. 1.1.

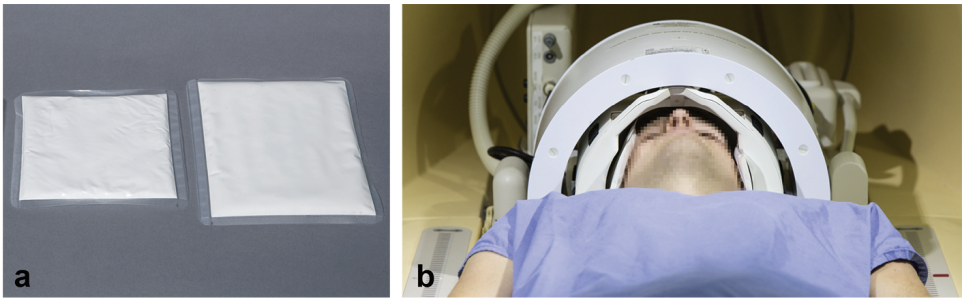

Figure 1.1: Examples of different dielectric pads (**a**) and positioning within the 7T MR system (**b**).

1.2. THESIS AIMS AND OUTLINE

This thesis aims to explore the utility of high permittivity dielectric materials for tailoring the RF field in high field MR. The work comprises two parts, covering the characterization and evaluation of dielectric shimming in applications at 3T and 7T, followed by a theoretical part to derive fundamental mechanisms that underlie RF inhomogeneity at high fields as well as constitute the technique of dielectric shimming.

The first part of this thesis, comprising chapters 2, 3, 4, 5 and 6, presents the evaluation of dielectric shimming in the context of a number of MR applications at 3T and 7T. This part starts with chapter 2 which presents a review of current clinical applications at 3T in which the use of dual-channel RF shimming has shown to improve image quality. This is compared with the use of high permittivity dielectric pads in functional cardiac imaging at 3T in chapters 3 and 4. The use of geometrically optimized dielectric pads is shown to reduce SAR, improve the contrast homogeneity and increase the contrast-to-noise ratio, compared to dual-channel RF shimming. The use of dielectric pads in imaging the thighs is explored in chapter 5. Combining the dielectric shims and an intensity correction filter was shown to improve image quality substantially compared to the situation without pads. Then in chapter 6 dielectric pads are shown to significantly improve the diagnostic imaging quality in high resolution imaging of the inner ear at 7T.

The second part of this thesis, which consists of chapters 7, 8 and 9, discusses some fundamental aspects of RF inhomogeneity at high fields. Chapter 7 explores the origin of local perturbations in the B_1^+ field often measured around the ventricles at 7T. Whereas many authors have interpreted these local B_1^+ perturbations as a measurement artifact related to the long relaxation times of cerebrospinal fluid (CSF), these results indicate that the effect is real and related to the high electrical conductivity of CSF with respect to the surrounding tissues. In chapter 8 a numerical framework is proposed to model the RF field perturbation generated by a dielectric shimming material. This formulation is shown to improve efficiency and convergence of forward modeling techniques, which indicates that the problem complexity is greatly reduced. This approach is further analyzed in chapter 9 where also a method for the automated design of dielectric shimming materials is demonstrated.

Finally, in chapter 10 a summary of the work and general discussion is presented together with main conclusions and future perspectives.

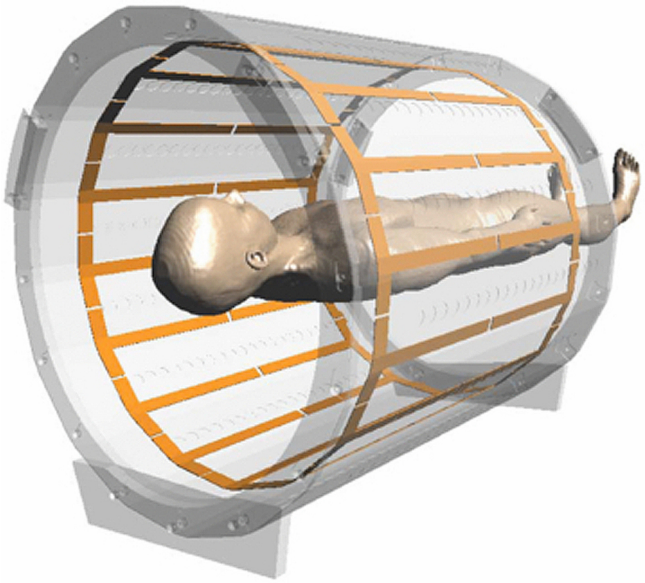

Figure 1.2: Example of a RF transmit "body coil" typically used at 1.5 and 3T.

1.3. TECHNICAL BACKGROUND

Virtually all MR experiments start with the generation of transverse magnetization, a procedure often referred to as "excitation". In this process, the nuclear spin system is tipped away from its equilibrium state by energy exchange via the $\boldsymbol{B}_1$ field generated by the RF transmit coil. This mechanism is governed by the forward circular polarized magnetic component of the RF field, denoted by B_1^+, which manifests a static component in the rotating frame of reference. This field, typically in the order of several μT's, then exerts a torque on the spin system forcing the net magnetization vector to tip away from equilibrium.

The most common transmit coil design used in MR is the so-called "birdcage" design which has been introduced in 1985 by Hayes et al. [1] By exciting such a structure in quadrature, i.e. with 0° and 90° signals on its two orthogonal ports, a circular polarized $\boldsymbol{B}_1$ field is generated within its volume. This design has later been shown to be optimal for RF excitation in the near-field regime [2]. Most 1.5T and 3T systems have such a coil integrated within the bore of the scanner, an example of which is shown in Fig. 1.2, while in some specific applications a local volume coil is used for excitation to reduce the RF exposure level. Neuroimaging at 7T is almost exclusively performed using a head-sized volume coil due to the absence of a body coil in these systems, as the RF exposure in such a case would be very restrictive.

Two parameters relevant to RF transmit coil characterization are the homogeneity of the B_1^+ field, and the transmit efficiency. The transmit efficiency can be expressed as B_1^+ magnitude with respect to the input energy at the coil port, or with respect to tissue heating via the square root of the specific absorption rate (SAR).

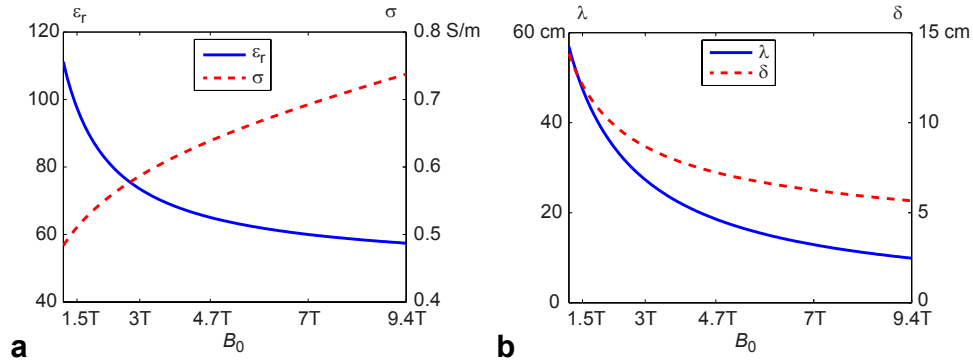

Figure 1.3: Characterization of RF interactions at different field strength. Dielectric properties of grey matter are illustrated in (**a**), showing a decrease in relative permittivity (ε_r) and an increase in electrical conductivity (σ) for higher static field strengths (B_0) [8]. The net result is that both the RF wavelength (λ) and penetration depth (δ) shorten as field strength increases. (**b**)

1.3.1. B_1^+ HOMOGENEITY

While the B_1^+ field in an optimally designed volume coil is in general very homogeneous when it is empty, this is significantly affected when introducing a lossy dielectric object such as the human body. The underlying electrical interactions lead to shortening of the RF wavelength and attenuation of the RF field, respectively. The resulting phase differences in the RF fields originating from the different conducting elements of the RF transmit coil lead to areas of constructive and destructive interference within the subject, with corresponding tip angle variations [3–7].

The RF wavelength λ of a time-harmonic plane wave propagating through a dielectric medium, characterized by the relative permittivity ε_r, can be expressed as

$$\lambda = \frac{c}{f\sqrt{\varepsilon_r}} \tag{1.1}$$

in which c denotes the propagation speed in free space, and f denotes the RF frequency [9]. An illustration of these trends for dielectric properties of grey matter [8] is given in Fig. 1.3. Although the permittivity of tissue generally decreases with frequency, the RF wavelength continues to shorten for increasing field strengths to ~27 cm at 3T and ~13 cm at 7T for gray matter tissue.

The attenuation of a wave is measured by the penetration depth δ, which is the depth at which the field amplitude has decayed to $e^{-1} \approx 37\%$ of its nominal value [9]. The penetration depth decreases with frequency and (effective) electrical conductivity σ[1]. This is known to be problematic in fetal imaging and pathologies such as ascites, where large amounts of conductive body fluids attenuate the RF field. This makes that these examinations are typically performed at 1.5T [10].

An example of B_1^+ inhomogeneity and its effect on images is given in Fig. 1.4, where a 17 cm diameter spherical water phantom shows significant wavelength effects at 7T. The

[1] The term "effective" is used here since the harmonic equivalent of electrical conductivity includes both contributions from free electron movement as well as polarization damping forces.

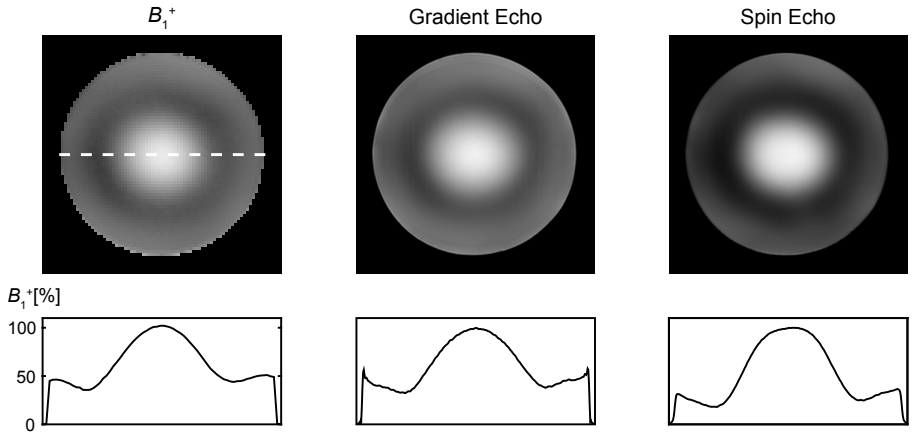

Figure 1.4: Example of B_1^+ non-uniformity and its effect on images at 7T. The spherical water-based phantom shows significant variation in B_1^+ (left), which translate to moderate variations in a low tip angle gradient echo image (middle) and stronger variations in a spin echo image (right).

B_1^+ shows variations of up to 250% within the phantom, which are translated into signal intensity variations in both gradient echo and spin echo images. A spin echo sequence is typically more affected by B_1^+ variations than a gradient echo sequence since echoes are recalled through the application of RF pulses.

1.3.2. SPECIFIC ABSORPTION RATE

RF induced heating is caused by the interaction of the electric component of the RF field with the lossy tissues of the body. This leads to RF power deposition, which is irreversibly converted into heat and distributed through the body tissue by thermodynamic mechanisms such as heat convection and blood perfusion. As these thermodynamic mechanisms are very difficult to predict in vivo, safety regulations are instead defined in terms of the surrogate metric of specific absorption rate (SAR). SAR is defined as the dissipated power per kilogram of tissue (W/kg), within a specific volume V:

$$\mathrm{SAR}(\boldsymbol{r}) = \frac{1}{V}\int_V \frac{\sigma(\boldsymbol{r})|\boldsymbol{E}(\boldsymbol{r})|^2}{2\rho(\boldsymbol{r})}\mathrm{d}V \tag{1.2}$$

in which ρ denotes tissue density and $\boldsymbol{r}$ denotes spatial position. Two specific SAR measures relevant to MRI are the local 10 g SAR and whole body SAR, with corresponding averaging volumes. More information on the regulations with respect to SAR can be found in the IEC60601-2-33 standard issued by the International Electrotechnical Committee [11].

1.4. PARALLEL TRANSMISSION

One approach to alter the interference in the RF field is by adjusting the current distribution on the RF transmit coil, which was first discussed in the context of MRI by Hoult

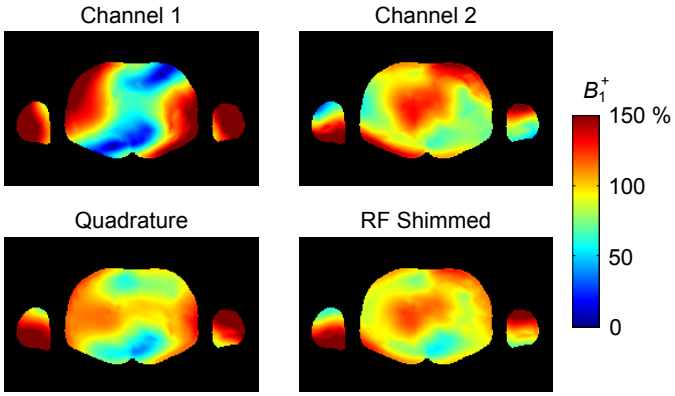

Figure 1.5: Simulated example of dual-channel RF shimming at 3T. Combining the two channels of the body coil in quadrature results in typical areas of low transmit efficiency. By optimizing the relative amplitude and phase shift of the channels, B_1^+ homogeneity can be considerably improved.

[12]. This led to the concept of parallel transmission (PTx), in which the transmit coil is split in discrete elements which are driven by independent sources.

Initial investigations considered controlling the spatial interference pattern in a static manner by adjusting the amplitude and phase settings of each of the channels [12, 13], which is termed "RF shimming". This procedure starts by characterizing the spatial sensitivities of each of the channels, by acquiring channel-wise B_1^+ calibration data. Then, after optimizing the relative amplitudes and phase differences between the channels, the conventional single-channel transmit protocol can be executed. An example of RF shimming in a two-channel 3T body coil is shown in Fig. 1.5. By optimizing the relative amplitude and phase between the two channels, B_1^+ homogeneity can be considerably improved compared to quadrature. This approach has also reached clinical application since the latest generation of 3T systems of all major vendors incorporate dual-channel RF shimming technology [14].

A further extension to static RF shimming is to have complete independent signals transmitted through each of the channels. This allows for dynamic alterations of the B_1^+ field between RF pulses [15, 16] and even during RF pulses [17–19]. This approach can be used for further spatial homogenization of the tip angle distribution [20] but also enables spatially localized excitation [21]. The use of these dynamic PTx signals often requires significant changes to conventional scanning protocols, therefore its implementation in clinical MR is not always trivial. A more elaborate review on PTx can be found in [22].

The increased flexibility available in a PTx system inevitably introduces additional uncertainties with respect to SAR prediction and monitoring [23]. Introducing conservative safety margins to allow such variations would be very restrictive, therefore accurate real-time SAR monitoring is crucial to enable the full potential of PTx [24]. Another aspect which increases the system complexity is the design of PTx signals, which is a mathematically complex problem as illustrated by the plethora of design approaches that have been developed so far, a selection being [25–28].

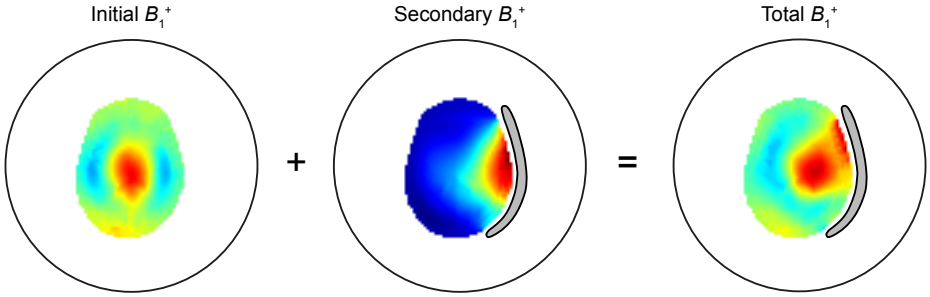

Figure 1.6: Illustration of the mechanism underlying dielectric shimming. A single dielectric pad with high permittivity material ($\varepsilon_r = 300$) is positioned in a neuroimaging setup at 7T. Superposition of the primary (left) and secondary (middle) B_1^+ field components lead to a strong focusing of the total B_1^+ (right).

1.5. BASIC PRINCIPLES OF DIELECTRIC SHIMMING

As the dielectric interactions within a coil lead to B_1^+ inhomogeneities, this mechanism may also be exploited in order to tailor the B_1^+ distribution. The integration of a dielectric material between the rungs and shield of a volume coil was first discussed by Foo et al. [29]. Alsop et al. [30] positioned a large water pad ($\varepsilon_r \approx 78$) against the scalp at 4T to correct for the axial drop-off in sensitivity. This approach was also demonstrated at 7T by Yang et al. [31], yielding significant perturbations of the RF field which allowed for either an improved transverse B_1^+ homogeneity or a deliberate focusing of the transmit sensitivity. Pads constructed of water or aqueous gels have also been shown to improve B_1^+ homogeneity and reduce SAR in body imaging and neuroimaging at 3T [32–35].

The physical mechanism underlying the technique of dielectric shimming can be explained via the electrical currents that are induced in the dielectric material. These currents can be regarded as secondary sources, generating a secondary RF field in addition to the primary RF field which was present without the dielectric pad. The induced current density ($\boldsymbol{J}_i$) in the pad is related to the electric field $\boldsymbol{E}$ as follows:

$$\boldsymbol{J}_i = (\sigma + j\omega\varepsilon_0\varepsilon_r)\boldsymbol{E} \tag{1.3}$$

where σ represents electrical conductivity of the dielectric shimming material, j is the imaginary unit, ω represents the angular frequency, ε_0 and ε_r represent the permittivity of free space and relative permittivity of the dielectric material, respectively. The electrical conductivity σ is associated with losses in the pad, which lead to a damping of the induced currents as well as local absorption of the RF field. Dielectric shimming materials are therefore generally preferred to have a σ as low as possible in view of energy efficiency. The permittivity on the other hand is preferred to be high in order to enhance the effect and thereby reduce the required volume of the pad.

A schematic decomposition of the RF fields in a dielectric shimming scenario is given in Fig. 1.6. The head model, centered in the volume transmit coil at 7T, is augmented by a single dielectric pad ($\varepsilon_r = 300$). The resulting total B_1^+ field is significantly perturbed with a strong local enhancement close to the shimming material, which can be particularly useful in localized MR applications.

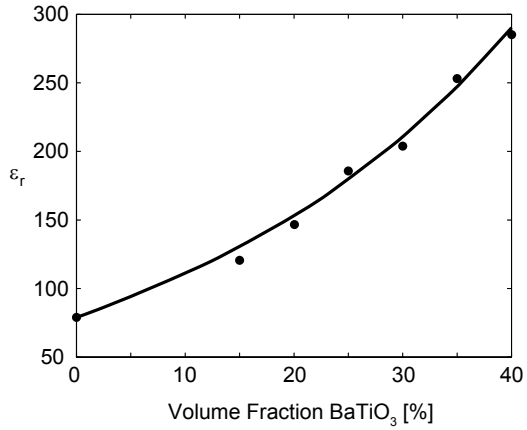

Figure 1.7: Example measurements of dielectric properties of an aqueous slurry of barium titanate at 300 MHz. The measured data are fitted against the logarithmic mixing rule.

1.5.1. HIGH PERMITTIVITY MATERIALS

One important innovation in dielectric shimming was the introduction of materials with a permittivity higher than water by Haines et al. [36]. Most studies so far have been based on either calcium or barium titanate, which belong to the family of perovskite structures and possess a very high intrinsic permittivity. By forming an aqueous suspension of such a material, a flexible pad can be constructed with a high permittivity up to $\varepsilon_r \approx 300$. The volume ratio of the mixture determines the obtained permittivity, following Lichtenecker's logarithmic mixing formula [36–38]. The permittivity of a barium titanate suspension is given in Fig. 1.7 up to a volume ratio of ~40%, at which the suspension becomes saturated.

A natural strategy to further increase the permittivity is to obtain a higher volume ratio, which can be achieved by compressing and sintering the materials at very high temperatures. The resulting solid blocks can reach extremely high permittivity values ($\varepsilon_r > 1000$) [39], however, main drawbacks are associated with the higher weight of these blocks and the complicated fabrication process. In addition, the solid blocks are less comfortable on the subject and cannot easily be geometrically formed to the subject geometry. The use of sintered beads presents another alternative for increasing the volume ratio and related permittivity [40].

1.5.2. DESIGN STRATEGIES

To design an appropriate dielectric shimming device one has to address the relevant degrees of freedom. These may include:

- material properties (permittivity, conductivity)
- geometry (size, thickness, position)
- subject specificity

The most practical approach to this design problem is to perform a parameterized optimization using commercially available simulation software. In such a procedure one sets up a series of electromagnetic simulations in which the relevant degrees of freedom are varied over an appropriate range. This results in many simulations, which are then evaluated by means of a suitable performance measure to determine which set of parameters yields the best performance. This is a very straightforward and stable approach, however can be also very time-consuming.

More efficient design methods are emerging, such as iterative methods in which the dielectric material distribution is iteratively updated to arrive at a predefined target field. In this manner, fewer simulations are needed to obtain a suitable dielectric shim design. However, this approach does require an appropriate model in order to generate suitable updates in the material distribution. Some methods have been proposed based on fast analytical models [41–44] and some based on discretized models [45–47]. Despite the increased efficiency, significant challenges concerning the stability and complexity of such a method remain to be addressed.

REFERENCES

[1] Hayes CE, Edelstein WA, Schenck JF, Mueller OM, and Eash M. An efficient highly homogeneous radiofrequency coil for whole-body NMR imaging at 1.5 T. Journal of Magnetic Resonance 1985; 63:622–628.

[2] Lattanzi R, and Sodickson DK. Ideal current patterns yielding optimal signal-to-noise ratio and specific absorption rate in magnetic resonance imaging: computational methods and physical insights. Magnetic resonance in medicine 2012; 68:286–304.

[3] Sled JG, and Pike GB. Standing-wave and RF penetration artifacts caused by elliptic geometry: an electrodynamic analysis of MRI. IEEE Transactions on Medical Imaging 1998; 17:653–662.

[4] Tropp J. Image brightening in samples of high dielectric constant. Journal of Magnetic Resonance 2004; 167:12–24.

[5] Collins CM, Liu W, Schreiber W, Yang QX, and Smith MB. Central brightening due to constructive interference with, without, and despite dielectric resonance. Journal of Magnetic Resonance Imaging 2005; 21:192–196.

[6] Ibrahim TS, Mitchell C, Schmalbrock P, Lee R, and Chakeres DW. Electromagnetic perspective on the operation of RF coils at 1.5-11.7 Tesla. Magnetic Resonance in Medicine 2005; 54:683–690.

[7] Van de Moortele PF, Akgun C, Adriany G, Moeller S, Ritter J, Collins CM, Smith MB, Vaughan JT, and Uğurbil K. B1 destructive interferences and spatial phase patterns at 7 T with a head transceiver array coil. Magnetic Resonance in Medicine 2005; 54:1503–1518.

[8] Hasgall P, Di Gennaro F, Baumgartner C, Neufeld E, Gosselin M, Payne D, Klingenböck A, and Kuster N. IT'IS Database for Thermal and Electromagnetic Parameters of Biological Tissues. 2015.

[9] von Hippel AR. Dielectrics and Waves. Chapman & Hall, London, 1954.

[10] Yang RK, Roth CG, Ward RJ, DeJesus JO, and Mitchell DG. Optimizing abdominal MR imaging: approaches to common problems. Radiographics 2010; 30:185–199.

[11] International Electrotechnical Commission. Particular requirements for the basic safety and essential performance of magnetic resonance equipment for medical diagnosis. IEC 60601-2-33, 3rd ed., Geneva, Switzerland; 2010.

[12] Hoult DI. Sensitivity and Power Deposition in a High-Field Imaging Experiment. Journal of Magnetic Resonance Imaging 2000; 12:46–67.

[13] Ibrahim TS, Lee R, Baertlein BA, Abduljalil AM, Zhu H, and Robitaille PMLM. Effect of RF coil excitation on field inhomogeneity at ultra high fields: A field optimized TEM resonator. Magnetic Resonance Imaging 2001; 19:1339–1347.

[14] Willinek WA, Gieseke J, Kukuk GM, Nelles M, König R, Morakkabati-Spitz N, Träber F, Thomas D, Kuhl CK, and Schild HH. Dual-source parallel radiofrequency excitation body MR imaging compared with standard MR imaging at 3.0 T: initial clinical experience. Radiology 2010; 256:966–975.

[15] Collins CM, Wang Z, Mao W, Fang J, Liu W, and Smith MB. Array-optimized composite pulse for excellent whole-brain homogeneity in high-field MRI. Magnetic Resonance in Medicine 2007; 57:470–474.

[16] Orzada S, Maderwald S, Poser BA, Bitz AK, Quick HH, and Ladd ME. RF excitation using time interleaved acquisition of modes (TIAMO) to address B1 inhomogeneity in high-field MRI. Magnetic Resonance in Medicine 2010; 64:327–333.

[17] Katscher U, Börnert P, Leussler C, and van den Brink JS. Transmit SENSE. Magnetic Resonance in Medicine 2003; 49:144–150.

[18] Saekho S, Yip Cy, Noll DC, Boada FE, and Stenger VA. Fast-kz three-dimensional tailored radiofrequency pulse for reduced B1 inhomogeneity. Magnetic Resonance in Medicine 2006; 55:719–724.

[19] Cloos MA, Boulant N, Luong M, Ferrand G, Giacomini E, Le Bihan D, and Amadon A. kT-points: short three-dimensional tailored RF pulses for flip-angle homogenization over an extended volume. Magnetic Resonance in Medicine 2012; 67:72–80.

[20] Setsompop K, Alagappan V, Gagoski B, Witzel T, Polimeni J, Potthast A, Hebrank F, Fontius U, Schmitt F, Wald LL, and Adalsteinsson E. Slice-selective RF pulses for in vivo B1+ inhomogeneity mitigation at 7 tesla using parallel RF excitation with a 16-element coil. Magnetic Resonance in Medicine 2008; 60:1422–1432.

[21] Schneider R, Haueisen J, and Pfeuffer J. Shaped saturation with inherent radiofrequency-power-efficient trajectory design in parallel transmission. Magnetic Resonance in Medicine 2014; 72:1015–1027.

[22] Padormo F, Beqiri A, Hajnal JV, and Malik SJ. Parallel transmission for ultrahigh-field imaging. NMR in biomedicine 2015.

[23] Zelinski AC, Angelone LM, Goyal VK, Bonmassar G, Adalsteinsson E, and Wald LL. Specific absorption rate studies of the parallel transmission of inner-volume excitations at 7T. Journal of Magnetic Resonance Imaging 2008; 28:1005–1018.

[24] Graesslin I, Vernickel P, Börnert P, Nehrke K, Mens G, Harvey P, and Katscher U. Comprehensive RF safety concept for parallel transmission MR. Magnetic Resonance in Medicine 2015; 74:589–598.

[25] Sbrizzi A, Hoogduin H, Lagendijk JJ, Luijten P, Sleijpen GLG, and van den Berg CAT. Time efficient design of multi dimensional RF pulses: application of a multi shift CGLS algorithm. Magnetic Resonance in Medicine 2011; 66:879–885.

[26] Wu X, Schmitter S, Auerbach EJ, Moeller S, Uğurbil K, and Van de Moortele PF. Simultaneous multislice multiband parallel radiofrequency excitation with independent slice-specific transmit B1 homogenization. Magnetic Resonance in Medicine 2013; 70:630–638.

[27] Hoyos-Idrobo A, Weiss P, Massire A, Amadon A, and Boulant N. On variant strategies to solve the magnitude least squares optimization problem in parallel transmission pulse design and under strict SAR and power constraints. IEEE Transactions on Medical Imaging 2014; 33:739–48.

[28] Guérin B, Setsompop K, Ye H, Poser BA, Stenger AV, and Wald LL. Design of parallel transmission pulses for simultaneous multislice with explicit control for peak power and local specific absorption rate. Magnetic Resonance in Medicine 2015; 73:1946–53.

[29] Foo TK, Hayes CE, and Kang YW. Reduction of RF penetration effects in high field imaging. Magnetic Resonance in Medicine 1992; 23:287–301.

[30] Alsop DC, Connick TJ, and Mizsei G. A spiral volume coil for improved RF field homogeneity at high static magnetic field strength. Magnetic Resonance in Medicine 1998; 40:49–54.

[31] Yang QX, Mao W, Wang J, Smith MB, Lei H, Zhang X, Ugurbil K, and Chen W. Manipulation of image intensity distribution at 7.0 T: passive RF shimming and focusing with dielectric materials. Journal of Magnetic Resonance Imaging 2006; 24:197–202.

[32] Sreenivas M, Lowry M, Gibbs P, Pickles M, and Turnbull LW. A simple solution for reducing artefacts due to conductive and dielectric effects in clinical magnetic resonance imaging at 3 T. European Journal of Radiology 2007; 62:143–146.

[33] Kataoka M, Isoda H, Maetani Y, Nakamoto Y, Koyama T, Umeoka S, Tamai K, Kido A, Morisawa N, Saga T, and Togashi K. MR imaging of the female pelvis at 3 Tesla: evaluation of image homogeneity using different dielectric pads. Journal of Magnetic Resonance Imaging 2007; 26:1572–1577.

[34] Franklin KM, Dale BM, and Merkle EM. Improvement in B1-inhomogeneity artifacts in the abdomen at 3T MR imaging using a radiofrequency cushion. Journal of Magnetic Resonance Imaging 2008; 27:1443–1447.

[35] Yang QX, Wang J, Wang J, Collins CM, Wang C, and Smith MB. Reducing SAR and enhancing cerebral signal-to-noise ratio with high permittivity padding at 3 T. Magnetic Resonance in Medicine 2011; 65:358–362.

[36] Haines K, Smith NB, and Webb AG. New high dielectric constant materials for tailoring the B1+ distribution at high magnetic fields. Journal of Magnetic Resonance 2010; 203:323–327.

[37] Simpkin R. Derivation of Lichtenecker's Logarithmic Mixture Formula from Maxwell's Equations. IEEE Transactions on Microwave Theory and Techniques 2010; 58:545–550.

[38] Teeuwisse WM, Brink WM, Haines KN, and Webb AG. Simulations of high permittivity materials for 7 T neuroimaging and evaluation of a new barium titanate-based dielectric. Magnetic Resonance in Medicine 2012; 67:912–918.

[39] Rupprecht S, Sica CT, Sahul R, Kwon S, Lanagan MT, and Yang QX. Drastic Enhancement and Manipulation of RF Field with Ultra High Dielectric Constant (uHDC) Material at 3T. In: Proceedings of the 21st Annual Meeting of ISMRM, Salt Lake City, UT, USA, 2013; p. 396.

[40] Yang QX, Rupprecht S, Luo W, Sica C, Herse Z, Wang J, Cao Z, Vesek J, Lanagan MT, Carluccio G, Ryu YC, and Collins CM. Radiofrequency field enhancement with high dielectric constant (HDC) pads in a receive array coil at 3.0T. Journal of Magnetic Resonance Imaging 2013; 38:435–440.

[41] Jayatilake ML, Storrs J, Chu WJ, and Lee JH. Theoretical determination of the dielectric constant for passive RF shimming at high field. In: Proceedings of the 19th Annual Meeting of ISMRM, Montreal, Canada, 2011; p. 3887.

[42] Carluccio G, Oh S, Yang QX, Erricolo D, Luo W, and Collins CM. Near-Field Wave Impedance Matching with High-Permittivity Dielectric Materials for Optimum Transmittance in MRI Systems. In: Proceedings of the 21st Annual Meeting of ISMRM, Salt Lake City, UT, USA, 2013; p. 4374.

[43] Winkler SA, Sbrizzi A, van den Berg CAT, Luijten PR, and Rutt BK. Optimized Dielectric Shimming in High-Field Magnetic Resonance Imaging: A Theoretical Approach. In: Proceedings of the Workshop Scattering by Aggregates, Bremen, Germany, 2014; pp. 70–73.

[44] Lattanzi R, Vaidya MV, Carluccio G, Sodickson DK, and Collins CM. Effects of high-permittivity materials on absolute RF coil performance as a function of B0 and object size. In: Proceedings of the 22nd Annual Meeting of ISMRM, Milan, Italy, 2014; p. 4818.

[45] Brink WM, and Webb AG. A forward model analysis of dielectric shimming in magnetic resonance imaging. In: Proceedings of the 15th Annual Meeting of ICEAA, Torino, Italy, 2013; pp. 528–531.

[46] Brink W, and Webb A. Integral Equations Based Modeling Approach to Dielectric Shimming. In: Proceedings of the 23rd Annual Meeting of ISMRM, Milan, Italy, 2014; p. 4831.

[47] Brink WM, Remis RF, and Webb AG. A theoretical approach based on electromagnetic scattering for analysing dielectric shimming in high-field MRI. Magnetic Resonance in Medicine 2015.

PART I

DIELECTRIC SHIMMING APPLICATIONS

Chapter 2

Clinical Applications of Dual-Channel Transmit MRI: A Review

J Magn Reson Imaging 2015; *in press*

Wyger M. Brink
Vikas Gulani
Andrew G. Webb

ABSTRACT

This article reviews the principle of dual-channel transmit MRI and highlights current clinical applications which are performed primarily at 3 Tesla. The main benefits of dual-channel transmit compared with single-transmit systems are the increased image contrast homogeneity and the decreased scanning time due to the more accurate local specific absorption ratio estimation, meaning that less conservative safety limits are needed. The dual-transmit approach has been particularly beneficial in body imaging applications, and is also promising in terms of cardiac, spine, and fetal imaging. Future advances in transmit SENSE, the combination of dual-channel transmit with high permittivity pads, as well as the potential increase in the number of transmit channels are also discussed.

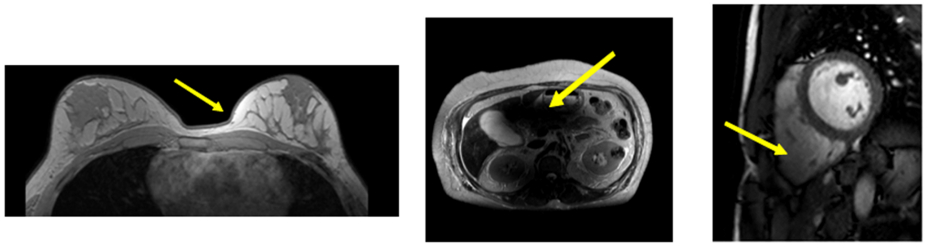

Figure 2.1: Examples of image artifacts at 3 Tesla. Left: Breast images showing unequal left/right signal intensity. Center: Anterior/posterior signal voids in abdominal imaging. Right: Shading artifacts in cardiac scans.

2.1. INTRODUCTION

Clinical MRI Scans, ideally, have uniform tissue contrast across the entire image. On 1.5 Tesla (T) and 3T systems the body coil is used for excitation, and is designed either as a birdcage [1] or transverse electromagnetic magnetic (TEM) [2] geometry, both of which provide a homogeneous radiofrequency (RF) transmit field (B_1^+) in an empty coil. However, the presence of the patient in the RF coil disturbs the uniformity of the RF transmit field, and results in areas within the body in which the transmit field is significantly weaker than in other regions. This perturbation increases as a function of the main magnetic field (B_0), the dimensions of the body part being imaged, and the relative permittivity (sometimes referred to as the dielectric constant) and conductivity of the tissue. A spatially varying transmit field produces corresponding variations in the flip angle within the body, and subsequent distortions in image contrast weighting. In extreme cases signal voids can occur in the image. Examples of image artifacts in breast, abdominal and cardiac scans at 3T are shown in Fig. 2.1. Although some degree of intensity correction is possible using a direct measurement of the transmit field, these types of postprocessing schemes cannot recover any of the reduced tissue contrast due to spatially varying tip angles. Because these effects are more severe the higher the magnetic field, many clinical protocols which could potentially benefit from the intrinsically higher signal-to-noise ratio (SNR) at 3T continue to be run on 1.5T systems. Several review articles have addressed the considerations in determining which clinical applications are appropriate for which field strength [3–6].

The major factor causing B_1^+ inhomogeneity is the high relative permittivity of the body. The wavelength of the RF waves in tissue is inversely proportional to the square root of the relative permittivity of the tissue. Figure 2.2 shows the relative permittivity of muscle, as well as the corresponding wavelength, as a function of field strength. In muscle, at 1.5T the wavelength is ~50 cm, whereas at 3T it is ~26 cm. This means that at 3T the dimensions of the body are a substantial fraction of the RF wavelength in tissue, and so the RF energy propagating through the body from different directions by means of the body coil produces areas of constructive and destructive interference, as shown schematically in Fig. 2.3. The second factor which can cause B_1^+ inhomogeneity is tissue conductivity: increased conductivity corresponds to reduced RF penetration through tissue. As shown in Fig. 2.2, this effect is not too severe with penetration depths of many tens of centimeters for healthy tissue at 1.5 and 3T. However, because conductiv-

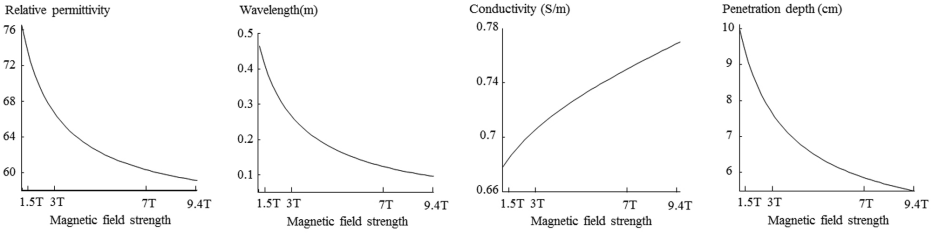

Figure 2.2: Plots of relative permittivity, wavelength, conductivity, and penetration depth for muscle tissue at different magnetic field strengths.

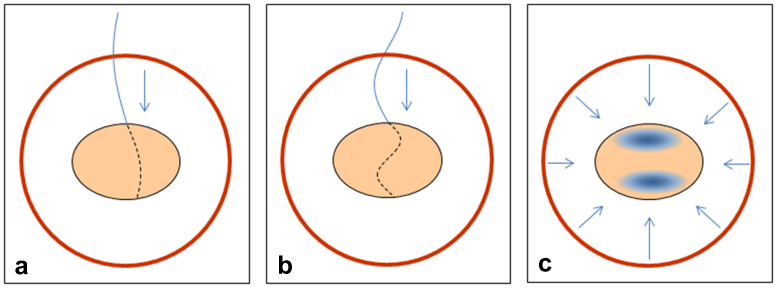

Figure 2.3: A schematic showing interference effects of the RF field in the body, represented as an ellipse, within the circular body coil (red circle). **a**: At 1.5T, the wavelength in air is ~235 cm, and in tissue ~52 cm. The tissue wavelength is larger than the body dimensions and, therefore, relatively little wave interference occurs. **b**: At 3T, the wavelength in air is ~117 cm, and ~26 cm in tissue. A much greater degree of wave interference is, therefore, seen than at 1.5 Tesla. **c**: This increased wave interference manifests itself as areas of low transmit efficiency (shaded regions).

ity increases with frequency (and, therefore, magnetic field strength) the effects become much more pronounced at 7T and above. A full mathematical description of the effects of permittivity and conductivity on the RF behavior in elliptical objects can be found, for example, in the publication by Sled and Pike [7].

The relationship between body type and the degree of image artifacts involves several components. Obese patients typically show greater image inhomogeneity due to their larger body size. Pathological conditions such as ascites, in which large volumes of water accumulate, are particularly problematic due to the high relative permittivity. If fluid accumulations within the body also have high salt content, then image uniformity is further degraded due to the reduced penetration depth. However, as reported by many authors, image artifacts can also be substantial in very thin patients. This is because the cross-section of the body in these cases is highly elliptical, i.e., very asymmetric with respect to the circular body coil. There is very little that can be done to overcome these artifacts using a single transmit channel 3T scanner (Fig. 2.4a). Dielectric pillows containing water-based gels have been proposed [8], and indeed image quality generally increases, but these pillows are large and heavy, placement is critical and patient comfort is compromised. New approaches using much thinner pads with very high permittivity materials [9] are discussed in the final section of this article.

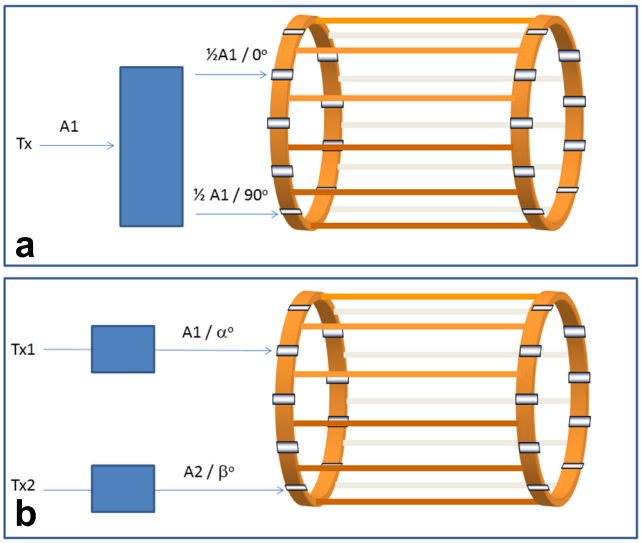

Figure 2.4: **a**: Single-channel transmit body coil operating in quadrature mode. There is a fixed phase angle of 90° between the two ports, and the amplitudes of the signal fed into each of the two ports are the same. **b**: Dual-channel transmit body coil. Using two separate transmitters, the amplitudes and phases of the two channels can be set independently, giving additional degrees of freedom.

The clinical importance of this situation has resulted in the recent introduction of commercial dual-channel transmit systems at 3T, in which the body coil is effectively split into two channels, each of which can be driven with an independently controlled magnitude and phase, as shown in Fig. 2.4b. The additional degrees-of-freedom (relative amplitudes and relative phases of the two channels) compared with a single degree-of-freedom (amplitude) for a conventional single transmit system can produce significant increases in RF transmit homogeneity, as has long been known theoretically. This approach of having extra degrees of freedom has been adapted from similar approaches in the area of electromagnetic hyperthermia [10], and is considered in more detail in the following sections.

SINGLE-CHANNEL VERSUS DUAL-CHANNEL TRANSMISSION

In the conventional single-channel approach, Fig. 2.4a, the body coil is driven in quadrature with equal magnitudes and a fixed 90° phase shift of the two signals fed into the two orthogonal ports of the coil. Although this mode is effective in terms of providing a homogeneous transmit field at low ($\leq$ 1.5T) magnetic field strengths, this geometry is not optimal at 3T for a subject geometry which is essentially elliptical, and results in nonuniformities in the transmitted RF field. The dual-channel transmit approach forms a logical improvement to the single-channel system in that it uses two completely independent transmit chains for driving the two ports of the coil. Different amplitudes and phases of the RF pulses, as well as their waveforms, can be applied through these two independent channels. Initially it was thought that a limited number of fixed preset am-

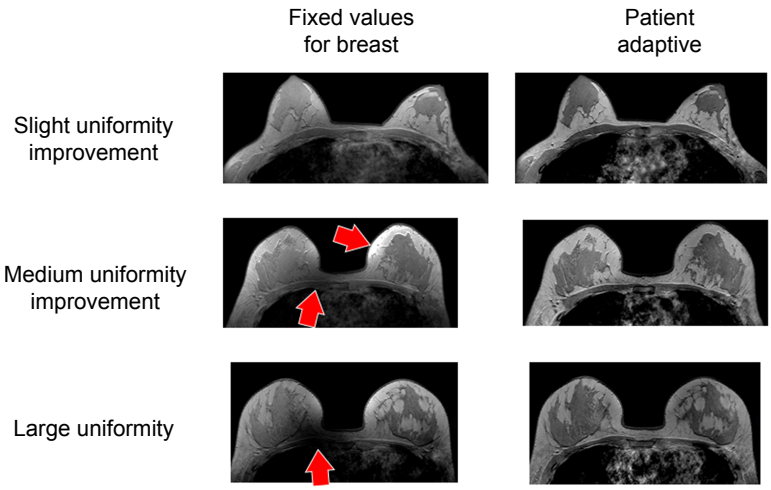

Figure 2.5: An illustration of the advantages of using patient-specific B_1^+ shimming for breast imaging compared with a generically optimized fixed amplitude/phase relationship. In the upper panel the fixed values give good image quality with no signal dropouts or differential intensities in the left and right breasts: there is little difference between fixed and patient-specific values. However, in the lowest panel there are clear image artifacts produced by the fixed-value approach in a different subject with larger breast size. In contrast, by using patient-specific values of the amplitude and phase, good image quality can be obtained in all cases.

plitude ratios and phase differences could be used for different applications, e.g., breast, liver, and cardiac imaging, without the need to determine patient-specific values. However, as illustrated in Fig. 2.5 studies have shown that this approach was too simplistic, as there was significant variation in imaging performance between patients [11]. Therefore, most studies are now performed using patient-specific settings. The process of optimizing image quality by adjusting the amplitudes and phases of the two channels is often referred to as "B_1^+ shimming." A short additional calibration scan (typically lasting less than a minute) is added to the start of the clinical protocol to map the B_1^+ field within the patient, and based upon this scan the optimum relative phases and magnitudes feeding the two ports of the dual-channel transmit coil are calculated. There are many different schemes for fast B_1^+ mapping [12–14] with different vendors using different sequences.

The dependence of the B_1^+ field on the amplitude and phase settings in a dual-channel system is illustrated in Fig. 2.6, which shows that moderate differences can have quite dramatic effects on the spatial distribution of the RF field: simulations were performed as described in Brink and Webb [15]. A 2.5 mm isotropic grid was used with commercially available simulation software (xFDTD 7.2, Remcom Inc., State College, PA). A two-port-drive high-pass birdcage structure was used and the coefficient of variance (CV) of the B_1^+ homogeneity was calculated for each case. In the case shown in Fig. 2.6 the highest B_1^+ homogeneity, i.e., the lowest value of the CV, corresponds to a quadrature phase relationship with a 10 dB power difference between the two channels.

In addition to the homogeneity of the B_1^+ transmit field, the other critical component is the specific absorption rate (SAR), covered in the next section. This often sets the limits for the total time that a particular scan can take.

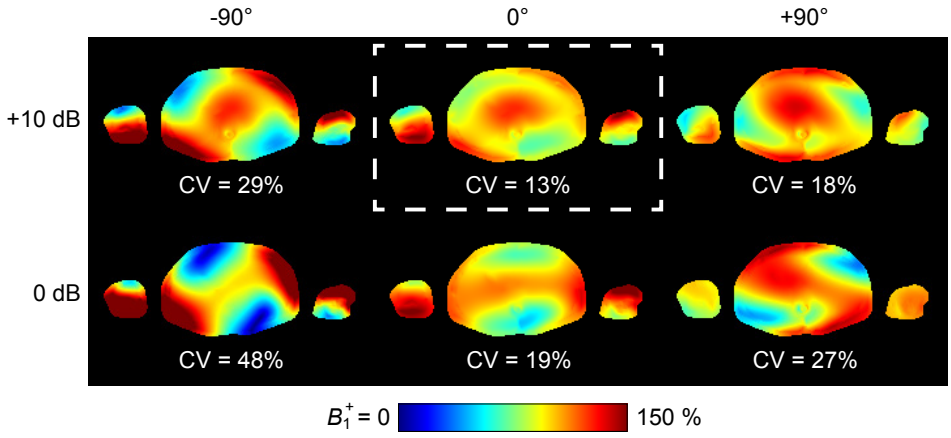

Figure 2.6: Simulations of the effect of B_1^+ shimming on the B_1^+ transmit field. The vertical axis denotes the relative power ratio, and the horizontal axis the relative phase of the two channels. The transverse B_1^+ field is illustrated through the centre of the torso at the level of the liver (superior/inferior direction). The simulation was performed using the Ella model of a normal-sized woman [16] with 75 tissue types, and the maps were normalized to the mean B_1^+. The white box corresponds to the case of the lowest CV, i.e., the highest B_1^+ homogeneity.

SPECIFIC ABSORPTION RATE

Heat is created in the body by the interaction of the electric field component of the EM field generated by the transmit coil with the conductive elements (tissue, blood, skin) of the body. The power deposited in the body is quantified in terms of the SAR measured in Watts/kg. The SAR is proportional to the product of the conductivity and the square of the electric field. The two different SAR measures relevant to clinical MR scanning are the local 10 g SAR and whole body SAR. As the terms suggest the local SAR is defined as the peak SAR value after spatial averaging over any 10 g of tissue, whereas the whole body SAR is spatially averaged over the entire body. In the United States, the Food and Drug Administration (FDA) limits are: whole-body average 4 W/kg over 15 min, head/ trunk local (1 g tissue) 8 W/kg over 10 min, extremities (1 g tissue) 12 W/kg over 5 min [17]. The International Electrotechnical Committee (IEC) has three levels, with all values over a 6-min average: normal (all patients), whole body average 2 W/kg, head/trunk local 10 W/kg and extremities local 20 W/ kg; first level (supervised) 4 W/kg, 10 W/kg, and 20 W/kg, respectively; second level (institutional review board approval) 4 W/kg, >10 W/kg and >20 W/kg, respectively [18].

These safety limits ultimately pose constraints on the values of different imaging parameters such as the flip angle or minimum TR. In practice, the MRI system will not start or will abort the scan if either the IEC-60601-2-33 6-min or 10-s limit (the SAR over any 10-s period is not allowed to exceed twice the levels listed previously) for global or local SAR is exceeded. Using a body coil transmit at 3T, as discussed by many publications, the local SAR limits constrain the imaging parameters before the whole body SAR limit is reached.

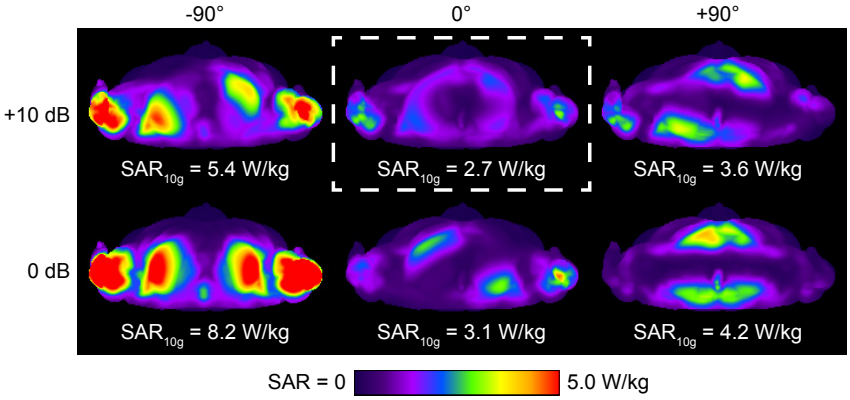

Figure 2.7: Simulation examples of the effect of B_1^+ shimming on the local SAR. Shown are the transverse maximum intensity projections of the 10 g-averaged SAR for different driving conditions. All data is normalized to a mean B_1^+ of 1 μT in the transverse plane. The white box corresponds to the case of the lowest SAR.

In general, SAR is predicted by the MR scanner based on the particular sequence being run. For single-channel transmit systems, these estimates incorporate a set of body models simulated at different landmarks within the system, from which the worst-case scenario (i.e., the maximum possible local SAR as a function of both body model and landmark) provides a very conservative estimate of the local SAR. The SAR estimate is then coarsely calibrated by measuring the global B_1^+, i.e., as a single value for the entire imaging volume. In contrast, the more elaborate calibration procedure mandatory for B_1^+ shimming in a dual-channel transmit system provides a more reliable estimate of the local SAR, because the B_1^+ field is actually measured, meaning that these additional safety margins can be reduced. Furthermore, the effect of B_1^+ shimming has been shown to be typically coincident with a reduction of local SAR. This is illustrated in Fig. 2.7, which shows transverse maximum intensity projections of the 10 g-averaged SAR, in which the same driving conditions for the RF coil were applied as in Fig. 2.6. As can be seen from both figures, the driving condition that improves B_1^+ homogeneity also reduces local SAR. This means that in many cases, the local SAR in the B_1^+ shimmed case is actually lower than in the single-channel transmit configuration, even if the total amount of power deposited within the body is higher. In this situation the imaging sequence parameters can be "improved" by, for example, decreasing the minimum TR, increasing the number of slices, or increasing the flip angle. The SAR behavior of multi-channel transmit systems is an important advantage and has been investigated by many groups [19–22].

2.2. CLINICAL APPLICATIONS

The first extensive clinically oriented reports on the advantages of dual-channel transmit MRI was by Willinek et al. [23] who investigated several different application areas. They determined that fast spin-echo images of the liver showed significantly better image homogeneity with dual-channel transmit, as did diffusion-weighted liver imaging.

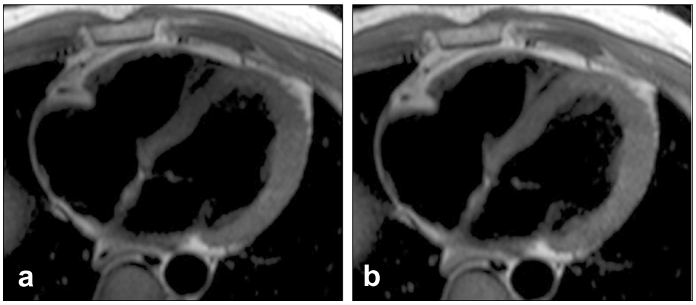

Figure 2.8: Axial TSE BB images (TR 2000 ms, TE 90 ms) obtained with single-channel transmit (**a**) and dual-channel transmit (**b**) in a 39-year-old man suspected of having arrhythmogenic right ventricular cardiomyopathy. Note the improved signal homogeneity of the image acquired with RF shimming, which enables clear delineation of the inter-ventricular septum and the anterior free wall of the right ventricle. Figure reproduced with permission from [24].

The effect was particularly pronounced in three patients with ascites. The total imaging time could be reduced by one-third due to the reduced maximum local SAR. For scans of the lumbar spine, reductions of 50% in total imaging time for sagittal T_2-weighted and 18% for sagittal T_1-weighted scans were achieved. This pivotal study formed the basis for many subsequent investigations of dual-transmit performance, which are summarized according to organ in the following sections.

CARDIAC

Cardiac imaging at 3T has shown significant benefits compared with 1.5T in applications such as myocardial tagging and myocardial perfusion measurements [25, 26]. However, in conventional functional protocols using cine sequences and single-channel transmit, the decreased B_1^+ homogeneity over the heart at 3T reduces image contrast compared with 1.5T. Sung and Naya [27] have reported that the magnitude of the B_1^+ field can vary by up to 50% across the heart at 3T. For single-channel transmit 3T systems, the minimum TR is greater than that at 1.5T due to the local SAR constraints. In addition to increased scan times, the longer TR increases the sensitivity of the technique to banding artifacts in balanced steady state free precession (bSSFP) sequences, which are the mainstay of cardiac scanning at 1.5T [28]. Despite several authors having shown that there is an increased SNR and contrast-to-noise ratio (CNR) at 3T, the nonuniform flip angle distribution results in sections of the free right ventricular wall and the mid-ventricular and apical septum being obscured [29, 30]. The approach of using preset RF shims [31] was initially proposed, but was not found to be particularly effective, because patient size and the presence of sternal wires, pericardial effusions and pleural effusions, amongst other phenomena, strongly affect the B_1^+ spatial distribution within the heart. Therefore, B_1^+ shimming is performed for each individual patient.

The first in-depth investigation of dual-channel transmit cardiac MRI was by Mueller et al. [24]. A cardiac-triggered B_1^+ calibration scan was run for each subject using the saturated dual-angle method (SDAM) with segmented echo planar imaging (EPI) readout within a single breath-hold [12]. The mean percentage of the achieved flip angle

with dual-channel transmit was 91.9 ± 3.3% versus 72.8 ± 4.0% for single-channel transmit. The CNR between the basal interventricular septum and blood pool increased from 26.3±3.4% to 33.3±3.4% with a bSSFP cine sequences, and from 73.0±6.0% to 87.3±5.8% with a turbo spin echo (TSE) black-blood (BB) sequence. In terms of image quality, the contrast between papillary muscles and/or myocardium and the blood pool was significantly increased, and the signal drop-off in the septum, right ventricle, and right ventricular free wall were reduced, as shown in Fig. 2.8. The TR could be significantly reduced, which led to a decrease in banding artifacts from bSSFP sequences.

Jia et al. [32] extended the analysis of dual-channel versus single-channel transmit by investigating how the reduced local SAR using dual-channel transmit enabled either an increased value of the flip angle or a decreased TR to be used. In their analysis, the TR could be reduced from 3.4 ms to 2.8 ms for a fixed flip angle of 45 in short-axis ventricular cine scans, or alternatively the TR could be maintained at 3.4 ms and the flip angle increased to 58. Krishnamurthy et al. [11] investigated the performance of a dual-channel transmit system for subjects with different body mass indices (BMIs). The authors showed increased B_1^+ homogeneity, image quality, SNR and CNR for the dual-channel transmit approach, confirming the data from previous studies. In addition, they found that the B_1^+ inhomogeneity from a single-channel system was not correlated to the BMI (or associated measures such as body surface area and width ratio) of the subject. Indeed, they also found that the degree of improvement in B_1^+ homogeneity using the dual-channel transmit approach was also not correlated to these measures. These findings provide further evidence that a patient-specific B_1^+ shimming approach, rather than using predetermined fixed values, is most appropriate. In a study on high-dose dobutamine stress (HDDS) at 3T, Strach et al. [33] also found significant improvements in image and diagnostic quality using a dual-channel transmit system. In the HDDS study ($n = 13$), all 13 cases were found to be diagnostic in dual-channel transmit mode, compared with only 5 of 13 with single-channel transmit. HDDS studies are potentially affected even more than standard clinical scans by bSSFP image artifacts due to the significant increase in heart rate, and, therefore, more complex and greater blood flow, which in turn result in greater ΔB_0-induced image artifacts for a given TR. The fact that the TR can be reduced in dual-channel transmit mode is, therefore, particularly important in this type of application.

MUSCULOSKELETAL

The first application of dual-channel transmit MRI in the spine was presented by Nelles et al. [34]. The authors showed that the duration of a three-station examination of the entire vertebral column could be reduced by, on average, a factor of one-third due to the shorter TR values enabled by the reduced local SAR estimate when using dual-channel transmit. Sagittal T_2-weighted scans had a reduction in TR from 3496 to 1748 ms, sagittal T_1-weighted scans from 812 to 578 ms, and sagittal spectral adiabatic inversion recovery (SPAIR) scans from 3554 to 2495 ms. Qualitative analysis showed that the diagnostic imaging quality was comparable to that from the single-channel transmit. In the same study, the authors reported that the transmit power was raised by a mean value of 68% for dual-channel transmit compared with single-channel transmit, while remaining within SAR limits, and produced the same maximum transmit field. However, the root-mean-

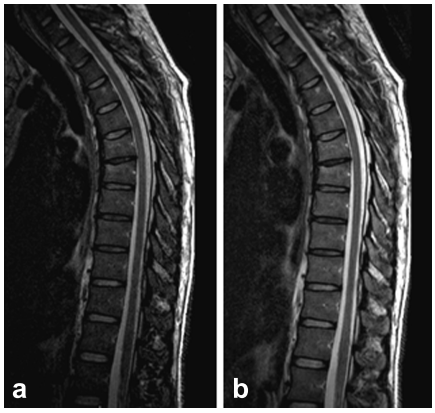

Figure 2.9: Comparisons of single-channel and dual-channel transmit in the spine. **a**: Sagittal single-channel images acquired in 5 min. **b**: Corresponding dual-channel images acquired in 3 min with a reduced TR and showing greater image contrast uniformity.

square (RMS) of the magnitude of the B_1^+ field was increased by an average of 29% using the dual-channel transmit approach, showing that a higher transmit homogeneity and average efficiency had been achieved.

In routine clinical practice, the reduced total imaging time is particularly important in spine applications due to patient discomfort from lying still for long periods of time: images showing slightly improved image quality even when using reduced imaging times using dual-transmit are shown in Fig. 2.9. A follow-up study provided further quantitative analysis of single-channel versus dual-channel transmit mode in the lumbar spine [35]. In this case, the authors kept the TR value the same for both cases: however, because the local SAR estimates were reduced using dual-channel transmit, they were able to scan more slices in each TR interval, which halved the imaging time for their axial T_2-weighted and axial T_1-weighted scans. Qualitative assessment by two neuroradiologists showed that both judged 90% of the scans (axial T_1-weighted, axial T_2-weighted, sagittal T_1-weighted, and sagittal T_2-weighted) to be superior for the dual-channel transmit mode. Measures of the CNR and SNR showed improvements of 53% and 19% (sagittal T_1), 48% and 23% (axial T_1), 38% and 20% (sagittal T_2), and 100% and 18% (axial T_2), respectively.

The same group has recently used a dual-channel transmit system for producing quantitative $T_{1\rho}$ maps, which are representative of the distribution of proteoglycan content, in the lumbar spine disk spaces [36]. The authors showed that the dual-channel transmit approach allowed them to use much thinner slices (3 mm) as opposed to 8 mm using the single-channel approach, thus reducing partial-volume effects. Using dual-channel transmit it was possible to run a three-dimensional sequence within SAR limits. In contrast, only a 2D multi-slice sequence was possible in single-channel transmit mode. The reduction in estimated SAR enabled more rapid acquisition of individual images, each one acquired with a specific spin-lock period. This meant that a greater number of images could be acquired within a given total scan duration, which led to a more accurate quantification of the $T_1\rho$ images.

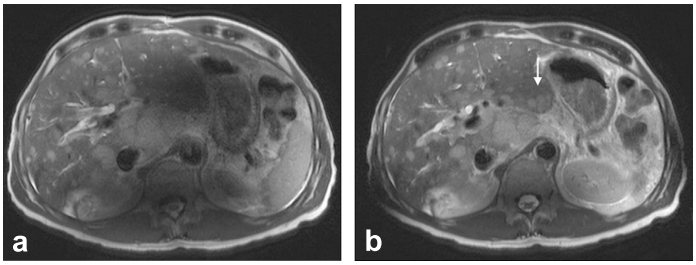

Figure 2.10: Metastatic pancreatic tumor in a 52-year-old man. **a**: Transverse T_2-weighted TSE image acquired using single-channel transmit. There are marked signal losses in the left lobe of the liver and dorsal parts of the right lobe of the liver. Image quality was rated as poor and lesion conspicuity moderate by two readers. **b**: Corresponding image acquired with dual-channel transmit. Image quality and lesion conspicuity were rated as good by both readers. One additional confluent liver metastasis in Couinaud liver segment II (arrow) was identified by both readers. Figure reproduced with permission from Kukuk et al. [44].

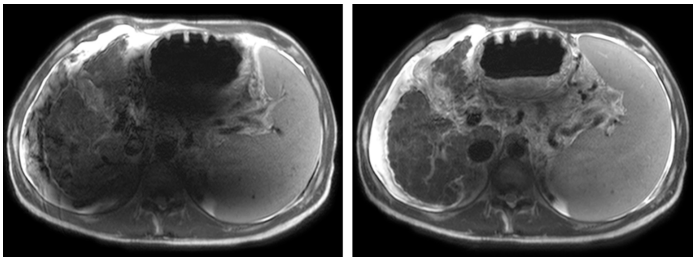

Figure 2.11: Example of image improvement by means of dual-channel transmit from a patient with ascites. A T_2-weighted TSE sequence was run with spatial resolution $1.2 \times 1.4 \times 7$ mm^3 within a single breathhold of 14 s. Left: Single-channel transmit. Right: Dual-channel transmit.

BODY IMAGING

As noted by many researchers, the intrinsic increase in SNR in body imaging by moving from 1.5T to 3T is often offset by a greater extent of signal loss and inhomogeneous image contrast [37–43], rendering the higher field images less diagnostically useful. Dual-channel transmit technology has made a substantial contribution to restoring the advantages of the higher field. Kukuk et al. [44], using axial T_2-weighted singleshot turbo spin echo (TSE) sequences, showed significant improvement in the detection of liver lesions using dual-channel compared with single-channel transmit, in addition to improved lesion conspicuity, lesion contrast and general image quality. An example is shown in Fig. 2.10, which displays significantly improved image quality in segment 3 of the liver, with an increase in lesion conspicuity and detection (white arrow). Luo et al. [45] have also shown significant improvements in liver imaging using a dual-channel transmit approach.

As mentioned earlier, image quality degradation at 3T is particularly severe with patients with ascites, a pathological condition in which large volumes of fluid accumulate in the abdomen. Because ascites is normally a product of pathologies such as liver cirrhosis or neoplasms, it is important to be able to image the affected organs for diagnosis. The fluid has a very high permittivity and conductivity, and, therefore, has a very severe

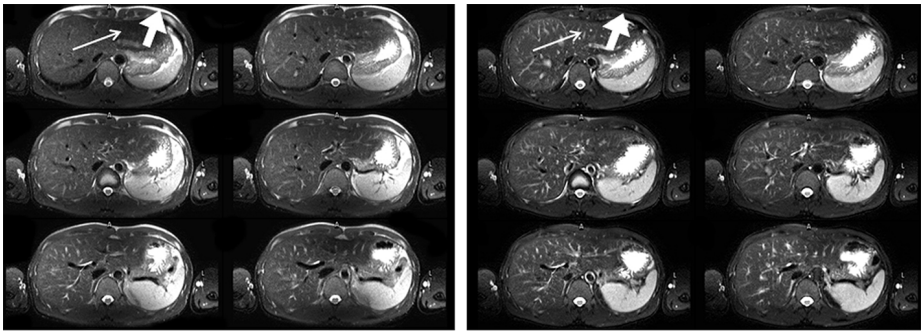

Figure 2.12: **a**,**b**: An example of improved image uniformity (thin arrow) and also fat suppression (thick arrow) using dual-channel transmit and a T_2-weighted TSE sequence with SPAIR fat suppression.

deleterious effect on the B_1^+ homogeneity. An example of how dual-channel transmit can improve image quality is shown in Fig. 2.11. The increased homogeneity of the transmit field also enables improvements in fat suppression, as illustrated in Fig. 2.12, even for methods such as SPAIR which have an "in-built" robustness with respect to B_1^+ inhomogeneity due to the use of an adiabatic pulse.

Diffusion-weighted abdominal imaging is another area that has shown significant improvement when using the dual-channel transmit approach [46, 47]. Any B_1^+ inhomogeneity present not only reduces the image intensity but incomplete fat suppression, as a result of spatially varying flip angles, can cause significant ghosting in the images. Riffel et al. [48] showed that images acquired using a dual-channel transmit 3T were of higher quality than those acquired at 1.5T, and both were better than those acquired with a single-channel transmit 3T system, as demonstrated in Fig. 2.13. In a similar study by Rao et al. [49], diffusion coefficients determined using dual-channel transmit at 3T were found to be almost identical to those measured at 1.5T, the current gold standard. This is in stark contrast to the case using single-channel 3T systems, where the values obtained are not currently considered to be reliable [50]. Diffusion-weighted whole-body imaging with background body signal suppression (DWIBS) is another technique that has been explored using dual-channel transmit at 3T. DWIBS has been used for several different, mainly oncological applications [50–53]. In a trial involving 40 subjects, using dual-channel transmit compared with single-channel transmit, Murtz et al. [46] showed that signal homogeneity was improved in 25/40 cases and was equal in 15/40 cases, and fat suppression improved in 17/40 and was equal in 23/40 cases. In addition, the total scan time per patient was reduced by approximately one-third. The image homogeneity improved in 50% of the pelvis cases, 100% of the abdominal cases, 67% of the chest cases, and 60% of the neck cases: in all other cases the images were judged to be equal. Fat suppression was improved in 33% of the pelvis cases, 50% of the abdominal cases, 83% of the chest cases: in all other cases the images were judged to be equal.

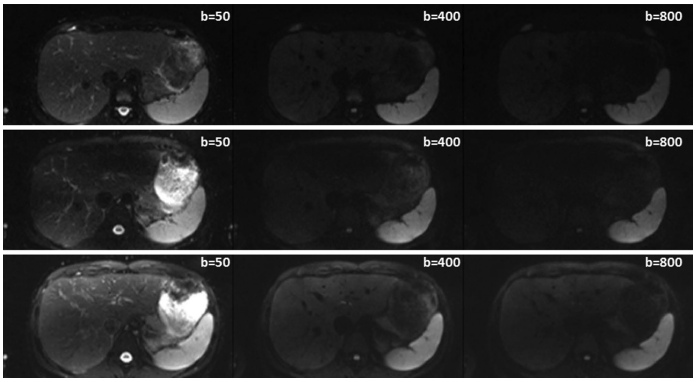

Figure 2.13: Representative diffusion-weighted images from healthy volunteers acquired at 1.5T (top row), using a single channel transmit 3T (middle row), and using a dual-channel transmit 3T (bottom row). From left to right within each row, *b*-values increase from 50 to 400 to 800 s/mm^2. Reproduced with permission from Riffel et al. [48].

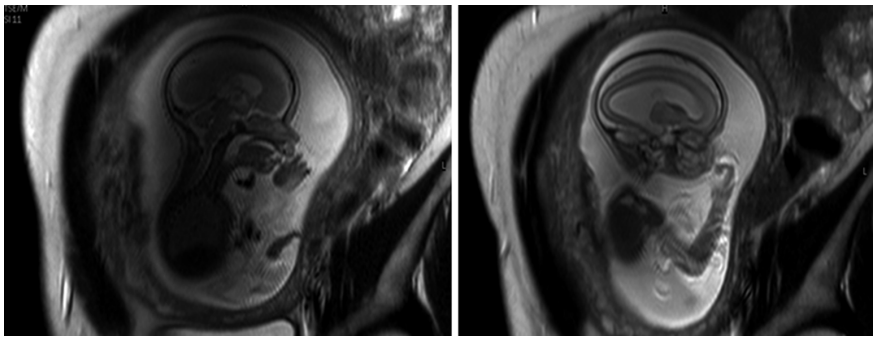

Figure 2.14: Comparison between single-channel (left) and dual-channel (right) single shot spin echo images of a fetus. The single-channel image shows a very low signal intensity in the center of the image, with much reduced contrast in the fetal brain. This is due to a large amount of amniotic fluid, combined with the large size of the patient. The dual-channel transmit approach improves the diagnostic image quality substantially.

FETAL IMAGING

Ultrasound is currently the main imaging modality used to diagnose disorders related to pregnancy. However, fetal MRI is increasingly being used because the quality of ultrasonic imaging is highly dependent on the maternal body habitus and fetal position. Additionally, visualization of the brain using MRI is not restricted by the bony structure of the skull. Soft tissue contrast is better in MR images and abnormally large fetuses can also be studied. However, fetal MR imaging at 3T is particularly sensitive to transmit field inhomogeneities because large volumes of high permittivity and high conductivity liquid, primarily amniotic fluid, are often present. In this case, the added flexibility of dual-channel transmit systems often results in significantly improved image quality. Figure 2.14 shows a comparison between single-channel and dual-channel transmit for a single shot spin echo sequence at 3T.

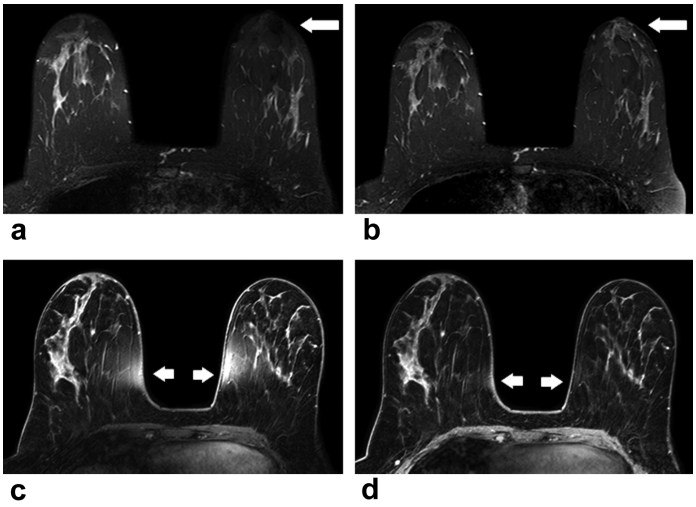

Figure 2.15: **a**: Single-channel transmit T_2-weighted sequence with SPAIR fat suppression, spatial resolution $1 \times 1.3 \times 2.5\,\mathrm{mm}^3$. There is a significantly lower signal intensity and image contrast in the right breast compared with the left (arrow). **b**: Corresponding dual-channel transmit shows a much more homogeneous signal intensity and increased image contrast. **c**: 3D T_1-weighted high-resolution isotropic volume excitation (THRIVE) sequence, $0.9 \times 0.9 \times 0.9\,\mathrm{mm}^3$ spatial resolution. The single-channel transmit shows significant image artifacts from incomplete fat suppression (arrows). **d**: Corresponding images using dual-channel transmit show much more homogeneous fat suppression.

BREAST IMAGING

Left–right differences in image intensity and contrast in imaging the breast are well-known to hamper diagnosis [54]. Fat-suppression also varies spatially, which can cause problems in detecting small lesions. Dual-channel transmit is very effective in reducing both of these types of image artifact, as shown in Fig. 2.15.

2.3. CURRENT STATE-OF-THE-ART AND FUTURE ADVANCES

Dual-channel 3T transmit systems are now offered by most major MR manufacturers, and B_1^+ shimming algorithms are implemented as simple extra calibration scans at the beginning of each examination. Comparison studies with single-channel 3T systems have shown significantly improved diagnostic quality in many applications. Because technology never stands still, we consider here several different areas which may well expand in the future.

IMPROVED AND MORE RAPID B_1^+ MAPPING

A key component to obtaining optimum image quality is the accuracy of the B_1^+ map produced by the B_1^+ calibration sequence, which should also be extremely fast to enable implementation in the clinical routine. Current protocols include methods such as the dual-TR and dual angle method [12, 14] which are not particularly rapid. However, this is an area of active research, with several new schemes being developed which result in

higher sensitivity, more rapid data acquisition and lower SAR: these include using the Bloch-Siegert effect [55] and very rapid dual-stimulated echo approaches [13]. Many of the current sequences are very accurate in mapping areas in which the transmit field is high, but are relatively inaccurate in areas with very low transmit efficiency, which are of course the areas that most need to be improved. B_1^+ mapping sequences with greater "dynamic range" are, therefore, needed to improve the B_1^+ calibration quality, and consequently the B_1^+ shimming performance [56].

ACCURATE SAR ESTIMATION

The estimation of local SAR must be performed extremely rapidly for regular clinical practice. Having determined the B_1^+ shimmed values of the amplitudes and phases of the two independent transmit channels, these values are then used to predict the SAR based on a precalculated SAR database. For a twochannel system, this consists of a simple lookup-table with various shim settings and corresponding SAR values. To better manage the increasing complexity of these SAR models, which can be especially challenging when considering systems with an even higher channel count (>2), so-called Q-matrices have been introduced [19]. A database consisting of a subset of these Q-matrices can then be built up for a set of different subject models (e.g., adult/child, male/female, high/low BMI, tall/short), to provide a rapid estimate of the SAR. The major disadvantages of this approach is that Q-matrices need to be computed for selected body models rather than being patient specific, and they do not account for positional differences (e.g., the patient lying asymmetrically). The computational complexity can also be reduced by methods such as the virtual-observation-point approach [57]. The ultimate aim is to be able to produce an accurate estimate of local SAR based upon, for example, the rapid "localizer prescans" used in every clinical protocol.

COMBINATION WITH OTHER APPROACHES

An alternative, and ultimately complementary, approach to overcoming the conductivity and dielectric effects is the use of high permittivity "dielectric pads." Commercial pads consisting of water-based gels are currently available from some vendors. However, with a relative permittivity ε_r of 80, and a thickness up to 4 cm these are rather bulky while only providing a moderate correction of the B_1^+ field [8, 58]. Much higher permittivity materials ($\varepsilon_r \approx 300$) made from an aqueous suspension of barium titanate [59, 60] have recently been introduced for body imaging at 3T [9]. De Heer et al. [9] showed significantly enhanced contrast homogeneity in liver scans using two symmetrically placed (anterior/posterior) 1 cm thick pads. Brink and Webb [15] have shown that cardiac imaging can be improved by reducing SAR by as much as 50% while increasing B_1^+ homogeneity by using an asymmetric anterior/posterior pad configuration. Both studies indicated that the most consistent imaging quality is obtained by a combination of dual-channel transmit and high permittivity pads, stressing the complementary nature of the two approaches, as demonstrated in Fig. 2.16. Although there are several advantages of such an approach, most particularly the fact that it is platform independent and requires no alterations to imaging sequences etc., there are issues of dielectric placement and patient comfort which need to be considered if these are to be used routinely in clinical practice.

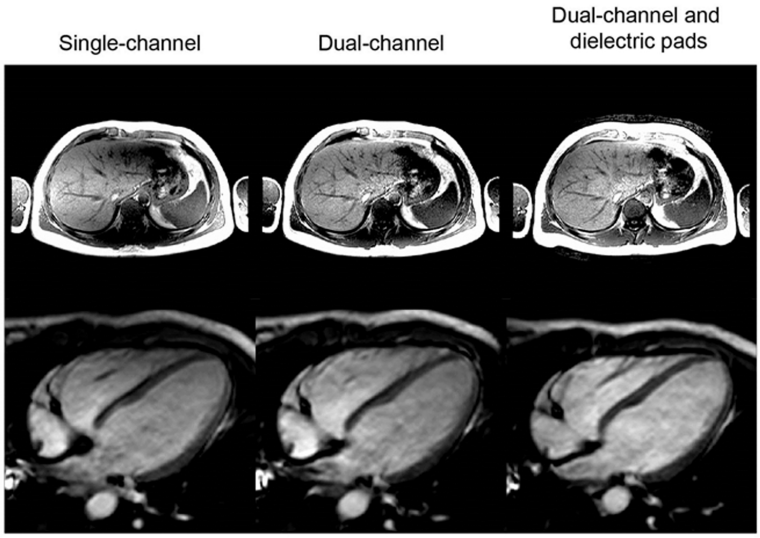

Figure 2.16: Top: Comparison of image quality in an abdominal scan using a single-channel, dual-channel, and dual-channel with high permittivity pads, the last of which gives the highest imaging consistency [9]. Bottom: Similar images from a cardiac scan at 3T, again showing the most consistent image quality from the combined approach [15].

DEVELOPMENT AND EVALUATION OF PARALLEL TRANSMIT SENSE

In contrast to the approach of driving the two channels of the body coil with the same RF pulse shape, independent RF waveforms can be transmitted from each channel: this technique is referred to as "parallel transmit" or "transmit SENSE" [61–63]. In general, this approach enables one to improve the performance of spatially selective multidimensional RF pulses by reducing their length (therefore, reducing T_2^* decay and off-resonance effects), enhancing their spatial definition (for reduced field-of-view imaging), or reducing the RF power deposited in the patient.

Reduced field-of-view imaging, using multidimensional RF pulses in combination with shaped gradients, is a method to increase the spatial resolution achieved per unit data acquisition time [64–66]. It is also a useful technique for minimizing motion artifacts from outside the reduced field-of-view. However, the RF pulses required for this type of application are quite long and this results in the images being very sensitive to artifacts caused by magnetic field inhomogeneities. The length of the pulses can be reduced by transmitting different waveforms on the two different channels. For dual-channel transmit systems the pulse lengths can be approximately halved. This has recently been implemented for zoomed imaging by Siemens under the tradename Syngo ZOOMit, as shown in Fig. 2.17.

The second important application of transmit SENSE is to increase the B_1^+ homogeneity compared with B_1^+ shimming which forms the basis of all of the clinical studies outlined earlier in this study. Transmit SENSE gives an additional degrees of freedom for increasing the B_1^+ homogeneity [68] because two separate waveforms can be used.

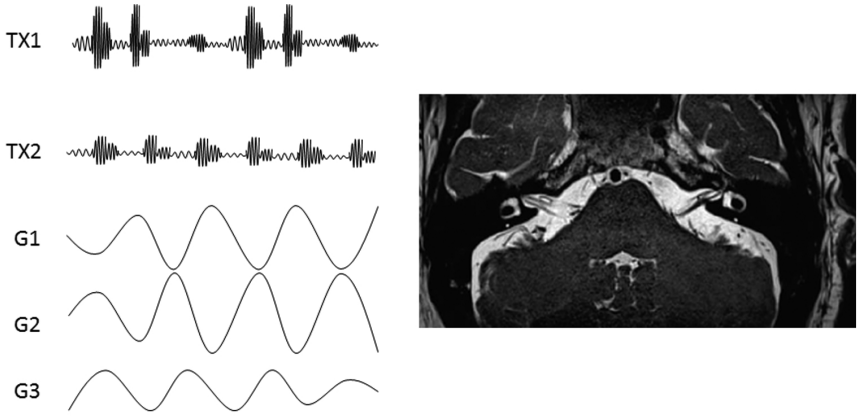

Figure 2.17: Left: Imaging sequence using the full flexibility of a dual-transmit channel system. Completely independent RF waveforms are used for each channel, with appropriate waveforms on all gradient amplifiers for the particular application. Right: Zoomed image of the internal auditory canal from Boada et al. [67].

Several different mathematical methods have been presented for optimizing the pulse shapes of each individual RF pulse and the corresponding gradient waveforms [63, 68–70]. Finally, transmit SENSE can be used either to reduce the local SAR [71, 72] by means of minimizing the mean RF power, or to minimize the peak power required for the RF pulses [73].

The natural extension of the advantages afforded by dual-channel transmit is to increase the channel count further. Potential advantages are: (i) further reduced local SAR allowing shorter overall scan times, (ii) further increases in the B_1^+ homogeneity and image contrast, and (iii) increased flexibility for reduced field-of-view imaging using shorter RF pulses, with the imaging volume more closely matching the geometry of the organs of interest. The major disadvantages are the added complexity of the system, the need for sophisticated multi-element transmit arrays, and the increased computational time for SAR calculations. The architecture of an eight-channel system, with eight independent sources, designed for operation at 3T was described many years ago by Vernickel et al. [71]. In recent work, Childs et al. [74] showed that there was an increase in B_1^+ homogeneity with increasing channel count, although the greatest increase is achieved by going from single to dual-channel transmit. There is a large literature dealing with the system architecture for body imaging at 7 Tesla, with between 8 and 32 transmit channels [75–77]. However, such developments at 3T will require significant financial and resource investment from the major commercial MR vendors, and whether the advantages outweigh the costs remains to be seen.

ACKNOWLEDGEMENTS

We thank Dr. Sjeff Gulpers for providing images for this manuscript.

REFERENCES

[1] Hayes CE, Edelstein WA, Schenck JF, Mueller OM, and Eash M. An efficient highly homogeneous radiofrequency coil for whole-body NMR imaging at 1.5 T. Journal of Magnetic Resonance 1985; 63:622–628.

[2] Vaughan JT, Adriany G, Snyder CJ, Tian J, Thiel T, Bolinger L, Liu H, DelaBarre L, and Ugurbil K. Efficient high-frequency body coil for high-field MRI. Magnetic Resonance in Medicine 2004; 52:851–859.

[3] Schick F. Whole-body MRI at high field: technical limits and clinical potential. European Radiology 2005; 15:946–959.

[4] Bernstein MA, Huston J, and Ward HA. Imaging artifacts at 3.0T. Journal of Magnetic Resonance Imaging 2006; 24:735–746.

[5] Chang KJ, and Kamel IR. Abdominal imaging at 3T: challenges and solutions. Applied Radiology 2010; 22–31.

[6] Cornfeld D, and Weinreb J. Simple changes to 1.5-T MRI abdomen and pelvis protocols to optimize results at 3 T. American Journal of Roentgenology 2008; 190:W140–W150.

[7] Sled JG, and Pike GB. Standing-wave and RF penetration artifacts caused by elliptic geometry: an electrodynamic analysis of MRI. IEEE Transactions on Medical Imaging 1998; 17:653–662.

[8] Franklin KM, Dale BM, and Merkle EM. Improvement in B1-inhomogeneity artifacts in the abdomen at 3T MR imaging using a radiofrequency cushion. Journal of Magnetic Resonance Imaging 2008; 27:1443–1447.

[9] de Heer P, Brink WM, Kooij BJ, and Webb AG. Increasing signal homogeneity and image quality in abdominal imaging at 3 T with very high permittivity materials. Magnetic Resonance in Medicine 2012; 68:1317–1324.

[10] Wust P, Nadobny J, Felix R, Deuflhard P, Louis A, and John W. Strategies for Optimized Application of Annular-Phased-Array Systems in Clinical Hyperthermia. International Journal of Hyperthermia 1991; 7:157–173.

[11] Krishnamurthy R, Pednekar A, Kouwenhoven M, Cheong B, and Muthupillai R. Evaluation of a Subject specific dual-transmit approach for improving B1 field homogeneity in cardiovascular magnetic resonance at 3T. Journal of Cardiovascular Magnetic Resonance 2013; 15:68.

[12] Cunningham CH, Pauly JM, and Nayak KS. Saturated double-angle method for rapid B1+ mapping. Magnetic Resonance in Medicine 2006; 55:1326–1333.

[13] Nehrke K, and Börnert P. DREAM—A Novel Approach for Robust, Ultrafast, Multislice B1 Mapping. Magnetic Resonance in Medicine 2012; 68:1517–1526.

[14] Yarnykh VL. Optimal radiofrequency and gradient spoiling for improved accuracy of T1 and B1 measurements using fast steady-state techniques. Magnetic Resonance in Medicine 2010; 63:1610–1626.

[15] Brink WM, and Webb AG. High permittivity pads reduce specific absorption rate, improve B1 homogeneity, and increase contrast-to-noise ratio for functional cardiac MRI at 3 T. Magnetic Resonance in Medicine 2014; 71:1632–1640.

[16] Christ A, Kainz W, Hahn EG, Honegger K, Zefferer M, Neufeld E, Rascher W, Janka R, Bautz W, Chen J, Kiefer B, Schmitt P, Hollenbach HP, Shen J, Oberle M, Szczerba D, Kam A, Guag JW, and Kuster N. The Virtual Family—development of surface-based anatomical models of two adults and two children for dosimetric simulations. Physics in Medicine and Biology 2010; 55:N23–38.

[17] Food and Drug Administration. Guidance for Industry and Food and Drug Administration Staff - Criteria for Significant Risk Investigations of Magnetic Resonance Diagnostic Devices. Silver Spring, MD: FDA; 2008.

[18] International Electrotechnical Commission. Particular requirements for the basic safety and essential performance of magnetic resonance equipment for medical diagnosis. IEC 60601-2-33, 3rd ed., Geneva, Switzerland; 2010.

[19] Graesslin I, Homann H, Biederer S, Börnert P, Nehrke K, Vernickel P, Mens G, Harvey P, and Katscher U. A Specific Absorption Rate Prediction Concept for Parallel Transmission MR. Magnetic Resonance in Medicine 2012; 68:1664–1674.

[20] Seifert F, Wübbeler G, Junge S, Ittermann B, and Rinneberg H. Patient safety concept for multichannel transmit coils. Journal of Magnetic Resonance Imaging 2007; 26:1315–1321.

[21] Mao W, Wang Z, Smith MB, and Collins CM. Calculation of SAR for Transmit Coil Arrays. Concepts in Magnetic Resonance Part B: Magnetic Resonance Engineering 2007; 31B:127–131.

[22] van den Berg CAT, van den Bergen B, van de Kamer JB, Raaymakers BW, Kroeze H, Bartels LW, and Lagendijk JJW. Simultaneous B1+ Homogenization and Specific Absorption Rate Hotspot Suppression Using a Magnetic Resonance Phased Array Transmit Coil. Magnetic Resonance in Medicine 2007; 57:577–586.

[23] Willinek WA, Gieseke J, Kukuk GM, Nelles M, König R, Morakkabati-Spitz N, Träber F, Thomas D, Kuhl CK, and Schild HH. Dual-source parallel radiofrequency excitation body MR imaging compared with standard MR imaging at 3.0 T: initial clinical experience. Radiology 2010; 256:966–975.

[24] Mueller A, Kouwenhoven M, Naehle CP, Gieseke J, Strach K, Willinek WA, Schild HH, and Thomas D. Dual-source radiofrequency transmission with patient-adaptive local radiofrequency shimming for 3.0-T cardiac MR imaging: initial experience. Radiology 2012; 263:77–85.

[25] Cheng ASH, Pegg TJ, Karamitsos TD, Searle N, Jerosch-Herold M, Choudhury RP, Banning AP, Neubauer S, Robson MD, and Selvanayagam JB. Cardiovascular magnetic resonance perfusion imaging at 3-tesla for the detection of coronary artery disease: a comparison with 1.5-tesla. Journal of the American College of Cardiology 2007; 49:2440–2449.

[26] Thomas D, Strach K, Meyer C, Naehle CP, Schaare S, Wasmann S, Schild HH, and Sommer T. Combined myocardial stress perfusion imaging and myocardial stress tagging for detection of coronary artery disease at 3 Tesla. Journal of Cardiovascular Magnetic Resonance 2008; 10:59.

[27] Sung K, and Nayak KS. Measurement and Characterization of RF Nonuniformity Over the Heart at 3T Using Body Coil Transmission. Journal of Magnetic Resonance Imaging 2008; 27:643–648.

[28] Barkhausen J, Ruehm SG, Goyen M, Buck T, Laub G, and Debatin JF. MR evaluation of ventricular function: true fast imaging with steady-state precession versus fast low-angle shot cine MR imaging: feasibility study. Radiology 2001; 219:264–269.

[29] Greenman RL, Shirosky JE, Mulkern RV, and Rofsky NM. Double Inversion Black-Blood Fast Spin-Echo Imaging of the Human Heart: A Comparison Between 1.5T and 3.0T. Journal of Magnetic Resonance Imaging 2003; 17:648–655.

[30] Gutberlet M, Noeske R, Schwinge K, Freyhardt P, Felix R, and Niendorf T. Comprehensive cardiac magnetic resonance imaging at 3.0 Tesla: feasibility and implications for clinical applications. Investigative Radiology 2006; 41:154–167.

[31] Zhai Z, De Meester GD, Morich MA, and Harvey PR. MR involving high speed coil mode switching between I-channel linear, Q-channel linear, quadrature and anti-quadrature modes. Patent WO2007/12426. 2007.

[32] Jia H, Wang C, Wang G, Qu L, Chen W, Chan Q, and Zhao B. Impact of 3.0 T Cardiac MR Imaging Using Dual-Source Parallel Radiofrequency Transmission with Patient-Adaptive B1 Shimming. PloS one 2013; 8:e66946.

[33] Strach K, Clauberg R, Müller A, Wonneberger U, Naehle CP, Kouwenhoven M, Gieseke J, Schild HH, and Thomas D. Feasibility of high-dose dobutamine stress SSFP Cine MRI at 3 Tesla with patient adaptive local RF Shimming using dual-source RF transmission: initial results. RöFo - Fortschritte auf dem Gebiete der Röntgenstrahlen und der Nuklearmedizin 2013; 185:34–39.

[34] Nelles M, König RS, Gieseke J, Guerand-van Battum MM, Kukuk GM, Schild HH, and Willinek WA. Dual-source parallel RF transmission for clinical MR imaging of the spine at 3.0 T: intraindividual comparison with conventional single-source transmission. Radiology 2010; 257:743–753.

[35] Filippi CG, Carlson M, Johnson JM, Burbank HN, Alsofrom GF, and Andrews T. Improvements in lumbar spine MRI at 3 T using parallel transmission. American Journal of Roentgenology 2012; 199:861–867.

[36] Filippi CG, Duncan CT, Watts R, Nickerson JP, Gonyea JV, Hipko SG, and Andrews T. In vivo quantification of T1ρ in lumbar spine disk spaces at 3 T using parallel transmission MRI. American Journal of Roentgenology 2013; 201:W110–6.

[37] Merkle EM, and Dale BM. Abdominal MRI at 3.0 T: The basics revisited. American Journal of Roentgenology 2006; 186:1524–1532.

[38] Schindera ST, Merkle EM, Dale BM, Delong DM, and Nelson RC. Abdominal Magnetic Resonance Imaging at 3.0 T: what is the ultimate gain in signal-to-noise ratio? Academic radiology 2006; 13:1236–1243.

[39] von Falkenhausen MM, Lutterbey G, Morakkabati-Spitz N, Walter O, Gieseke J, Blömer R, Willinek WA, Schild HH, and Kuhl CK. High-field-strength MR imaging of the liver at 3.0 T: intraindividual comparative study with MR imaging at 1.5 T. Radiology 2006; 241:156–166.

[40] Lee VS, Hecht EM, Taouli B, Chen Q, Prince K, and Oesingmann N. Body and cardiovascular MR imaging at 3.0 T. Radiology 2007; 244:692–705.

[41] Chang JM, Lee JM, Lee MW, Choi JY, Kim SH, Lee JY, Han JK, and Choi BI. Superparamagnetic iron oxide-enhanced liver magnetic resonance imaging: comparison of 1.5 T and 3.0 T imaging for detection of focal malignant liver lesions. Investigative Radiology 2006; 41:168–174.

[42] Ramalho M, Herédia V, Tsurusaki M, Altun E, and Semelka RC. Quantitative and qualitative comparison of 1.5 and 3.0 Tesla MRI in patients with chronic liver diseases. Journal of Magnetic Resonance Imaging 2009; 29:869–879.

[43] Tsurusaki M, Semelka RC, Zapparoli M, Elias J, Altun E, Pamuklar E, and Sugimura K. Quantitative and qualitative comparison of 3.0T and 1.5T MR imaging of the liver in patients with diffuse parenchymal liver disease. European Journal of Radiology 2009; 72:314–320.

[44] Kukuk GM, Gieseke J, Weber S, Hadizadeh DR, Nelles M, Träber F, Schild HH, and Willinek WA. Focal liver lesions at 3.0 T: lesion detectability and image quality with T2-weighted imaging by using conventional and dual-source parallel radiofrequency transmission. Radiology 2011; 259:421–428.

[45] Luo W, Lanagan MT, Sica CT, Ryu Y, Oh S, Ketterman M, Yang QX, and Collins CM. Permittivity and performance of dielectric pads with sintered ceramic beads in MRI: early experiments and simulations at 3 T. Magnetic Resonance in Medicine 2013; 70:269–275.

[46] Mürtz P, Kaschner M, Träber F, Kukuk GM, Büdenbender SM, Skowasch D, Gieseke J, Schild HH, and Willinek WA. Evaluation of dual-source parallel RF excitation for diffusion-weighted whole-body MR imaging with background body signal suppression at 3.0 T. European Journal of Radiology 2012; 81:3614–3623.

[47] Mürtz P, Kaschner M, Träber F, Kukuk G, Skowasch D, Gieseke J, Schild HH, and Willinek WA. Diffusion-weighted whole-body MRI with background body signal suppression: technical improvements at 3.0 T. Journal of Magnetic Resonance Imaging 2012; 35:456–461.

[48] Riffel P, Rao RK, Haneder S, Meyer M, Schoenberg SO, and Michaely HJ. Impact of field strength and RF excitation on abdominal diffusion-weighted magnetic resonance imaging. World Journal of Radiology 2013; 5:334–344.

[49] Rao RK, Riffel P, Meyer M, Kettnaker PJ, Lemke A, Haneder S, Schoenberg SO, and Michaely HJ. Implementation of dual-source RF excitation in 3 T MR-scanners allows for nearly identical ADC values compared to 1.5 T MR scanners in the abdomen. PloS one 2012; 7:e32613.

[50] Padhani AR, Liu G, Koh DM, Chenevert TL, Thoeny HC, Takahara T, Dzik-Jurasz A, Ross BD, Van Cauteren M, Collins D, Hammoud DA, Rustin GJS, Taouli B, and Choyke PL. Diffusion-weighted magnetic resonance imaging as a cancer biomarker: consensus and recommendations. Neoplasia 2009; 11:102–125.

[51] Kwee TC, Takahara T, Ochiai R, Katahira K, Van Cauteren M, Imai Y, Nievelstein RAJ, and Luijten PR. Whole-body diffusion-weighted magnetic resonance imaging. European Journal of Radiology 2009; 70:409–417.

[52] Kwee TC, Takahara T, Ochiai R, Koh DM, Ohno Y, Nakanishi K, Niwa T, Chenevert TL, Luijten PR, and Alavi A. Complementary roles of whole-body diffusion-weighted MRI and 18F-FDG PET: the state of the art and potential applications. Journal of Nuclear Medicine 2010; 51:1549–1558.

[53] Takahara T, Imai Y, Yamashita T, Yasuda S, Nasu S, and Van Cauteren M. Diffusion weighted whole body imaging with background body signal suppression (DWIBS): technical improvement using free breathing, STIR and high resolution 3D display. Radiation Medicine 2004; 22:275–282.

[54] Kuhl CK, Kooijman H, Gieseke J, and Schild HH. Effect of B1 inhomogeneity on breast MR imaging at 3.0 T. Radiology 2007; 244:929–930.

[55] Sacolick LI, Wiesinger F, Hancu I, and Vogel MW. B1 mapping by Bloch-Siegert shift. Magnetic Resonance in Medicine 2010; 63:1315–1322.

[56] Brunner DO, and Pruessmann KP. B1(+) interferometry for the calibration of RF transmitter arrays. Magnetic Resonance in Medicine 2009; 61:1480–1488.

[57] Eichfelder G, and Gebhardt M. Local specific absorption rate control for parallel transmission by virtual observation points. Magnetic Resonance in Medicine 2011; 66:1468–1476.

[58] Sreenivas M, Lowry M, Gibbs P, Pickles M, and Turnbull LW. A simple solution for reducing artefacts due to conductive and dielectric effects in clinical magnetic resonance imaging at 3 T. European Journal of Radiology 2007; 62:143–146.

[59] Teeuwisse WM, Brink WM, Haines KN, and Webb AG. Simulations of high permittivity materials for 7 T neuroimaging and evaluation of a new barium titanate-based dielectric. Magnetic Resonance in Medicine 2012; 67:912–918.

[60] Teeuwisse WM, Brink WM, and Webb AG. Quantitative assessment of the effects of high-permittivity pads in 7 Tesla MRI of the brain. Magnetic Resonance in Medicine 2012; 67:1285–1293.

[61] Katscher U, Börnert P, Leussler C, and van den Brink JS. Transmit SENSE. Magnetic Resonance in Medicine 2003; 49:144–150.

[62] Zhu Y. Parallel excitation with an array of transmit coils. Magnetic Resonance in Medicine 2004; 51:775–784.

[63] Katscher U, and Börnert P. Parallel RF transmission in MRI. NMR in Biomedicine 2006; 19:393–400.

[64] Pauly J, Nishimura D, and Macovski A. A k-space analysis of small-tip-angle excitation. Journal of Magnetic Resonance 1989; 81:43–56.

[65] Börnert P, and Schäffter T. Curved slice imaging. Magnetic Resonance in Medicine 1996; 36:932–939.

[66] Hardy CJ, and Cline HE. Spatial localization in two dimensions using NMR designer pulses. Journal of Magnetic Resonance 1989; 82:647–654.

[67] Boada F, Shepherd T, Rosenkrantz A, Sigmund EE, Fütterer J, Chandarana H, Hagiwara M, Rusinek H, Mikheev A, Bruno M, Geppert C, Glielmi C, and Pfeuffer J. Parallel Transmission and its Clinical Implementation: Enabling new Clinical Imaging Paradigms. Magnetom Flash 2013; 2:104–110.

[68] Grissom W, Yip CY, Zhang Z, Stenger VA, Fessler JA, and Noll DC. Spatial domain method for the design of RF pulses in multicoil parallel excitation. Magnetic Resonance in Medicine 2006; 56:620–629.

[69] Grissom WA, Yip CY, Wright SM, Fessler JA, and Noll DC. Additive angle method for fast large-tip-angle RF pulse design in parallel excitation. Magnetic Resonance in Medicine 2008; 59:779–787.

[70] Grissom WA, Xu D, Kerr AB, Fessler JA, and Noll DC. Fast large-tip-angle multidimensional and parallel RF pulse design in MRI. IEEE Transactions on Medical Imaging 2009; 28:1548–1559.

[71] Vernickel P, Roschmann P, Findeklee C, Ludeke KM, Leussler C, Overwag J, Katscher U, Graesslin I, and Schunemann K. Eight-channel transmit/receive body MRI coil at 3T. Magnetic Resonance in Medicine 2007; 58:381–389.

[72] Graesslin I, Niemann M, Harvey P, Vernickel P, and Katscher U. SAR and RF power reduction parallel excitation using non-cartesian trajectories. Magnetic Resonance Materials in Physics Biology and Medicine 2005; 18:S251.

[73] Yip CY, Fessler JA, and Noll DC. Iterative RF pulse design for multidimensional, small-tip-angle selective excitation. Magnetic Resonance in Medicine 2005; 54:908–917.

[74] Childs AS, Malik SJ, O'Regan DP, and Hajnal JV. Impact of number of channels on RF shimming at 3T. Magma 2013; 26:401–410.

[75] Vaughan JT, Snyder CJ, DelaBarre LJ, Bolan PJ, Tian J, Bolinger L, Adriany G, Andersen P, Strupp J, and Ugurbil K. Whole-body imaging at 7T: preliminary results. Magnetic Resonance in Medicine 2009; 61:244–248.

[76] Kraff O, Bitz AK, Kruszona S, Orzada S, Schaefer LC, Theysohn JM, Maderwald S, Ladd ME, and Quick HH. An eight-channel phased array RF coil for spine MR imaging at 7 T. Investigative Radiology 2009; 44:734–740.

[77] Graessl A, Renz W, Hezel F, Dieringer Ma, Winter L, Oezerdem C, Rieger J, Kellman P, Santoro D, Lindel TD, Frauenrath T, Pfeiffer H, and Niendorf T. Modular 32-channel transceiver coil array for cardiac MRI at 7.0T. Magnetic Resonance in Medicine 2014; 72:276–290.

Chapter 3

High Permittivity Pads Reduce SAR, Improve B_1^+ Homogeneity, and Increase Contrast-to-Noise Ratio for Functional Cardiac MRI at 3T

Magn Reson Med 2014;71:1632–1640

Wyger M. Brink
Andrew G. Webb

ABSTRACT

Purpose: To improve image quality and reduce specific absorption rate in functional cardiac imaging at 3T.

Methods: Two high permittivity dielectric pads on the anterior and posterior sides of the thorax were numerically designed and implemented using an aqueous suspension of barium titanate. The effects on the average transmit efficiency, B_1^+ homogeneity, reception sensitivity, and contrast-to-noise ratio were verified in vivo on a dual-transmit system with the body coil driven in conventional quadrature and radiofrequency shimmed mode.

Results: Statistically significant improvements in average transmit efficiency, B_1^+ homogeneity, and contrast-to-noise ratio were measured in healthy volunteers ($n = 11$) with body mass indices between 20.3 and 34.9 kg/m^2. Simulations show that no radiofrequency hot spots are introduced by the dielectric material.

Conclusion: High permittivity pads are shown to reduce specific absorption rate, improve B_1^+ homogeneity, and increase contrast-to-noise ratio in functional cardiac magnetic resonance at 3T. The results presented in this work show that the current approach is more effective than dual-channel radiofrequency shimming.

3.1. INTRODUCTION

Increasing the field strength from 1.5 to 3T has been shown to increase both the signal-to-noise ratio (SNR) and contrast-to-noise ratio (CNR) for cardiac magnetic resonance imaging (MRI), improving the trade-off between temporal resolution, spatial resolution, and SNR [1, 2]. In general, however, the overall image quality is not improved due to the increased static (B_0) and radiofrequency (RF; B_1^+) magnetic field inhomogeneities which lead to susceptibility artifacts and contrast variations or "shading," respectively. In particular, the balanced steady-state free precession (bSSFP) sequence, which is the "workhorse" in functional cardiac imaging at 1.5T, suffers from increased susceptibility artifacts or "dark bands" at 3T, with the spacing between the bands being proportional to the resonance offset frequency and inversely proportional to the repetition time (TR). If the TR for 3T scanning could be reduced, then these artifacts could be improved: however, the approximate fourfold increase in specific absorption rate (SAR) in going from 1.5 to 3T limits the minimum achievable TR at 3T, meaning that 1.5T is still the preferred field strength for functional cardiac MR.

Recent advances in static and RF shimming (using multiple-transmit systems) have been shown to be able to overcome some of these technical challenges. Higher-order static and dynamic shimming of the static magnetic field has been shown to reduce significantly susceptibility artifacts in the heart [3–5]. The higher-order B_0 correction, however, can lead to increases in the resonance frequency offset outside the region-ofinterest (ROI), decreasing the overall image quality. Dual-transmit systems have recently become commercially available for 3T and show a substantial improvement in the B_1^+ homogeneity within the heart and a reduction in SAR which allows a reduction of the TR in bSSFP sequences, reducing the susceptibility artifacts [6, 7].

Previous studies have shown the potential of improving B_1^+ homogeneity in volume coils by using high permittivity materials. At 3 and 7T, these materials have shown to improve the global B_1^+ homogeneity and reduce the required RF power level [8–11]. High permittivity materials have also proved useful for locally enhancing SNR and reducing SAR for head and neck imaging at 3T as well as 7T [12, 13]. Although the optimization of RF shimming using multiple sources has been studied for many years [14–17], design studies have not been reported using high permittivity materials for local RF shimming.

To date, there is no closed form solution for the design of dielectric pads. One can, however, perform parameterized numerical computations within a limited parameter space to address most of the practical degrees-of-freedom such as the material properties, dimensions, and positioning. This method has been applied in the past to assess the effects of the permittivity on the B_1^+ distribution [9, 11]. However, no design studies oriented toward the geometry of the dielectric pads have been reported so far. Some qualitative insight for setting the parameter space can be derived from intuitive formulations of the effect of a dielectric material used for RF shimming. One way of explaining this is through the currents induced in the dielectric which can be regarded as secondary sources that generate a secondary field [10, 18, 19]. The superposition of this secondary field and the primary field (without pads) determines the final B_1^+ distribution. Based on these mechanisms, one can relate the magnitude of the secondary field being proportional to the permittivity of the material and the volume of the dielectric pad. This implies that using a dielectric material with a permittivity as high as possible is benefi-

cial because a smaller geometry can then be considered, which is more comfortable and convenient for the patient. Based on the spatial decay of the secondary field, which is a result of both Sommerfeld's radiation condition and absorption in the human body, one can expect this secondary field to be strongest close to the dielectric material. This indicates that the material should be applied as close to the ROI as possible. A dielectric pad on the anterior side of the thorax would therefore provide the most effective gain in B_1^+ as the heart is located more toward the anterior side of the thorax. The spatial decay of the secondary field introduced by an anterior pad indicates that at some point additional material on the posterior side can be beneficial for correcting this spatial decay in the heart ROI. In the limit, interference between the secondary field and the primary field indicates the need for balancing both pad thicknesses such that best B_1^+ homogeneity in the heart region is achieved.

In this work, we present high permittivity pads tailored for reducing SAR and improving B_1^+ homogeneity in cardiac MRI at 3T. Due to the localized nature of the heart, a different pad size and thickness needs to be considered than in the case where one aims on maximizing global B_1^+ homogeneity in the entire imaging slice [11]. By using an aqueous suspension of barium titanate, a large number of degrees of freedom (relative permittivity, size, geometry, and placement) can be used for locally tailoring the RF field distribution. Numerical design results and simulations of the local SAR effects are presented. The effects of the dielectric pads on the average transmit efficiency, B_1^+ homogeneity, average RF power, and CNR are validated in vivo. The performance with and without high permittivity pads is experimentally compared with dual-transmit RF shimming, as well as the combined operation of dual-transmit RF shimming with the high permittivity pads in place.

3.2. METHODS

RF SIMULATIONS

The transmit B_1^+ field and SAR distribution in a 3T body coil was simulated using commercially available software (xFDTD, version 7.2, Remcom Inc., State College, PA). The body coil was modeled as a 16-rung high-pass birdcage numerically tuned using lumped elements and driven in conventional quadrature mode by two matched feed points. The tuning capacitors had a capacitance of 26.48 pF and a series resistance of 0.1 Ω to account for coil losses [20]. The length of the birdcage was 50 cm, the rung length was 40 cm, and the diameter was 61 cm. The shield had a length of 100 cm and a diameter of 67 cm. A male and female subject were modeled by Virtual Family members "Duke" and "Ella" with appropriate material properties assigned to each tissue type (IT'IS Foundation, Zurich, Switzerland [21]). B_1^+ field data were normalized to 1 kW of accepted power.

The simulations were performed using a 2.5-mm^3 isotropic grid terminated with a seven-cell perfectly matched layer (PML) boundary condition. Numerical convergence of the parameters of interest (such as local SAR) was verified by simulating the configuration for a time frame up to 0.7 μs in steps of 0.05 μs. All parameters of interest converged within 1% for a time frame of 0.5 μs or longer, which was then used in all simulations. The computations were performed on an Intel Xeon six-core 2.80-GHz processor equipped with an NVIDIA Tesla C1060-GPU acceleration card.

PARAMETRIC NUMERICAL DESIGN

A dielectric padding on the anterior and posterior side of the thorax was numerically designed using both the male and female body model. The objectives of the design were twofold. The first objective was to maximize the average transmit efficiency (η), defined as the mean B_1^+ per square root of accepted power, and the second objective was to minimize the B_1^+ inhomogeneity (σ), defined as the standard deviation of the B_1^+ divided by its mean value, over the entire three-dimensional (3D) heart volume. The degrees of freedom were restricted to the dimensions (width, height, and thickness), permittivity, and position of the pads. To further reduce the degrees of freedom, a baseline configuration was chosen consisting of two pads of dimensions 20-by-20 cm with a relative permittivity of 300 placed on the front and back of the thorax centered at the heart. From this baseline configuration, a feasible set of geometries was created by varying the thickness of both pads from 0 to 20 mm in steps of 2.5 mm. Additional variations in the size and the position of the pads were performed to verify this baseline geometry. First, the width and length of the anterior and posterior pads were varied from 15 to 25 cm in steps of 2.5 cm while maintaining a thickness of 15 and 10 mm, respectively. Then, the position of the pads was varied by introducing an offset of ± 3 and ± 5 cm in both the x- and z-direction.

Both design objectives were combined into a figure of merit (F) by taking a weighted sum of the gain in average transmit efficiency and B_1^+ homogeneity. This is formally expressed as

$$F(d_1, d_2) = w_1 \cdot \eta(d_1, d_2)/\eta(0,0) + w_2 \cdot (1 - \sigma(d_1, d_2))$$

in which $\eta(d_1, d_2)$ denotes the average transmit efficiency and $\sigma(d_1, d_2)$ denotes the B_1^+ inhomogeneity in the heart ROI for anterior pad thickness d_1 and posterior pad thickness d_2 . In our case, we chose $w_1 = 0.2$ and $w_2 = 0.8$, which means that B_1^+ homogeneity is emphasized in designing the dielectric pads, however, this choice is free to the operator. The rationale for favoring B_1^+ homogeneity in this respect is to improve the consistency in image quality for subjects with a similar body geometry.

SAR ANALYSIS

With the introduction of high permittivity material into the configuration, care needs to be taken to ensure that this does not lead to any RF hot spots that exceed the safety limit. Regulatory limits are issued by the International Electrotechnical Commission for the global SAR, defined as the whole body average SAR, and the local SAR, defined as the spatial-average SAR over any 10 g of tissue [22]. A further differentiation is made between local SAR in the head, torso, and extremities. SAR simulations were run for both the male and female body model with and without pads to assess the implications on SAR. Care was taken to keep the dielectric pads and the body separated by 1 mm to incorporate the separation effect due to the plastic encasing of the dielectric material and the subject's clothing. For implementing this separation distance, the mesh resolution was increased to 1 mm around the pads.

DIELECTRIC PADS

The dielectric pads were constructed using a suspension of barium titanate (–325 mesh powder, Alfa Aesar GmbH & Co. KG, Karlsruhe, Germany) in distilled deionized water. The dielectric pads were intentionally protonated for verifying their position during the scans. A very dense mixture of 4:1 barium titanate-to-water (mass/mass ratio) was created for obtaining a dielectric constant as high as possible, while keeping the production process tractable. The resulting dielectric material was characterized using a dielectric probe kit (85070E, Agilent Technologies, Santa Clara, CA) and was found to have a relative permittivity of 293 and electrical conductivity of 0.473 S/m at 128 MHz. The mixture was heatsealed in polypropene using a manual sealer (420 SBM2, Audion Elektro, Weesp, The Netherlands) to form rectangular pads.

MRI SYSTEM AND PROTOCOLS

In vivo experiments were performed on a Philips Achieva 3T TX system (Philips Healthcare, Best, The Netherlands) equipped with dual-transmit technology. Four series of scans were performed by driving the body coil in quadrature or dual-transmit mode, both with and without the dielectric pads in place. Before scanning, the dielectric pads were positioned underneath and on top of the subject's thorax, centered at the heart. A 6-s scout scan was run to ensure proper positioning of the dielectric pads. After scanning in quadrature and dual-transmit mode, the dielectric pads were removed and the protocol was repeated without pads. For reception, a six-channel coil array was used with three elements on the anterior and three elements on the posterior side. First-order B_0 shimming was performed on an angulated cube covering the heart, and RF shimming in the dual-transmit mode was performed on the same volume using the vendor-supplied RF shimming routine. All scans were cardiac-gated using a peripheral pulse sensor. Quantitative analysis of the data was performed using in-house developed Mass analysis software (Leiden University Medical Center, Leiden, The Netherlands [23]). To perform a statistical analysis on the intersubject-variability, data were collected in a cohort of 11 volunteers (six female, five male), with a mean body mass index of 23.5 ± 4.7 kg/m^2 (mean ± standard deviation), all body mass indices falling between 20.3 and 34.9 kg/m^2. Statistical significance was evaluated using a double-sided paired t-test, in which a $P < 0.05$ was considered to indicate a statistically significant difference. The study was approved by the institution's ethics board and written informed consent was obtained.

TRANSMIT EFFICIENCY AND RECEPTION SENSITIVITY MEASUREMENT

B_1^+ maps were acquired in the transverse and sagittal plane using a saturated double-angle method with a nominal tip angle of 40° [24]. The spatial resolution was set to 5 × 5 mm^2 with a slice thickness of 10 mm. The B_1^+ maps were converted to transmit efficiency maps by dividing by the square root of the accepted RF power measured at the output of the amplifiers. We note that this includes the power absorbed in the RF chain, which can amount to almost 50% of the reported value [20]. Therefore, only a relative comparison with the simulations is possible. The transmit efficiency maps were analyzed by manual segmentation to obtain the average transmit efficiency and B_1^+ inhomogeneity in the heart. Reception sensitivity maps were obtained using a cardiac triggered 3D gradient-echo sequence with a tip angle of five degrees, geometrically aligned with the B_1^+ map.

The resulting signal intensity is proportional to the product of the reception sensitivity and the B_1^+ [25]. The ratio of the 3D gradient-echo image and the B_1^+ map then yielded the reception sensitivity map in arbitrary units. The effects on the average RF power were verified by running a bSSFP sequence along the short axis of the heart and recording the accepted RF power time-averaged over 30 s of the sequence. The tip angle was set to 40° and the imaging resolution was set to 2×1.6 mm^2 with a slice thickness of 8 mm. Sensitivity encoding was enabled with a reduction factor of 2. The TR was set to the shortest allowed by the system, typically in the range of 2.5-3.0 ms.

CNR MEASUREMENT

The effect of the dielectric pads on the CNR was assessed through a dynamic noise scan planned along the short axis of the heart. In this scan, two bSSFP dynamics are acquired, the second one without RF pulses and gradients resulting in an image that contains only uniform noise. Both scans were reconstructed with identical reconstruction parameters. The same resolution was applied as in the bSSFP sequence. Reconstruction was performed without sensitivity encoding to obtain a uniform noise image. The mean signal in the interventricular septum and left ventricular cavity was determined by manually drawing an ROI of approximately 4 cm^2 in both areas. The absolute difference was then divided by the standard deviation of the noise image to obtain the CNR.

3.3. RESULTS

PARAMETRIC NUMERICAL DESIGN

The results from the parametric numerical design study are shown for both the male and female body model in Fig. 3.1. As can be seen from the transmit efficiency maps, the anterior pad is most effective for increasing the average transmit efficiency; however, best B_1^+ homogeneity is achieved when the thickness of both pads is correctly balanced. It can be seen that the best geometry for maximizing the average transmit efficiency does not correspond to the best geometry for minimizing the B_1^+ inhomogeneity. This reflects a trade-off between B_1^+ homogeneity and SAR, which has been observed in RF shimming using multiple sources as well [16]. The figure of merit (F) weighs both performance measures and indicates a single optimum at a thickness of 15 mm for the anterior and 10 mm for the posterior pad. This configuration increased the average transmit efficiency by 38% from 5.8 to 8.0 $\mu T/\sqrt{kW}$ and reduced the B_1^+ inhomogeneity from 13.8 to 6.9%.

Additional simulations were performed to verify the size and position of the pads, and confirmed that the baseline geometry of the pads was properly chosen. The position variations indicated that the B_1^+ inhomogeneity is sensitive to the position of the anterior pad. A position error of 3 cm increased the B_1^+ inhomogeneity up to 8.0% and an offset of 5 cm increased the B_1^+ inhomogeneity up to 9.9%. This implies that to ensure consistent image quality, which is mainly depending on B_1^+ homogeneity, large positioning errors need to be corrected. The size variations indicated a smooth optimum around 20-by-20 cm with all values for the B_1^+ inhomogeneity being less than 8.9%.

Design of the dielectric pads using the female body model resulted in the same geometry of the pads. In this case, the pads increased the average transmit efficiency by 31% from 8.1 to 10.6 $\mu T/\sqrt{kW}$. The B_1^+ inhomogeneity was reduced from 11.0 to 6.4%.

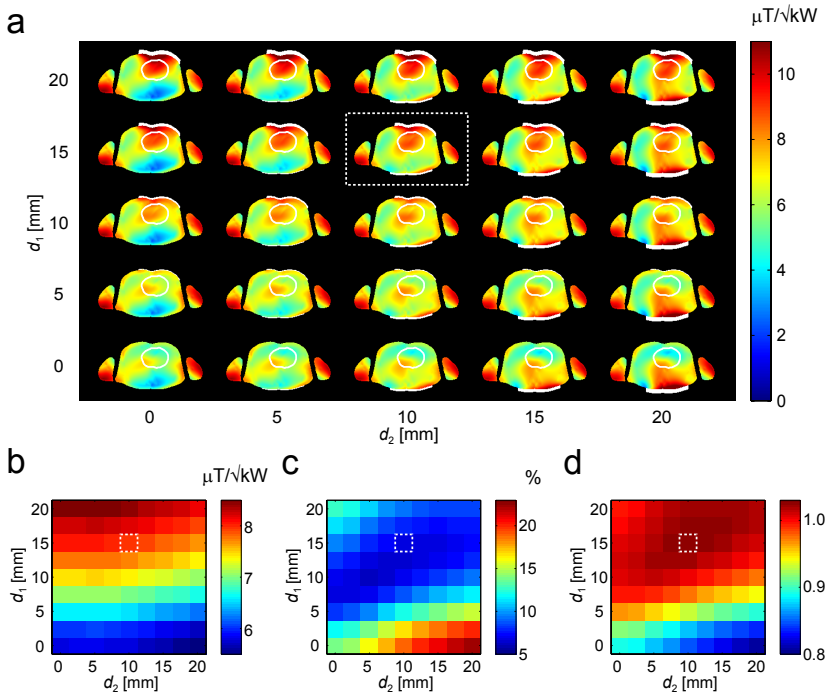

Figure 3.1: Variational maps showing the simulated transmit efficiency in the transverse plane (**a**), average transmit efficiency (**b**), B_1^+ inhomogeneity (**c**), and the figure of merit (F) (**d**) for anterior pad thickness d_1 and posterior pad thickness d_2. The anterior pad is clearly most effective for increasing the average transmit efficiency, whereas for improving the B_1^+ homogeneity, both thicknesses need to be correctly balanced. The best performance was obtained for an anterior pad thickness of 15 mm and posterior pad thickness of 10 mm, which has been encircled in white. The heart and dielectric pads are illustrated in white.

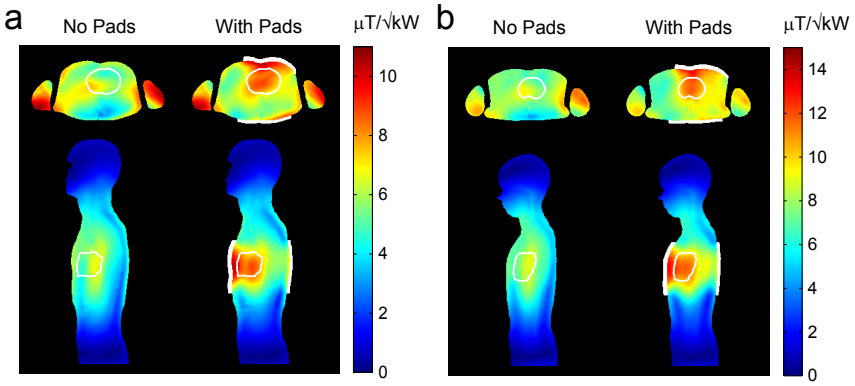

Figure 3.2: Transverse (top) and sagittal (bottom) cross section of the simulated transmit efficiency without (left) and with (right) the dielectric pads in the male (**a**) and female (**b**) body model with the body coil driven in quadrature. The heart and dielectric pads are illustrated in white.

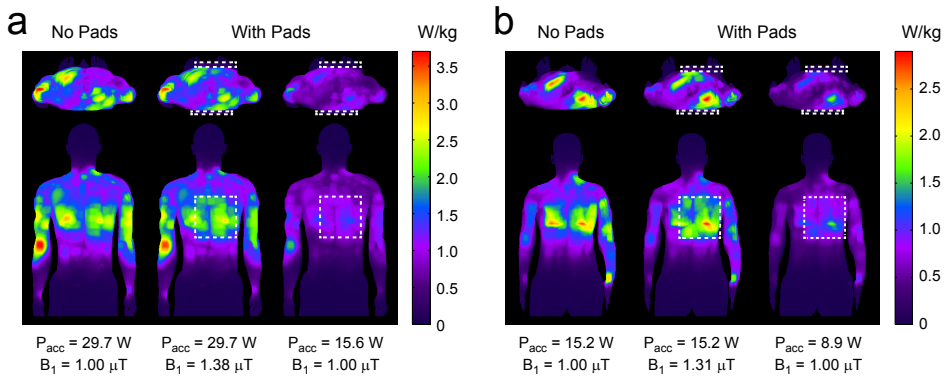

Figure 3.3: Maximum intensity projections of the local SAR in the transverse (top) and coronal (bottom) plane with and without dielectric pads (white), both normalized to the accepted power (P_{acc}; middle) or normalized to the average B_1^+ in the heart ROI (right) for the quadrature driven body coil. The middle figures show that the dielectric pads do not introduce any additional RF hot spots for a given amount of accepted RF power. The right figures show that after proper B_1^+ calibration the SAR is substantially reduced due to the localized increase in transmit efficiency.

Figure 3.2 shows the transverse and sagittal cross sections of the transmit efficiency in the male and female body model corresponding to the configuration with and without dielectric pads. The transmit efficiency maps obtained in the male model were substantially different from those obtained in the female body model which reflects a subject dependence of both the initial B_1^+ distribution and the effect of introducing the dielectric pads. These results, however, also indicate that the best size of the pads is not very subject dependent, which is appealing because one set of pads would then be sufficient for subjects with a similar body geometry.

SAR ANALYSIS

Simulations of the SAR distribution showed that the high permittivity pads do not introduce any RF hot spots. Figure 3.3 shows the maximum intensity projections of the local SAR distribution in the transverse and coronal view for the male and female body model with and without pads, normalized to either the accepted power (P_{acc}; middle) or normalized to the average B_1^+ in the heart ROI (right). The middle figures show that the dielectric pads do not introduce any additional RF hot spots for a given amount of accepted power. The right figures show that after proper B_1^+ calibration the SAR is substantially reduced which is a result of the local increase in transmit efficiency caused by the pads. The relative power balance in the system is presented in Table 3.1 in percentage of accepted power. The peak values of the local SAR for the torso (including the armpits) and extremities obtained in both models are listed in Table 3.2, together with the local torso to global SAR ratio. The relative power balance is normalized to the accepted power and the peak local SAR data are normalized to an average B_1^+ of 1 μT in the heart ROI. From the relative power balance, it is clear that the dielectric pads do not significantly change the distribution of losses in the system. We note that these results are only strictly valid for the quadrature-driven birdcage.

Table 3.1: Relative Power Balance Simulated in the Quadrature Body Coil

	Duke		Ella	
	No Pads	With Pads	No Pads	With Pads
Accepted power (%)	100.00	100.00	100.00	100.00
Tissue dissipated power (%)	85.75	85.22	80.26	79.87
Coil losses (%)	12.08	10.99	15.81	13.59
Pads dissipated power (%)	0.00	2.08	0.00	4.08
Radiated power (%)	2.17	1.71	3.93	2.46

[a] The power balance is normalized to the accepted power.

Table 3.2: SAR Data Simulated in the Quadrature Body Coil

	Duke		Ella	
	No Pads	With Pads	No Pads	With Pads
Global SAR (W/kg)	0.35	0.19	0.20	0.12
Peak local torso SAR (W/kg)	3.10	1.57	2.84	1.79
Peak local extr. SAR (W/kg)	3.68	1.95	2.22	1.06
Local/Global SAR ratio	8.9	8.3	14.2	14.9

[a] The SAR data are normalized to an average B_1^+ of 1 µT in the heart ROI.

TRANSMIT EFFICIENCY AND RECEPTION SENSITIVITY MEASUREMENT

Figure 3.4 shows transverse and sagittal cross sections of the transmit efficiency measured in vivo in one male volunteer with the body coil in quadrature and dual-transmit mode, with and without pads. As can be seen from the images, the dielectric pads prove to be much more effective for creating a local increase of the transmit efficiency and for improving the B_1^+ homogeneity when compared to dual-channel RF shimming. The combined approach resulted in a slightly reduced average transmit efficiency but improved B_1^+ homogeneity because the RF shimming routine optimizes for B_1^+ homogeneity primarily.

The reception sensitivity profiles measured in the same volunteer are illustrated in Fig. 3.5. An increase in the reception sensitivity can be observed after introducing the dielectric pads. This corresponds to a stronger coupling of the receive coil to the body, which has been described previously [26].

Receiver noise correlation matrices have been collected in three volunteers and show no systematic increase in correlation when having the dielectric pads in place. This is consistent with earlier findings [8].

QUANTITATIVE ANALYSIS

Figure 3.6 shows a long-axis and short-axis bSSFP image in end-diastolic phase with corresponding line intensity plots for the four transmit configurations. In both the quadrature mode and the dual-transmit mode, shading artifacts and blood-myocardium con-

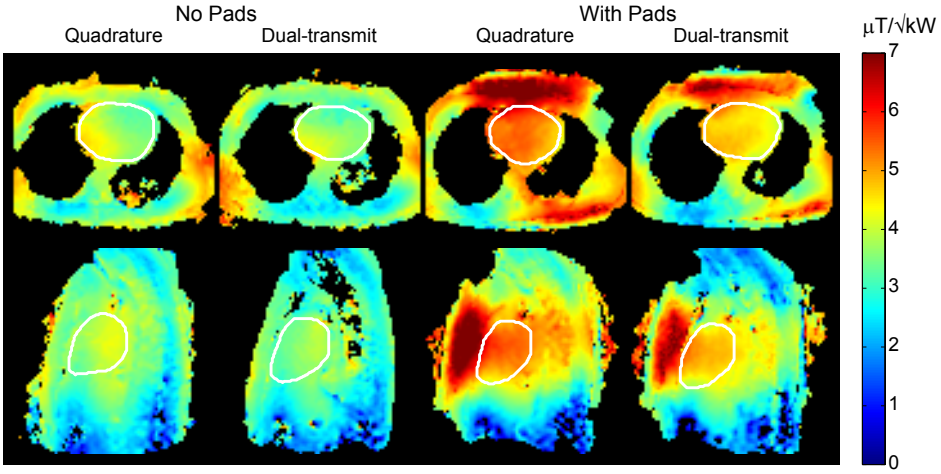

Figure 3.4: Transverse (top) and sagittal (bottom) maps of the transmit efficiency measured in one volunteer with the body coil driven in quadrature and dual-transmit mode, with and without dielectric pads present. The ROI used for evaluating the average transmit efficiency and B_1^+ inhomogeneity is illustrated in white. The dielectric pads show superior improvements in average transmit efficiency and B_1^+ homogeneity compared to dual transmission.

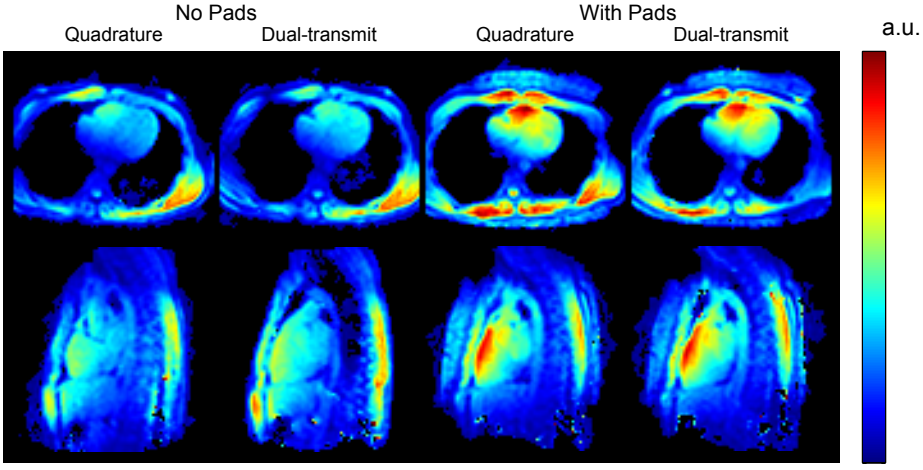

Figure 3.5: Transverse (top) and sagittal (bottom) maps of the reception sensitivity measured in quadrature and dual-transmit mode, with and without dielectric pads. The dielectric pads increased the reception sensitivity in the heart, which corresponds to an increased SNR.

trast variations remain present along the septum toward the apex of the heart. The best image quality is obtained when using the dielectric pads with the body coil driven in dual-transmit mode. For relative comparison, the images were normalized to the mean signal intensity in the aorta.

Measurements of the average transmit efficiency, B_1^+ inhomogeneity, average RF power, and CNR showed a significant improvement when using dielectric pads. The pairwise results are presented in Fig. 3.7. The group mean values and standard deviation are presented in Table 3.3. As can be seen from the data, the dielectric pads lead to a significant improvement in average transmit efficiency and B_1^+ homogeneity both in conventional and dual-channel transmit mode. A cross-comparison considering the configuration with pads in quadrature mode and the configuration without pads in dual-transmit mode indicates that the dielectric pads significantly outperform the dual-transmit system in improving both the average transmit efficiency ($P < 0.0001$) and B_1^+ homogeneity ($P = 0.0002$). Additionally, the dielectric material increased the reception sensitivity and thereby increased the SNR and CNR. It should be noted that the RF power reduction is less then anticipated based on the average transmit efficiency increase due to the use of global B_1^+ calibration, that is, the scanner calibrates the B_1^+ over an entire transverse slice rather than just the ROI of the heart itself [20].

3.4. DISCUSSION AND CONCLUSIONS

High permittivity pads lead to a significant reduction of SAR, improved B_1^+ homogeneity, and increased CNR in functional cardiac MRI. The results presented in this work show that the current approach is more effective than dual-channel RF shimming alone. The most consistent image quality is obtained when both methods are combined.

When comparing dielectric "shimming" to multitransmit RF shimming, it is important to note that the underlying physical mechanisms are fundamentally different. RF shimming using multiple sources is based on the superposition of independent RF fields, the distribution of each being determined by the RF coil, and the dielectric properties of the subject. In contrast, in dielectric shimming, one tailors the intrinsic field distribution of an RF coil which offers degrees of freedom for designing the RF field that are physically different as compared to those offered by multiple coil elements. In a previous 3T application, the dielectric material and geometry were tailored for maximizing global B_1^+ homogeneity across the abdomen [11]. In that case, dielectric pads showed a similar improvement to that obtained using dual-transmission. In the current work, however, we have found that using high permittivity material is much more effective for local RF shimming as compared to dual-transmission, which underlines the different physical mechanisms behind these methods.

A substantial difference can be observed in the improvements in average transmit efficiency and B_1^+ homogeneity caused by the dielectric pads when the body coil is driven in quadrature and dual-transmit mode. This difference can be attributed to the fact that both RF shim strategies introduce some degree of redundancy when they are combined. In other words, when having the dielectric pads in place the starting point for RF shimming is already much closer to the optimum and therefore the potential benefit of using multiple sources is reduced.

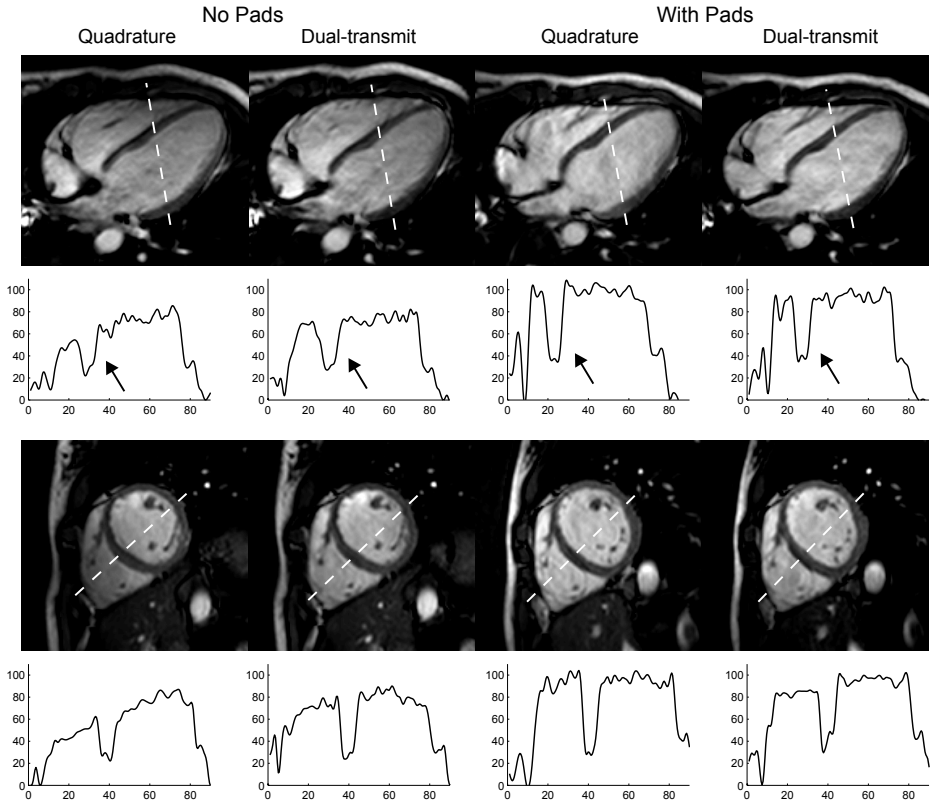

Figure 3.6: Long-axis (top) and short-axis (bottom) bSSFP images in end-diastolic phase for the four configurations with corresponding line intensity profiles. Images obtained without dielectric pads show a substantial signal drop off toward the apex of the heart. Introducing the dielectric pads resolves this artifact and improves the blood-myocardium contrast along the interventricular septum (arrow).

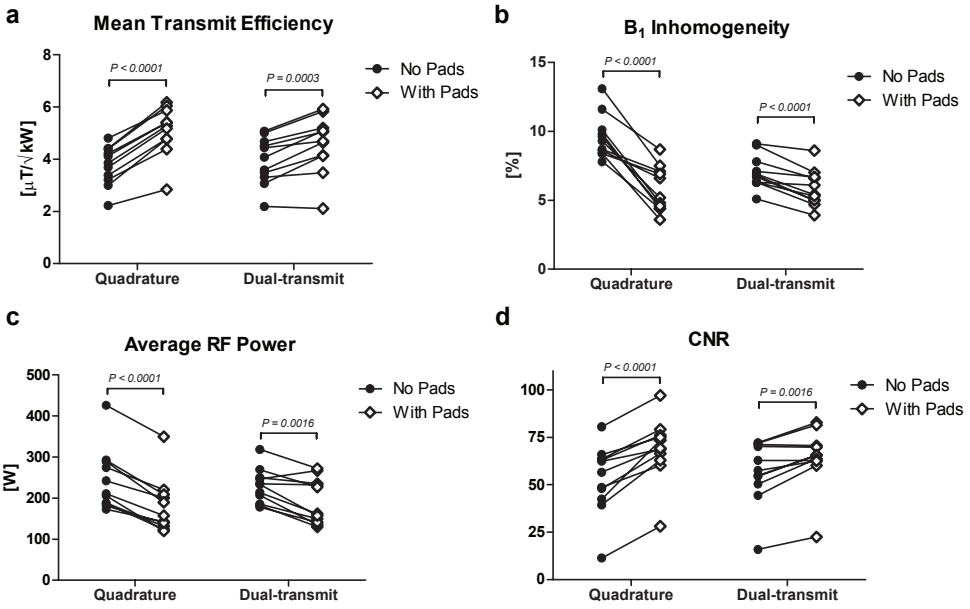

Figure 3.7: Pairwise plots of the average transmit efficiency (**a**), B_1^+ inhomogeneity (**b**), average RF power (**c**), and CNR (**d**) in quadrature and dual-transmit mode, with and without dielectric pads present. The dielectric pads led to significant improvements ($n = 11$).

Due to the increased separation of the receive array and the body, one might suspect that the reception sensitivity drops when the dielectric pads are in place. This would indeed be the case were one to use very low permittivity material, such as foam, as the separator. The high permittivity of the barium titanate suspension, however, increases the coupling of the receiver coil array to the heart which leads to a local increase of the reception sensitivity, which is reflected in the increase in image SNR and CNR.

One very minor drawback of the approach presented in this work is the fact that the subject now has to carry the weight of the anterior pad which amounts to 2.3 kg. The (healthy) volunteers scanned in this study confirmed that the weight is noticeable at first, but easy to accommodate.

In the geometrical design of the dielectric pads, B_1^+ homogeneity was emphasized for reducing subject specificity of the performance. However, one could certainly choose instead to sacrifice some B_1^+ homogeneity for a further reduction in SAR, which would result primarily in increasing the thickness of the anterior pad.

The numerical design study indicated that the anterior dielectric pad is sensitive to placement, which makes sense given the localized nature of the region of interest and the localized increase in B_1^+. In our protocol, we verified the position of the dielectric pads using a 6-s scout scan in the transverse and sagittal planes and corrected the position whenever it was more than approximately 3 cm off. This resulted in a 1-2 min additional time to the imaging protocol. As a future implementation, integration of the dielectric into a vest or into the receiving coil array itself would easily improve the positioning accuracy and reproducibility.

Table 3.3: Group Means in Quadrature and Dual-Transmit Mode, With and Without Dielectric Pads

	Quadrature		Dual-transmit	
	No Pads	With Pads	No Pads	With Pads
Average transmit efficiency ($\mu T/\sqrt{kW}$)	3.8 ± 0.7	5.1 ± 0.9	3.9 ± 0.9	4.6 ± 1.1
B_1^+ inhomogeneity (%)	9.6 ± 1.6	5.8 ± 1.6	7.0 ± 1.2	5.8 ± 1.3
Average RF power (W)	243 ± 75	180 ± 67	229 ± 42	192 ± 55
CNR	52.9 ± 18.2	68.8 ± 16.7	56.9 ± 16.6	64.3 ± 15.8

[a] Values are means ± standard deviations ($n = 11$).

The localized increase of the transmit efficiency caused by the dielectric pads indicates that localized calibration of the RF field within the heart region only is desirable. This has been proposed for cardiac MR at 3T previously, and also implemented in very high-field MRI [4, 27], but is not a standard feature on most commercial systems [20]. When using a conventional calibration routine, one calibrates the mean tip angle over an entire slice, usually in the transverse plane. With the localized increase in the transmit efficiency in the heart afforded by the high permittivity pads, this effectively results in a significantly increased tip angle (compared to the mean tip angle) in the heart, which in turn leads to a suboptimal contrast in the heart and SAR levels that are higher than necessary.

One limiting factor in the current study is that the dielectric pads have been designed for a body coil driven in quadrature mode. The SAR analysis was also limited to the quadrature mode only. The best dielectric configuration and effects on SAR might be slightly different when considering the RF-shimmed body coil system instead. One could think of optimizing both degrees of freedom, that is, RF shims and dielectric pads, simultaneously for increased flexibility in the trade-off between homogeneity and SAR. Furthermore, the numerical design study and SAR analysis were limited to two body models and a different pad geometry might improve the performance in subjects with a very different body geometry. Finally, from an operational point-of-view, it should be noted that some vendors might not include a provision for "external passive devices" such as dielectric pads within their strict legal terms of insurable operation.

ACKNOWLEDGEMENTS

The authors acknowledge Dr. Rob van der Geest, Dr. Jos Westenberg, and Dr. Maarten Versluis for advice on cardiac imaging protocols and image processing schemes. The authors also thank Dr. Alexander Raaijmakers for advice on SAR data representation.

REFERENCES

[1] Gutberlet M, Spors B, Grothoff M, Freyhardt P, Schwinge K, Plotkin M, Amthauer H, Noeske R, and Felix R. Comparison of different cardiac MRI sequences at 1.5 T/3.0 T with respect to signal-to-noise and contrast-to-noise ratios - initial experience.

Rofo 2004; 176:801–808.

[2] Wieben O, Francois C, and Reeder SB. Cardiac MRI of ischemic heart disease at 3 T: potential and challenges. European Journal of Radiology 2008; 65:15–28.

[3] Schar M, Kozerke S, Fischer SE, and Boesiger P. Cardiac SSFP imaging at 3 tesla. Magnetic Resonance in Medicine 2004; 51:799–806.

[4] Schar M, Vonken EJ, and Stuber M. Simultaneous B(0)- and B(1)+-map acquisition for fast localized shim, frequency, and RF power determination in the heart at 3 T. Magnetic Resonance in Medicine 2010; 63:419–426.

[5] Kubach MR, Bornstedt A, Hombach V, Merkle N, Schar M, Spiess J, Nienhaus GU, and Rasche V. Cardiac phase-specific shimming (CPSS) for SSFP MR cine imaging at 3 T. Physics in Medicine and Biology 2009; 54:N467–N478.

[6] Harvey PR, Zhai Z, Morich M, Mens G, van Yperen G, DeMeester G, Graesslin I, and Hoogeveen R. SAR Behavior During Whole-Body MultiTransmit RF Shimming at 3.0T. In: Proceedings of the 17th Annual Meeting of ISMRM, Honolulu, Hawaii, USA, 2009; p. 4786.

[7] Mueller A, Kouwenhoven M, Naehle CP, Gieseke J, Strach K, Willinek WA, Schild HH, and Thomas D. Dual-source radiofrequency transmission with patient-adaptive local radiofrequency shimming for 3.0-T cardiac MR imaging: initial experience. Radiology 2012; 263:77–85.

[8] Teeuwisse WM, Brink WM, and Webb AG. Quantitative assessment of the effects of high-permittivity pads in 7 Tesla MRI of the brain. Magnetic Resonance in Medicine 2012; 67:1285–1293.

[9] Teeuwisse WM, Brink WM, Haines KN, and Webb AG. Simulations of high permittivity materials for 7 T neuroimaging and evaluation of a new barium titanate-based dielectric. Magnetic Resonance in Medicine 2012; 67:912–918.

[10] Yang QX, Wang J, Wang J, Collins CM, Wang C, and Smith MB. Reducing SAR and enhancing cerebral signal-to-noise ratio with high permittivity padding at 3 T. Magnetic Resonance in Medicine 2011; 65:358–362.

[11] de Heer P, Brink WM, Kooij BJ, and Webb AG. Increasing signal homogeneity and image quality in abdominal imaging at 3 T with very high permittivity materials. Magnetic Resonance in Medicine 2012; 68:1317–1324.

[12] Yang QX, Herse Z, Ketterman M, Wang J, Sica C, Collins CM, and Lanagan MT. Enhancement of RF field by high dielectric constant pad at 3T: Cervical Spine Imaging. In: Proceedings of the 19th Annual Meeting of ISMRM, Montreal, Canada, 2011; p. 621.

[13] Snaar JEM, Teeuwisse WM, Versluis MJ, van Buchem MA, Kan HE, Smith NB, and Webb AG. Improvements in high-field localized MRS of the medial temporal lobe in humans using new deformable high-dielectric materials. NMR in Biomedicine 2011; 24:873–879.

[14] van den Berg CAT, van den Bergen B, van de Kamer JB, Raaymakers BW, Kroeze H, Bartels LW, and Lagendijk JJW. Simultaneous B1+ Homogenization and Specific Absorption Rate Hotspot Suppression Using a Magnetic Resonance Phased Array Transmit Coil. Magnetic Resonance in Medicine 2007; 57:577–586.

[15] Vernickel P, Roschmann P, Findeklee C, Ludeke KM, Leussler C, Overwag J, Katscher U, Graesslin I, and Schunemann K. Eight-channel transmit/receive body MRI coil at 3T. Magnetic Resonance in Medicine 2007; 58:381–389.

[16] Homann H, Graesslin I, Eggers H, Nehrke K, Vernickel P, Katscher U, Dössel O, and Börnert P. Local SAR management by RF Shimming: a simulation study with multiple human body models. Magnetic Resonance Materials in Physics Biology and Medicine 2012; 25:193–204.

[17] van den Bergen B, van den Berg CAT, Klomp DWJ, and Lagendijk JJW. SAR and Power Implications of Different RF Shimming Strategies in the Pelvis for 7T MRI. Journal of Magnetic Resonance Imaging 2009; 30:194–202.

[18] Luo W, Lanagan MT, Sica CT, Ryu Y, Oh S, Ketterman M, Yang QX, and Collins CM. Permittivity and performance of dielectric pads with sintered ceramic beads in MRI: early experiments and simulations at 3 T. Magnetic Resonance in Medicine 2013; 70:269–275.

[19] Yang QX, Mao W, Wang J, Smith MB, Lei H, Zhang X, Ugurbil K, and Chen W. Manipulation of image intensity distribution at 7.0 T: passive RF shimming and focusing with dielectric materials. Journal of Magnetic Resonance Imaging 2006; 24:197–202.

[20] El-Sharkawy AMM, Qian D, Bottomley PA, and Edelstein WA. A multichannel, real-time MRI RF power monitor for independent SAR determination. Med Phys 2012; 39:2334–2341.

[21] Christ A, Kainz W, Hahn EG, Honegger K, Zefferer M, Neufeld E, Rascher W, Janka R, Bautz W, Chen J, Kiefer B, Schmitt P, Hollenbach HP, Shen J, Oberle M, Szczerba D, Kam A, Guag JW, and Kuster N. The Virtual Family—development of surface-based anatomical models of two adults and two children for dosimetric simulations. Physics in Medicine and Biology 2010; 55:N23–38.

[22] International Electrotechnical Commission. Particular requirements for the basic safety and essential performance of magnetic resonance equipment for medical diagnosis. IEC 60601-2-33, 3rd ed., Geneva, Switzerland; 2010.

[23] van der Geest RJ, De Roos A, van der Wall EE, and Reiber JHC. Quantitative analysis of cardiovascular MR images. International Journal of Cardiac Imaging 1997; 13:247–258.

[24] Cunningham CH, Pauly JM, and Nayak KS. Saturated double-angle method for rapid B1+ mapping. Magnetic Resonance in Medicine 2006; 55:1326–1333.

[25] Webb AG, and Collins CM. Parallel transmit and receive technology in high-field magnetic resonance neuroimaging. International Journal of Imaging Systems and Technology 2010; 20:2–13.

[26] Liu W, Yang QX, Collins CM, and Smith MB. Numerical Evaluation of Power Radiated by a Loaded Volume Coil at High Fields. In: Proceedings of the 11th Annual Meeting of ISMRM, Toronto, Ontario, Canada, 2003; p. 2393.

[27] Versluis MJ, Kan HE, van Buchem MA, and Webb AG. Improved Signal to Noise in Proton Spectroscopy of the Human Calf Muscle at 7 T Using Localized B1 Calibration. Magnetic Resonance in Medicine 2010; 63:207–211.

Chapter 4

The Effects of High Permittivity Pads on Specific Absorption Rate in Radiofrequency-Shimmed Dual-Transmit Cardiac Imaging at 3 Tesla

J Cardiovasc Magn Reson 2015; 17:82

Wyger M. Brink
Johan S. van den Brink
Andrew G. Webb

ABSTRACT

Background: Dual-channel transmit technology improves the image quality in cardiac imaging at 3T by reducing the degree of radiofrequency (RF) shading over the heart using RF shimming. Further improvements in image quality have been shown on a dual-transmit system using high permittivity pads. The aim of this study is to investigate the transmit field (B_1^+) homogeneity and the specific absorption rate (SAR) characteristics of using high permittivity pads as a function of the complete range of possible RF-shim settings in order to gauge the efficacy and safety of this approach.

Methods: Electromagnetic (EM) simulations were performed in five different body models using a dual-transmit RF coil, with and without high permittivity pads. The RF shimming behaviour in terms of B_1^+ homogeneity and local SAR were determined as a function of different RF-shim settings. Comparative experimental data were obtained in healthy volunteers ($n = 33$) on either a standard-bore (60 cm diameter) or wide-bore (70 cm diameter) 3T MRI system.

Results: EM simulations and experimental data showed higher (B_1^+) homogeneity and lower SAR for optimized RF-shim settings when using the high permittivity pads. The power distribution between the two channels was also much closer to equal using the pads. EM simulations showed that for all five body models studied, optimized RF-shim settings corresponded to reduced local SAR using high permittivity pads. However, there are specific, non-optimal RF-shim settings for which the actual SAR using the pads would be higher than that calculated by the MR system.

Conclusion: The combination of active (dual transmit) and passive (high permittivity pads) RF shimming shows great promise for increasing image quality for cardiac imaging at 3T. In most practical cases optimized RF-shim settings result in increased B_1^+ homogeneity and reduced SAR with the high permittivity pads: however, there are cases in which SAR might be underestimated and these need further investigation.

4.1. BACKGROUND

A number of advantages of performing cardiovascular MRI at 3T compared to 1.5T have been reported [1], particularly in applications such as myocardial tagging and perfusion [2, 3] as well as whole-heart coronary artery imaging [4]. However, significant challenges remain in performing routine clinical imaging at 3T, especially the reduced radiofrequency (RF) transmit field (B_1^+) homogeneity over the heart at 3T compared to 1.5T: Sung et al. [5] have reported that the magnitude of the B_1^+ field can vary by up to 50% at 3T. The B_1^+ inhomogeneity can produce significant shading artifacts leading to a reduced signal-to-noise ratio (SNR) and contrast over the heart [6]. Other issues at 3T include the increased specific absorption ratio (SAR), which limits the minimum repetition time (TR) that can be used, and increased static field (B_0) inhomogeneity over the heart which, in combination with the higher TR, can introduce significant banding into images acquired with the highly efficient steady-state free precession (SSFP) sequences which are used at 1.5T [7].

Recently, all major MRI manufacturers have introduced dual-channel transmit systems for 3T [8]. Although a single-channel system driven in quadrature, i.e. the two modes of the body coil being driven by equal amplitudes and a fixed 90° phase difference, produces a sufficiently homogeneous B_1^+ field at field strengths up to and including 1.5T, this approach is not optimal at 3T as the reduced RF wavelength, which is approximately 25 cm in tissue at 3T, leads to significant B_1^+ nonuniformities within the human body. An elliptical drive, i.e. using equal amplitudes but a fixed non-90° phase difference between the two ports, improves this situation in abdominal imaging but does not provide optimal settings for cardiac imaging. The dual-channel transmit approach utilizes two dedicated transmit chains, which allows for complete independent control of the amplitudes and phases driving the two ports of the body coil. The process of optimizing image quality by adjusting the relative amplitudes and phases of these two channels is referred to as "RF-shimming". A short calibration scan (typically lasting less than a minute) is performed at the beginning of each examination to map the B_1^+ fields of each of the two channels, and based upon these data the optimal relative amplitudes and phases are calculated. SAR estimates are then obtained from a precalculated SAR database, which includes multiple body models and RF-shim settings. This procedure allows for subject-specific driving conditions that optimize the B_1^+ homogeneity as well as reduce the SAR [9, 10]. A number of studies have shown that the dual-channel approach increases the B_1^+ homogeneity over the heart, improves the contrast-to-noise ratio (CNR) between the basal inter-ventricular septum and blood pool, and also between papillary muscles and/or myocardium and the blood pool, and reduces the signal drop-off in the septum, right ventricle and right ventricular free wall [11–13]. In addition, due to the reduced SAR, the TR can be significantly reduced, which leads to a decrease in banding artifacts from the SSFP sequences. In one particular study on high-dose dobutamine stress (HDDS) at 3T, Strach et al. [14] found significant improvements in image and diagnostic quality using a dual-channel transmit system compared to operating in single-channel mode. In their study 13/13 cases were found to be diagnostic in dual-channel transmit mode, compared to only 5/13 in single-channel transmit mode.

An alternative (but also complementary) approach to improving image quality is the use of high permittivity materials [15]. The underlying physical mechanism is that these

materials support a strong and localized density of electrical displacement currents that are induced by the primary RF field from the body coil. These currents can be thought of as secondary sources which superimpose a secondary RF field onto the primary RF field present without high permittivity pads. Therefore, introducing a high permittivity material will generally lead to a local enhancement of the B_1^+ field, which can be tailored to a specific organ or region-of-interest. Previous results have shown that two high permittivity pads optimized for cardiac imaging can significantly increase the CNR, reduce SAR by as much as 50% and improve B_1^+ homogeneity in functional cardiac magnetic resonance at 3T [16]. However, the latter two characteristics have not explicitly been studied as a function of the RF-shim settings, i.e. the relative phases and amplitudes used during the scan. Since the SAR model used in commercial MRI systems obviously does not account for the presence of high permittivity pads, it is currently unknown if the presence of pads while scanning can lead to actual SAR levels higher than those reported by the system under certain conditions of RF-shimming. The aim of this study is to perform a thorough analysis of the B_1^+ and SAR performance of a 3T dual-channel transmit system as a function of RF-shimming in order to address these questions.

4.2. METHODS

Healthy volunteers were scanned under a protocol approved by the local institutional review board. Signed informed consent was obtained from all volunteers.

4.2.1. ELECTROMAGNETIC SIMULATIONS

The transmit RF field in a two-port high pass birdcage body coil tuned to 128 MHz was simulated using commercially available software (xFDTD, version 7.2, Remcom inc., State College, PA, USA). The dimensions of the coil were 50 × 61 cm (length × diameter), where the shield had a diameter of 67 cm. This corresponds to the body coil on a standard-bore (60 cm diameter) 3T system. An isotropic grid of 2.5 mm^3 was used with mesh refinement up to 1 mm around the dielectric pads. A set of five body models were simulated with a body-mass-index (BMI) ranging from 19.2 to 27.3 kg/m^2. Two body models were obtained from the Virtual Family dataset [17], "Duke" (BMI = 23.1 kg/m^2) and "Ella" (BMI = 22.0 kg/m^2) and three body models from the GSF Family [18], "Golem" (BMI = 22.2 kg/m^2), "Irene" (BMI = 19.2 kg/m^2) and "Donna" (BMI = 27.3 kg/m^2).

The simulated field data were processed to evaluate the RF shimming behaviour in terms of B_1^+ inhomogeneity over the whole heart (expressed as the coefficient-of-variation $CV_{B_1^+}$, the ratio of the standard deviation to mean value), and local torso SAR, defined as the peak 10g-averaged SAR within the torso. These measures were calculated for a range of absolute phase differences (-90° to +270°) and relative power ratios (-20 dB to +20 dB; i.e. amplitude ratios of 0.1 to 10) of the two channels. A Q-matrix formalism was applied to model local SAR during RF shimming [19], and 10-g averaging of the Q-matrices was performed using a FFT-based kernel growing method [20]. All routines were implemented in Matlab (version 2012, Mathworks, Natick, MA). All field data were normalized to the average B_1^+ in the transverse cross-section of the body (i.e. a global rather than local B_1^+ value), which corresponds to the B_1^+ calibration procedure that is performed on the scanner [21].

4.2.2. HIGH PERMITTIVITY PADS

Two high permittivity pads, with a relative permittivity of ~300 and conductivity of ~0.4 S/m, were formed as described previously [16] using a suspension of barium titanate (-325 mesh powder, Alfa Aesar, The Netherlands) in distilled deionized water. The dimensions of the high permittivity pads were 20-by-20 cm, with a thickness of 1.5 cm and 1.0 cm for the anterior and posterior pad, respectively. The pads were positioned centered at the heart. After a fast localizer scan acquired in the transverse as well as the sagittal plane to visualize the position of the pads with respect to the heart, a manual adjustment of their position was performed if their position was off by more than ~3 cm.

4.2.3. MRI PROTOCOL

Experimental data were acquired on two different systems, a "standard bore" 60 cm diameter and a "wide bore" 70 cm diameter, to provide a comprehensive assessment of the performance in a cohort of 11 and 22 healthy volunteers, respectively. The imaging protocol, comprising scout images, RF-shimming on the heart, and cine-acquisitions in short- and long-axis with and without high permittivity pads has been described in a previous publication [16]. The RF-shim settings were recorded for each volunteer both in the short-axis and four-chamber views, meaning that two different settings were collected for each subject. The BMI values for the subjects ranged from 20.1 to 34.9 kg/m^2, and body surface area (BSA) from 1.56 to 2.44 m^2.

4.3. RESULTS

Figure 4.1 shows simulated B_1^+ and SAR maps in two body models in the standard-bore magnet, using the RF-shim settings which optimize the B_1^+ homogeneity within the heart for each case. Results obtained in a model of the body coil used in the wide-bore system essentially show very similar results (data not shown). This figure illustrates the improved B_1^+ homogeneity and the reduced SAR that can be achieved when using the high permittivity pads in combination with optimized RF-shim settings.

Figure 4.2 shows the effect of different RF-shim settings on the inhomogeneity of the B_1^+ field (measured as $\mathrm{CV}_{B_1^+}$) over the heart. Figure 4.2(a) shows that, for the Duke model without pads, the highest B_1^+ homogeneity (white circle) occurs at a phase difference of approximately 45° and a power ratio of approximately 8 dB (i.e. a signal amplitude ratio of 2.5 between the two channels). For these settings the $\mathrm{CV}_{B_1^+}$ is 8.6% compared to 14.4% for when the coil is driven in quadrature (shown as a white plus sign). The isocontour, drawn at the level of B_1^+ homogeneity obtained in quadrature mode, indicates that a large range of RF-shim settings improve the transmit homogeneity compared to quadrature mode. When high permittivity pads are in place, RF-shim settings optimized for B_1^+ homogeneity correspond to a power ratio close to unity, and a phase difference ~90°; i.e. the RF coil being driven in quadrature mode. With these settings, the $\mathrm{CV}_{B_1^+}$ is 5.9%, which reflects a further improvement of the B_1^+ homogeneity due to the pads. The isocontour line in this case indicates a very tight set of RF-shim settings (compared to the much more "diffuse" case without pads) would improve the B_1^+ homogeneity over the quadrature mode. The behavior is very similar for the other body models, as also shown for the Ella model in Fig. 4.2(b), with the relevant numbers reported in Table 4.1.

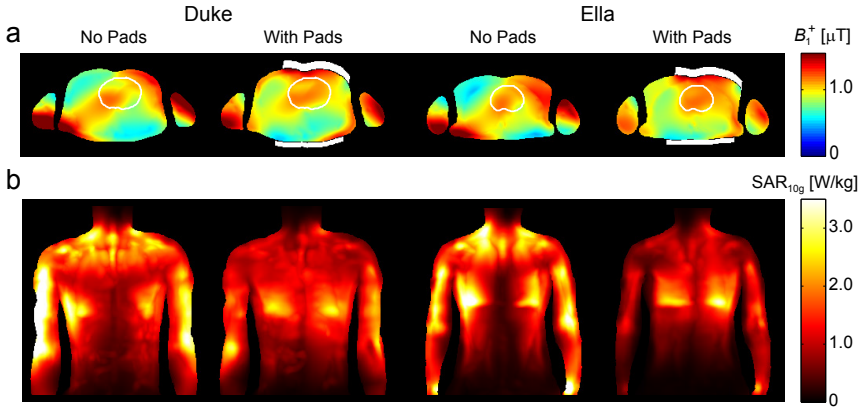

Figure 4.1: Simulations of the RF-shimmed dual-channel transmit system (standard bore) in the body models "Duke" (left), and "Ella" (right) with and without high permittivity pads, shown in white. (**a**) Transverse cross-sections of the B_1^+ and (**b**) coronal maximum intensity projections of the 10g-averaged SAR. The heart is outlined by the thin line. The phase settings are those calculated for maximum B_1^+ homogeneity for each individual case (see Fig. 4.2). The pads improve the B_1^+ homogeneity within the heart and significantly reduce local SAR throughout the body. All data are normalized to a mean B_1^+ of 1 μT in the transverse cross-section of the body model.

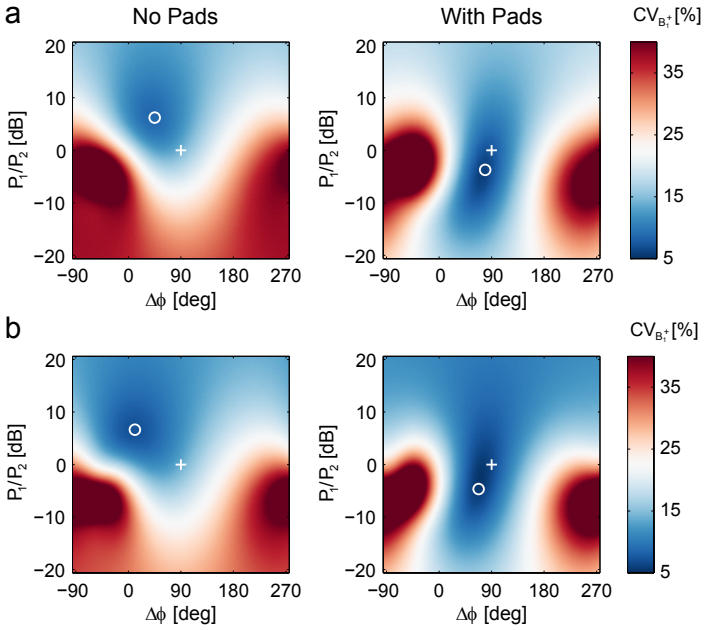

Figure 4.2: Two-dimensional plots of the B_1^+ inhomogeneity (CV$_{B_1^+}$) with RF-shim settings simulated in the body models "Duke" (**a**), and "Ella" (**b**) with and without high permittivity pads. In each plot, quadrature mode is indicated by the plus sign (+) and the RF-shim setting that maximizes B_1^+ homogeneity is indicated by the circle (○). The dashed line indicates the iso-contour at the level of B_1^+ homogeneity obtained in quadrature mode.

Table 4.1: Overview of simulated B_1^+ inhomogeneity for different RF shim settings.

	Duke		Ella		Golem		Irene		Donna	
RF Shim	No Pads	With Pads	No Pads	With Pads	No Pads	With Pads	No Pads	With Pads	No Pads	With Pads
Quadrature	14.4%	7.4%	13.8%	6.4%	10.7%	8.5%	11.5%	8.1%	15.0%	8.0%
Minimum $CV_{B_1^+}$	8.6%	5.9%	7.1%	5.4%	8.2%	7.9%	6.8%	7.3%	7.5%	6.4%
Minimum local SAR	14.2%	7.9%	11.5%	7.8%	11.0%	9.1%	10.1%	9.6%	11.9%	6.4%

Table 4.2: Overview of simulated local torso SAR for different RF shim settings.

	Duke		Ella		Golem		Irene		Donna	
RF Shim	No Pads	With Pads	No Pads	With Pads	No Pads	With Pads	No Pads	With Pads	No Pads	With Pads
Quadrature	3.0	2.1	3.2	2.8	2.8	2.5	3.3	2.9	2.9	2.4
Minimum $CV_{B_1^+}$	5.3	2.8	4.1	3.4	3.9	3.0	4.1	3.5	7.0	1.8
Minimum local SAR	2.5	1.9	1.8	1.8	2.0	1.9	2.0	2.0	1.9	1.7

[a] The SAR data are normalized to an average B_1^+ of 1 µT.

Experimental measurements of the RF-shim settings determined by the system to optimize the B_1^+ homogeneity over the heart are shown in Fig. 4.3, which plots the relative power ratios and phase differences measured on both the standard-bore and wide-bore systems. Confidence ellipses are shown at a level of 95%. Although there is significant variation between individual subjects, a large imbalance in the power delivered to the two channels is clear when no pads are used, whereas the optimal RF-shim when the high permittivity pads are used is close to the quadrature case.

Figure 4.4 shows the variation of local torso SAR in two selected body models as a function of RF-shim setting. In the case of the Duke model without the pads, the lowest SAR value of 2.5 W/kg is found at about a 5 dB power ratio and a 110° phase difference. However, when using these RF-shim settings the $CV_{B_1^+}$ is 14.2%, essentially the same as in the quadrature case. When the pads are added, the lowest SAR value is reduced to 1.9 W/kg, and the corresponding $CV_{B_1^+}$ using these RF-shim settings is 7.9%. These values, and those obtained using the other body models are shown in Tables 4.1 and 4.2.

The results in Fig. 4.5 address the question of to what extent high permittivity pads change the SAR behavior during RF shimming, given that the SAR values reported on the scanner are calculated based on models that do not incorporate high permittivity pads. For example, from Tables 1 and 2, if the system operates in quadrature mode with pads present, the SAR for the Duke model without pads would be 3.0 W/kg, whereas the actual SAR is 2.1 W/kg. So, the reported value would be an overestimation of ~30% and there would be no safety concerns operating in this mode: similarly for the other models. Then, if in the case of the Duke model RF shimming were performed to maximize the B_1^+ homogeneity, then the reported SAR value would be 3.8 W/kg, whereas the actual value is 2.8 W/kg; which reflects again an overestimation of ~25%. However, there are also RF-shim settings for which the reported value is less than the actual value, although these correspond to RF-shim settings which are sub-optimal in terms of either B_1^+ homogeneity or SAR. Figure 4.5 shows the degree to which SAR is over- or underestimated as a function of RF settings for all five different body models, with a wide range of BMI values, heights and weights. In all cases quadrature operation results in a conservative SAR estimate when based on the situation without pads. In four of the five cases, the RF-shim settings which correspond to the highest B_1^+ homogeneity correspond to points very far removed from the areas in which SAR would be underestimated (shown in red). In the case of Donna, which has the highest BMI of 27.3 kg/m^2, optimal RF shimming still results in a lowered SAR compared to that reported, but there is quite a sharp transition to a set of RF shims which would underestimate the SAR.

4.4. DISCUSSION

The results of this study show that, when combining high permittivity pads and dual-channel RF shimming, then in general not only is the B_1^+ uniformity over the heart increased, but also the local SAR is reduced. An important observation of the simulated and experimental data is that the optimal RF-shim settings, in terms of minimizing B_1^+ inhomogeneity or SAR, are much closer to quadrature settings when high permittivity pads are used. This has several advantages: one is the much more equal amounts of power required by both channels, meaning that the upper power limit of the RF amplifier is not reached as quickly as in the case of the much greater degree of power imbalance

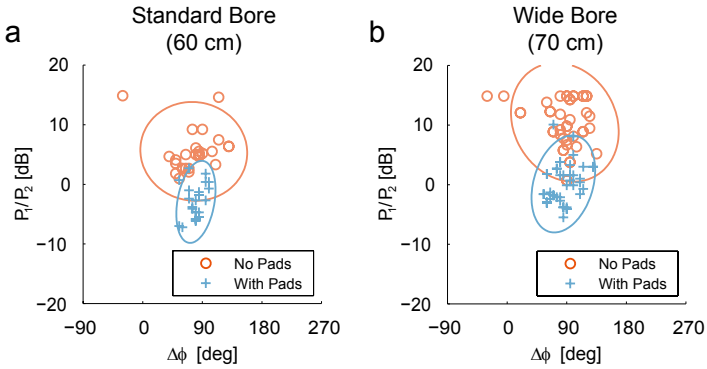

Figure 4.3: Experimental RF shimming results acquired on the standard bore (**a**) and wide bore (**b**) system, together with corresponding 95% confidence ellipses. RF-shim settings for images acquired in the long- and short-axis orientations were recorded separately.

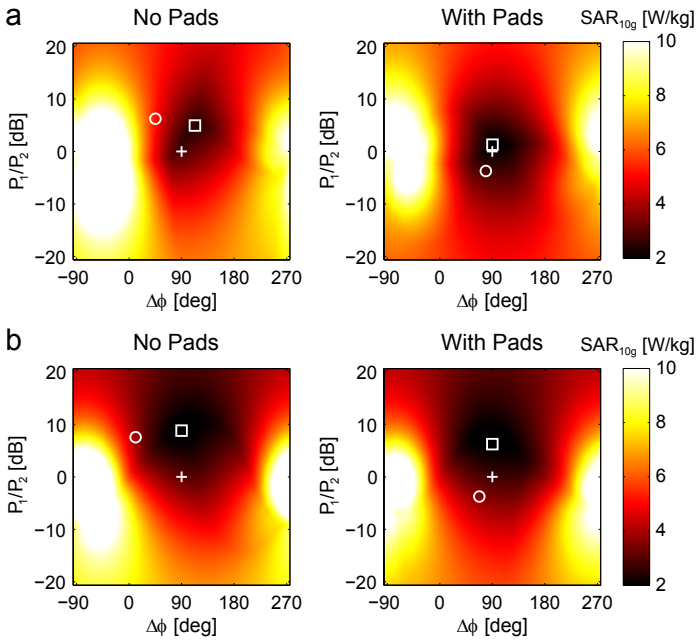

Figure 4.4: Variation of local torso SAR with RF-shim settings simulated in the "Duke" (**a**) and "Ella" (**b**) body models, with and without high permittivity pads. In each plot, quadrature mode is indicated with the plus sign (+) and the shim setting which minimizes local torso SAR by the box (□). For reference, the shim setting that maximizes B_1^+ homogeneity is indicated by the circle (○), as previously shown in Fig. 4.2. All data are normalized to the mean B_1^+ in the transverse cross-section of the body.

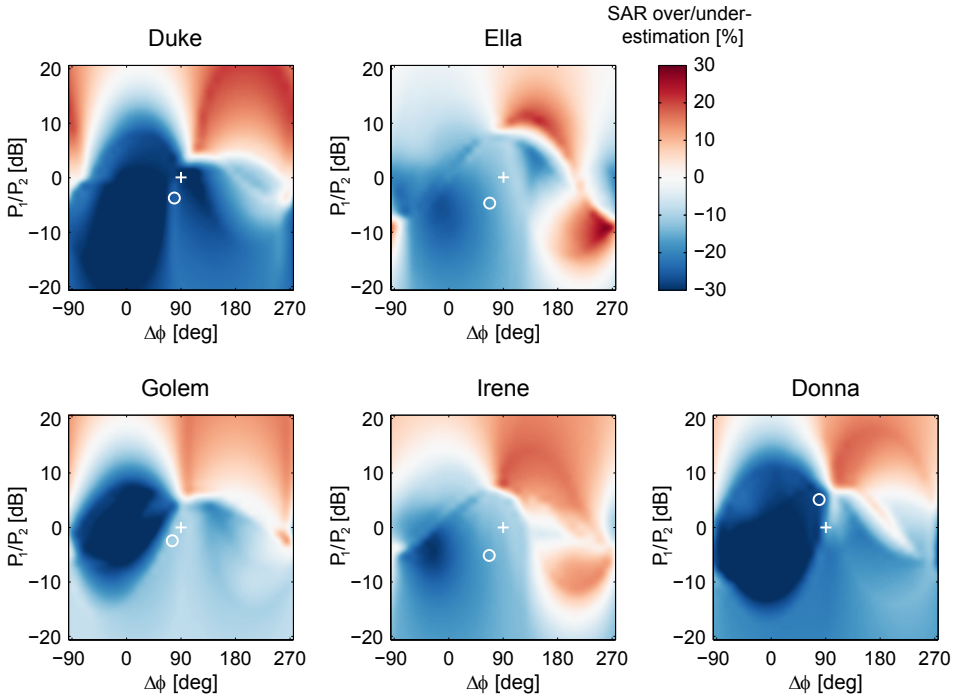

Figure 4.5: Plots of the over- or underestimation of SAR when using high permittivity pads. Blue refers to overestimation, i.e. the actual SAR is less than that calculated by the MRI system. Quadrature mode is indicated with the plus sign (+) and the RF-shim setting that maximizes B_1^+ homogeneity is indicated by the circle (○).

when high permittivity pads are not used. A second is that the process of optimization of the RF-shim values is a much more well-defined problem than without the pads: as shown in Fig. 4.2 the optimum value with pads lies very close to the starting point (which is typically quadrature) and the region of the $CV_{B_1^+}$ minimum is much more tightly defined than in the case without pads. The mechanism behind this is that the high permittivity pads can be thought of as making the elliptical subject more circulo-symmetric, which means that each channel of the body coil is equally efficient.

As shown in Fig. 4.5, for five different body models, the optimization of RF-shim settings either to obtain the lowest $CV_{B_1^+}$ or the lowest SAR, in each case results in an actual SAR with the pads present being lower than that used by the scanner to check the safety of the imaging protocols. However, it is important to note that there are indeed RF-shim settings, indicated in red in Fig. 4.5, which result in the actual SAR being higher than that used by the scanner. In most cases, these RF-shim values are quite distant (e.g. a difference in power distribution of up to a factor-of-five) from ones that would be calculated by the scanner either for minimizing B_1^+ inhomogeneity or SAR, and thus are very unlikely to be chosen. Nevertheless, as shown by the case of Donna, the difference between an overestimation of 10% and an underestimation of 10% can also be relatively small.

One limitation of the current study is the relatively small number of body models studied in the simulations, although we did try to cover as large a range of BMI as is possible using available body models. Experimental data (results not shown) confirmed the work of Krishnamurthy et al. [13] that the relative amplitude and phase settings between the two channels are essentially independent of body habitus. The simulations in Fig. 4.5 show that also the SAR ratio is quite similar for many different types of body size and composition, although for the highest BMI case there were some noticeable differences. The results presented are essentially independent of whether a standard-bore or wide-bore magnet is used: throughout the manuscript simulations have been presented for the standard-bore system, but simulations performed for the wide-bore system show essentially identical behavior (data not shown). Another experimental degree of variability is the potential incorrect positioning of the high permittivity pads on the subjects' body. The high permittivity pads are visible with a very low intensity on the localizer scans and so can be repositioned quickly if required. In simulations (data not shown) the SAR over- or underestimation was essentially identical if the offset in pad position was less than 5 cm.

How might the improved performance be translated to a clinical platform while ensuring patient safety? The most pragmatic solution would be to run the system strictly in quadrature mode when pads are being used, since from Tables 1 and 2 one can see that local SAR is consistently reduced when using the pads in quadrature mode, while B_1^+ homogeneity is typically higher than that of the RF shimmed case without pads. However, this would miss out on the residual reductions in SAR possible by dual channel RF-shimming. A second option would be to introduce an error margin which would reduce the SAR limit when using pads to ~90% of that when not using pads. This would mean that even if the RF shimming algorithm malfunctioned and produced values corresponding to a "red area" in Fig. 4.5, then the chances of underestimating SAR are very low. The ultimate method to take full advantage of the high permittivity pads is, of course, to generate a second SAR model used by the scanner in which a fixed size and position of pads have been included.

4.5. CONCLUSIONS

The combination of active (dual transmit) and passive (high permittivity pads) RF shimming shows great promise for increasing image quality for cardiac imaging at 3T. The current simulation study shows that transmit performance improves when high permittivity pads are used and RF-shim settings are optimized for producing either the highest degree of B_1^+ homogeneity or the lowest SAR. Both of these factors enable higher imaging quality to be achieved for cardiac MR at 3T.

REFERENCES

[1] Oshinski JN, Delfino JG, Sharma P, Gharib AM, and Pettigrew RI. Cardiovascular magnetic resonance at 3.0 T: Current state of the art. Journal of Cardiovascular Magnetic Resonance 2010; 12:55.

[2] Cheng ASH, Pegg TJ, Karamitsos TD, Searle N, Jerosch-Herold M, Choudhury RP, Banning AP, Neubauer S, Robson MD, and Selvanayagam JB. Cardiovascular magnetic resonance perfusion imaging at 3-tesla for the detection of coronary artery disease: a comparison with 1.5-tesla. Journal of the American College of Cardiology 2007; 49:2440–2449.

[3] Thomas D, Strach K, Meyer C, Naehle CP, Schaare S, Wasmann S, Schild HH, and Sommer T. Combined myocardial stress perfusion imaging and myocardial stress tagging for detection of coronary artery disease at 3 Tesla. Journal of Cardiovascular Magnetic Resonance 2008; 10:59.

[4] Gharib AM, Abd-Elmoniem KZ, Herzka DA, Ho VB, Locklin J, Tzatha E, Stuber M, and Pettigrew RI. Optimization of coronary whole-heart MRA free-breathing technique at 3 Tesla. Magnetic Resonance Imaging 2011; 29:1125–30.

[5] Sung K, and Nayak KS. Measurement and Characterization of RF Nonuniformity Over the Heart at 3T Using Body Coil Transmission. Journal of Magnetic Resonance Imaging 2008; 27:643–648.

[6] Greenman RL, Shirosky JE, Mulkern RV, and Rofsky NM. Double Inversion Black-Blood Fast Spin-Echo Imaging of the Human Heart: A Comparison Between 1.5T and 3.0T. Journal of Magnetic Resonance Imaging 2003; 17:648–655.

[7] Barkhausen J, Ruehm SG, Goyen M, Buck T, Laub G, and Debatin JF. MR evaluation of ventricular function: true fast imaging with steady-state precession versus fast low-angle shot cine MR imaging: feasibility study. Radiology 2001; 219:264–269.

[8] Willinek WA, Gieseke J, Kukuk GM, Nelles M, König R, Morakkabati-Spitz N, Träber F, Thomas D, Kuhl CK, and Schild HH. Dual-source parallel radiofrequency excitation body MR imaging compared with standard MR imaging at 3.0 T: initial clinical experience. Radiology 2010; 256:966–975.

[9] van den Berg CAT, van den Bergen B, van de Kamer JB, Raaymakers BW, Kroeze H, Bartels LW, and Lagendijk JJW. Simultaneous B1+ Homogenization and Specific Absorption Rate Hotspot Suppression Using a Magnetic Resonance Phased Array Transmit Coil. Magnetic Resonance in Medicine 2007; 57:577–586.

[10] Katscher U, and Börnert P. Parallel RF transmission in MRI. NMR in Biomedicine 2006; 19:393–400.

[11] Mueller A, Kouwenhoven M, Naehle CP, Gieseke J, Strach K, Willinek WA, Schild HH, and Thomas D. Dual-source radiofrequency transmission with patient-adaptive local radiofrequency shimming for 3.0-T cardiac MR imaging: initial experience. Radiology 2012; 263:77–85.

[12] Jia H, Wang C, Wang G, Qu L, Chen W, Chan Q, and Zhao B. Impact of 3.0 T Cardiac MR Imaging Using Dual-Source Parallel Radiofrequency Transmission with Patient-Adaptive B1 Shimming. PloS one 2013; 8:e66946.

[13] Krishnamurthy R, Pednekar A, Kouwenhoven M, Cheong B, and Muthupillai R. Evaluation of a Subject specific dual-transmit approach for improving B1 field homogeneity in cardiovascular magnetic resonance at 3T. Journal of Cardiovascular Magnetic Resonance 2013; 15:68.

[14] Strach K, Clauberg R, Müller A, Wonneberger U, Naehle CP, Kouwenhoven M, Gieseke J, Schild HH, and Thomas D. Feasibility of high-dose dobutamine stress SSFP Cine MRI at 3 Tesla with patient adaptive local RF Shimming using dual-source RF transmission: initial results. RöFo - Fortschritte auf dem Gebiete der Röntgenstrahlen und der Nuklearmedizin 2013; 185:34–39.

[15] Haines K, Smith NB, and Webb AG. New high dielectric constant materials for tailoring the B1+ distribution at high magnetic fields. Journal of Magnetic Resonance 2010; 203:323–327.

[16] Brink WM, and Webb AG. High permittivity pads reduce specific absorption rate, improve B1 homogeneity, and increase contrast-to-noise ratio for functional cardiac MRI at 3 T. Magnetic Resonance in Medicine 2014; 71:1632–1640.

[17] Christ A, Kainz W, Hahn EG, Honegger K, Zefferer M, Neufeld E, Rascher W, Janka R, Bautz W, Chen J, Kiefer B, Schmitt P, Hollenbach HP, Shen J, Oberle M, Szczerba D, Kam A, Guag JW, and Kuster N. The Virtual Family—development of surface-based anatomical models of two adults and two children for dosimetric simulations. Physics in Medicine and Biology 2010; 55:N23–38.

[18] Petoussi-Henss N, Zanki M, Fill U, and Regulla D. The GSF family of voxel phantoms. Physics in medicine and biology 2002; 47:89–106.

[19] Graesslin I, Homann H, Biederer S, Börnert P, Nehrke K, Vernickel P, Mens G, Harvey P, and Katscher U. A Specific Absorption Rate Prediction Concept for Parallel Transmission MR. Magnetic Resonance in Medicine 2012; 68:1664–1674.

[20] Kuehne A, Seifert F, and Ittermann B. GPU-Accelerated SAR Computation with Arbitrary Averaging Shapes. In: Proceedings of the 20th Annual Meeting of ISMRM, Melbourne, Australia, 2012; p. 2735.

[21] El-Sharkawy AMM, Qian D, Bottomley PA, and Edelstein WA. A multichannel, real-time MRI RF power monitor for independent SAR determination. Med Phys 2012; 39:2334–2341.

Chapter 5

Passive RF Shimming in the Thighs at 3T using High Permittivity Materials and Body Coil Receive Uniformity Correction

submitted

Wyger M. Brink
Hans M. Peeters
Maarten V. Versluis
Peter Börnert
Andrew G. Webb

ABSTRACT

Purpose: To explore the effects of high permittivity dielectric pads on the transmit and receive characteristics of a 3T body coil and their implications on image and contrast uniformity in receive array applications.

Methods: Transmit and receive profiles of the body coil with and without dielectric pads were simulated and measured in healthy volunteers. Parallel imaging was performed in the thighs using sensitivity encoding (SENSE) with and without pads. An intensity correction filter was constructed from the measured receive profile of the body coil.

Results: Measured and simulated data show that the dielectric pads improve the transmit homogeneity of the body coil in the legs, but decrease its receive homogeneity which propagates into a conventional SENSE reconstruction. However, by correcting for the body coil reception profile, contrast uniformity is recovered.

Conclusions: Combining high permittivity dielectric pads with a body coil receive sensitivity filter improves the image quality and contrast uniformity substantially compared to the situation without pads.

5.1. INTRODUCTION

While MRI benefits from higher magnetic field strengths in terms of the signal-to-noise ratio (SNR) and spectral resolution, the increased radiofrequency (RF) transmit field (B_1^+) inhomogeneities pose fundamental challenges. The most commonly-encountered clinical examples occur in the torso at 3T where the RF wavelength approaches the physical dimensions of the body, which gives rise to standing wave patterns with interference effects as described extensively in the literature [1, 2]. These interferences result in spatial variations in the excitation tip angle and lead to corresponding variations in local signal intensity, thereby degrading the contrast uniformity throughout the body. Parallel transmission, using multiple independent transmit channels, has been shown to mitigate this problem for many body applications [3]. This has led to the introduction of dual-channel transmit technology at 3T by most major vendors. However, MRI of the lower pelvis and extremities can still suffer from significant B_1^+ non-uniformity in such a system [4]. These non-uniformities have been reported to be especially problematic in MR angiography in the thighs [5], in which the medial anterior area of reduced transmit efficiency typically coincides with the femoral artery. B_1^+ uniformity in this region can be improved with an increased number of transmit channels: however these eight-channel systems are not yet available for clinical use at 3T [6].

Apart from parallel transmission, dielectric materials can also be used for appropriate RF field shaping. This concept, also referred to as "dielectric shimming", was introduced to MRI by the work of Yang et al. [7] in which the use of water pads was shown to drastically change the MR sensitivity distribution at 7T. This approach was also found to improve the B_1^+ homogeneity at 3T by placing a dielectric pad constructed of water or aqueous gel on top of the abdomen [8–10]. One previous study has evaluated the performance of such a water-based dielectric pad for improving the B_1^+ uniformity in the thighs, but reported inconsistent performance [11]. Recently, dielectric materials with a higher permittivity than water have been shown to significantly improve image quality in angiography of the femoral arteries [12]. These high permittivity dielectric materials are able to induce a much stronger B_1^+ "correction" than can be obtained with water and therefore enable a much more localized increase of the B_1^+ field close to the material [13, 14]. Although initial experiments at our institute confirmed the improved B_1^+ homogeneity when imaging the thighs using these materials, results using a surface coil receive array consistently showed increased image shading in the reconstructed images.

The aim of this current work, therefore, is to explore the consequences of using high permittivity dielectric materials on transmit and receive inhomogeneities and image uniformity in the legs at 3T when using a surface coil receive array, and to evaluate the use of a body coil receive sensitivity filter to improve the reconstructed images.

5.2. THEORY

The B_1^+ field in the legs at 3T features a distinct asymmetric pattern with reduced transmit efficiency at the medial anterior or medial posterior side of the left or right leg, respectively, depending on the subject orientation, i.e. head-first or feet-first, with respect to the static magnetic field. This is schematically illustrated in Fig. 5.1. The receive sensitivity (B_1^-) of the body coil also shows this asymmetric pattern: however, due to the

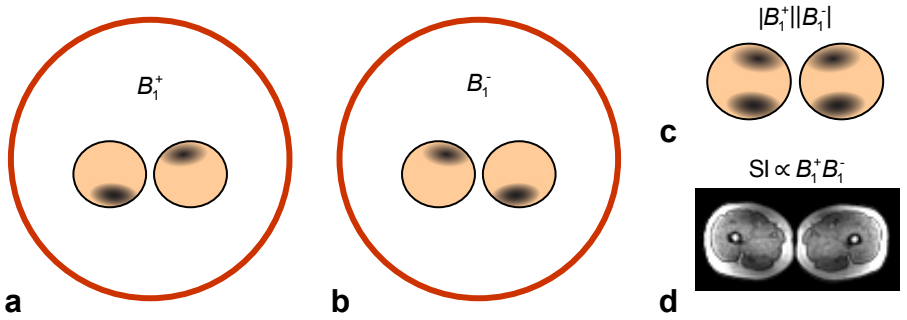

Figure 5.1: Schematic illustration of the transmit (B_1^+) and receive (B_1^-) inhomogeneities of the body coil centered at the legs (transverse view). The B_1^+ profile (**a**) features an asymmetric sensitivity pattern which is mirrored in the B_1^- profile (**b**) for this type of symmetric object. The mirror symmetry leads to complementary shading patterns (**c**) that are visible in a transceive mode image (**d**) obtained using the body coil for both RF transmission and reception in a gradient echo scan performed at 3T.

reverse polarization sensitivity [15], the pattern is mirrored along the symmetry plane of the configuration, as is well known for quadrature coils at high fields [16]. In a transmit-receive (transceive) mode low tip angle gradient echo image acquired using the body coil, this results in complementary areas of shading (c.f. Fig. 5.1(c) and Fig. 5.1(d)).

The use of surface coil arrays for signal reception has become the method of choice on clinical MR systems for their increased SNR with respect to the body coil. This has also led to the development of parallel imaging techniques which offer accelerated imaging by complementing Fourier encoding with spatial encoding via the localized sensitivities of the array elements. Data from non-accelerated acquisitions can be processed using algorithms such as the Roemer reconstruction, whereas accelerated acquisitions (i.e. via undersampling) can be reconstructed using techniques such as sensitivity encoding (SENSE) and generalized autocalibrating partially parallel acquisitions (GRAPPA) [17–19]. As such, the inhomogeneity of the body coil reception profile is not an intrinsic problem. However, most implementations of the Roemer and SENSE reconstruction methods, and some implementations of GRAPPA, use body coil information as a reference for calibration of the receive sensitivity profiles of the array elements, since the body coil is assumed to represent a homogeneous sensitivity reference [18, 20]. In this calibration procedure, the receive coil sensitivity profiles are constructed by acquiring two sets of low-resolution reference images, one using the array elements to receive the signal and the other using the body coil. By dividing the images from the individual array elements by the "uniform" image acquired using the body coil, common factors such as tissue contrast and magnetization phase are removed, thereby providing the magnitude and phase components of the receive coil sensitivity profiles. During this process, systematic errors such as noise and inhomogeneities present in the body coil image can propagate into the coil sensitivity profiles, and from there into the reconstructed image. These coil sensitivity estimation procedures therefore typically incorporate spatial smoothing and other image processing to minimize the effects of noise [18]. Receive inhomogeneities of the body coil, however, are not removed and can still lead to image shading in the reconstructed images, as will be shown in the next section.

A conventional uniform-sensitivity Roemer or SENSE reconstruction p of measured array image data m can be written as [17, 18]

$$p = (\boldsymbol{s}^{\mathrm{H}}\boldsymbol{\Psi}^{-1}\boldsymbol{s})^{-1}\boldsymbol{s}^{\mathrm{H}}\boldsymbol{\Psi}^{-1}\boldsymbol{m} \tag{5.1}$$

in which $\boldsymbol{\Psi}$ denotes the receiver noise correlation matrix and $\boldsymbol{s}$ the receive coil sensitivity vector. These profiles can be obtained from the calibration data vector acquired with the receive array $\boldsymbol{c}$ and the scalar calibration data from body coil b, which contain the same contrast behaviour as $\boldsymbol{c}$, as follows

$$\boldsymbol{s} = \boldsymbol{c}b^{-1}. \tag{5.2}$$

By inserting Equation (5.2) into Equation (5.1), and after some transformations, one can obtain

$$p = b\,(\boldsymbol{c}^{\mathrm{H}}\boldsymbol{\Psi}^{-1}\boldsymbol{c})^{-1}\boldsymbol{c}^{\mathrm{H}}\boldsymbol{\Psi}^{-1}\boldsymbol{m}. \tag{5.3}$$

Equation (5.3) indicates that the uniformity of the final image is defined by b. Therefore, this can serve as a basis for any form of intensity correction necessary in the context of parallel reception [20–22].

A corrected image that compensates for receive inhomogeneities of the body coil can be obtained by correcting the body coil data

$$\hat{b} = \frac{b}{\left|B_1^-\right|} \tag{5.4}$$

or, similarly, by correcting the reconstructed image

$$\hat{p} = \frac{p}{\left|B_1^-\right|}. \tag{5.5}$$

According to Equations 5.4 and 5.5, the correction is independent of the reconstruction technique or acceleration factor used. The correction is referred to as “body coil receive sensitivity filter” in the current work.

5.3. METHODS

HIGH PERMITTIVITY PADS AND ELECTROMAGNETIC SIMULATIONS

Two dielectric pads with a relative permittivity of 300 were designed by means of parametric optimization [13, 14] to improve the B_1^+ homogeneity in the legs. The optimum size of the pads was found to be 13 by 30 cm with a thickness of 1.5 cm. The transmit and receive sensitivities of the body coil were simulated using XFdtd (version 7.3, Remcom Inc., State College, PA). The body coil was modelled, based on the actual body coil geometry, as a 16-rung high-pass birdcage driven in quadrature mode using 50 Ω unit voltage sources at the capacitor gaps. The total length of the birdcage was 50 cm, the rung length was 40 cm and the diameter was 61 cm. The shield had a length of 100 cm and a diameter of 67 cm. For simulating the receive sensitivity the phase evolution along the circumference of the body coil was reversed [16]. The adult male body model “Duke”

from the Virtual Family datasets [23] was used. All simulated data were normalized to 1 kW of dissipated power.

The dielectric pads were constructed using a deuterated suspension of barium titanate with a 4:1 mass-mass ratio [13, 14]. This results in a very dense mixture with a relative permittivity of approximately 300. The pads were positioned asymmetrically on the thighs with one on the medial anterior and one on the medial posterior side, corresponding to the areas of low transmit efficiency.

MR DATA ACQUISITION

Healthy volunteers were scanned under a protocol approved by the local institutional review board. Signed informed consent was obtained from all volunteers. All experiments were performed on a Philips Achieva 3T TX MR system (Philips Healthcare, Best, The Netherlands). In the first part of the protocol the body coil was used in transceive mode. In the second part (corresponding to a practical imaging protocol) a six-channel surface coil array was used for reception, which consisted of three anterior and three posterior elements. The body coil was driven in quadrature mode during all experiments. Two series of scans were acquired, first without and then with dielectric pads in place.

B_1^+ maps were acquired using the dual refocusing echo acquisition mode (DREAM) method [24]. The sequence settings were as follows: field-of-view = 440 × 240 mm^2; in-plane resolution = 5 × 5 mm^2; slice thickness = 10 mm; 27 slices; STEAM/imaging tip angle = 60°/10°; repetition time (TR)/echo time (TE)$_{\text{STE}}$/TE$_{\text{FID}}$ = 3.3/1.9/2.3 ms, acquisition time = 4.5 s. The B_1^+ inhomogeneity was measured via the coefficient of variation (CV), i.e. the standard deviation of the B_1^+ divided by its mean value within the transverse cross-section of the subject. Additional low tip angle three-dimensional (3D) gradient echo images (TR/TE = 3.4/2.3 ms, tip angle = 1°, acquisition time = 7.7 s) were acquired in the same geometry using the body coil in transceive mode. If we omit relaxation effects, the signal intensity (SI) of a low tip angle gradient echo image is given by:

$$SI = M_0 \sin(\gamma B_1^+ \tau) B_1^- \propto B_1^+ B_1^- . \tag{5.6}$$

Therefore, we can obtain an estimate of the receive sensitivity, B_1^-, by taking the ratio of the gradient echo image and the B_1^+ map, using appropriate regularization [25]. Contrast weighting and chemical shift effects were minimized by choosing a short and in-phase TE, a very low tip angle together with appropriate gradient spoiling. The body coil receive sensitivity profile was then used to construct the body coil receive sensitivity filter (cf. Equations 5.4 and 5.5), after smoothing the profile by means of a polynomial fitting procedure to minimize residual density weighting and noise.

Three imaging sequences, which produce image contrasts which are sensitive to B_1^+ variations, were used to visualize the effect of the transmit and receive inhomogeneities when parallel imaging is used, and to evaluate the effectiveness of the body coil receive sensitivity filter. Fast spin echo (FSE) acquisitions were performed as a multi-slice sequence using the following parameters: field of view = 430 × 250 mm^2; in-plane resolution = 1.5 × 1.5 mm^2; slice-thickness = 3 mm; slice-gap = 1.5 mm; 27 slices; TR/TE = 600/10 ms; echo train length = 7; excitation/refocusing tip angle = 90°/180°. Dixon fat/water imaging was performed using a 3D dual-echo gradient echo sequence with the following settings: field of view = 440 × 240 × 200 mm^3; voxel size = 1.4 × 1.4 × 5

mm^3; $TR/TE_1/TE_2$ = 5.3/1.15/2.3 ms; tip angle = 2.5°. A low tip angle was used to enhance the sensitivity to B_1^+ variations. Finally, short inversion time (TI) inversion recovery FSE (STIR-FSE) images were acquired for illustrative purposes using the following protocol parameters: field of view = 440 × 240 mm^2; in-plane resolution = 1.5 × 1.5 mm^2; slice-thickness = 5 mm; slice-gap = 1.5 mm; 31 slices; TR/TE/inversion time (TI) = 5000/25/210 ms; echo train length = 7; excitation/refocusing tip angle = 90°/180°. The TI was designed such that fat signal is reduced in the final images. A non-adiabatic inversion pulse was used to better illustrate the effect of B_1^+ inhomogeneities (in a clinical setting, the use of an adiabatic inversion pulse improves robustness with respect to B_1^+ inhomogeneities). Sensitivity encoding (SENSE) in the A/P direction was used in all parallel reception acquisitions with a SENSE acceleration factor of 1.5, using the body coil as a reference coil during image-based sensitivity estimation [18]. In addition to the conventional SENSE reconstruction, the body coil receive sensitivity filter was applied (cf. Equation (5.5)) in a simple image-processing step to correct the intensity weighting by the body coil reception profile.

5.4. RESULTS

Figures 5.2 and 5.3 show the simulated and measured B_1^+ and B_1^- sensitivity profiles of the body coil with and without dielectric pads. Without dielectric pads, the asymmetric non-uniformity in the B_1^+ profile is pronounced, and mirrored in the B_1^- profile. The use of the dielectric pads leads to a local increase in transmit efficiency which improves the B_1^+ homogeneity, as indicated by the reduced CV values. In particular, the areas of very low transmit efficiency are improved substantially as the pads are positioned close to these areas. This is in contrast to the B_1^- profile, where the local increase in sensitivity is induced in areas where the sensitivity was already high. This degrades the uniformity of the B_1^- profile, which is reflected in the increased CV values. More explicitly, while dielectric pads clearly improved the B_1^+ uniformity, the image shading in a gradient echo image acquired using the body coil appears to be increased (Fig. 5.3(a,b)). This finding can be explained using the principle of reciprocity [15], but may be counterintuitive from an operational point-of-view.

Figure 5.4 show FSE imaging results from one volunteer acquired using the surface coil array, illustrating the effect of the dielectric pads on the contrast uniformity. As the body coil was used as a reference for coil calibration, the final image intensity is modulated by the receive inhomogeneities of the body coil. This can be seen from the conventional SENSE reconstruction without pads, in which both the transmit and receive non-uniformities of the body coil introduce shading in the final image (cf. Figure 5.4(a)). Although using the dielectric pads improves the transmit uniformity of the body coil, as shown in Figs. 5.2 and 5.3, an increased amount of shading can be observed in the reconstructed images, as indicated in Figure 5.4(b). The body coil receive sensitivity filter can correct for these receive non-uniformities, as illustrated in Figure 5.4(c,d). The combined approach of using both the high permittivity pads and the body coil receive sensitivity filter improves both areas of shading and improves the image quality compared to the “standard” clinical protocol using a conventional SENSE reconstruction without dielectric pads.

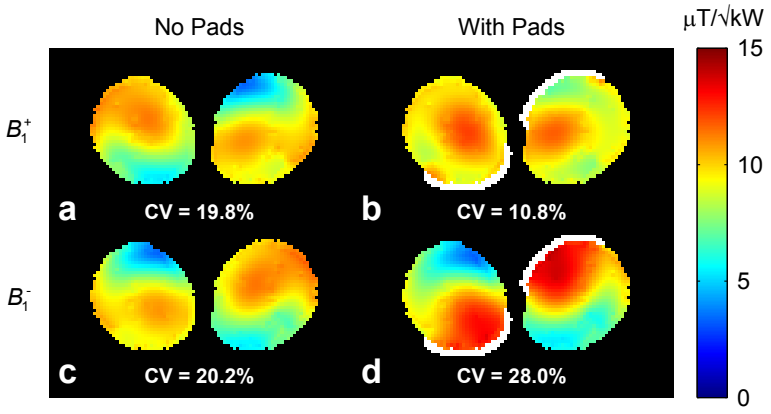

Figure 5.2: Simulated transverse transmit (B_1^+) and receive (B_1^-) sensitivity of the body coil without (left) and with (right) dielectric pads. The homogeneity of the B_1^+ profiles (**a**,**b**) is considerably improved by the dielectric pads while the homogeneity of the B_1^- profiles (**c**,**d**) is degraded, as indicated by the corresponding CV values. The simulated data are normalized to 1 kW of tissue dissipated power. The dielectric pads are shown in white.

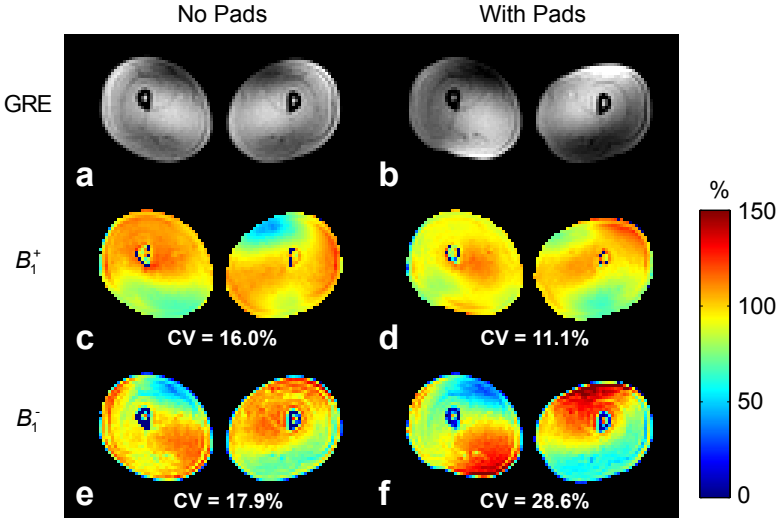

Figure 5.3: Measured transmit (B_1^+) and receive (B_1^-) sensitivity of the body coil without (left) and with (right) dielectric pads. The B_1^+ homogeneity (**c**,**d**) is improved by the dielectric pads while the B_1^- homogeneity (**e**,**f**) is degraded, as indicated by the corresponding CV values. Both factors determine the shading pattern in a low tip angle gradient echo image (GRE) acquired in transceive mode (**a**,**b**). Some residual anatomical structure is visible in the B_1^- maps is due to density weighting.

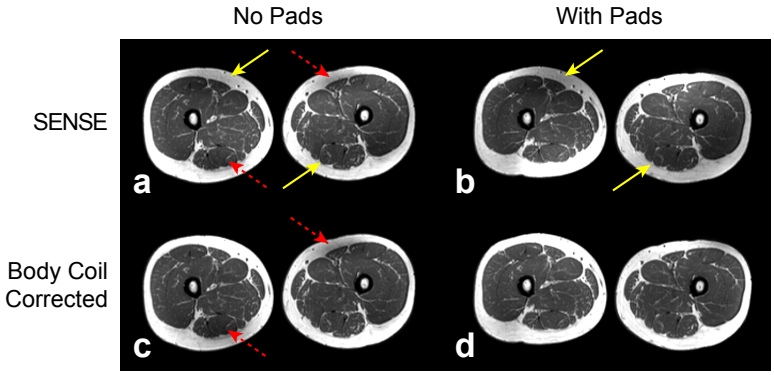

Figure 5.4: FSE imaging results. Shown are the conventional SENSE reconstruction results (**a**,**b**), in which the body coil is used as a reference coil, and the corrected data employing the body coil receive sensitivity filter (**c**,**d**), both without and with dielectric pads. The transmit non-uniformities (**a**,**c**; dashed red arrows) can be corrected using dielectric pads, however the increased receive non-uniformities of the body coil (**a**,**b**; yellow arrows) lead to substantial shading in the final images. This shading can however be removed by the body coil receive sensitivity filter (**d**).

Dixon water images from another volunteer are shown in Fig. 5.5, reflecting the separate areas of transmit and receive non-uniformity and the results of the body coil receive sensitivity filter. Figure 5.5 also shows one-dimensional line profiles through the areas most affected by transmit and receive non-uniformities. Figure 5.5(a) shows the case where a conventional SENSE reconstruction is applied without dielectric pads. There is a clear drop-off in image intensity of 50% with respect to the centre in both the medial posterior and medial anterior sides of the thighs. Figure 5.5(c) shows the same data except corrected using the body coil receive sensitivity filter. In this case the anterior non-uniformity is eliminated, but the posterior shading remains unchanged. In Fig. 5.5(b), in which a conventional SENSE reconstruction is combined with the high permittivity pads, the posterior signal drop-off is corrected, however a 70% drop in signal intensity remains on the anterior side, reflecting the increased receive non-uniformity of the body coil receive profile. Finally, in Fig. 5.5(d) the body coil receive sensitivity correction is combined with the high permittivity pads to produce images in which image uniformity is achieved across the entire profile.

STIR-FSE images are shown in Fig. 5.6. The images without pads clearly show areas of insufficient fat suppression together with a strong signal drop off in the adjacent muscle tissue: both are the result of the low transmit efficiency and thus imperfect inversion in these areas. The receive sensitivity profile of the body coil modulates the reconstructed image intensity to a lesser extent. This can be corrected by applying the body coil receive sensitivity filter. In the STIR-FSE images the effects of transmit and receive non-uniformities are different from a low tip angle gradient echo imaging sequence, such as the DIXON images shown in Fig. 5.5, where the image intensity is approximately linearly proportional to both the transmit and receive non-uniformities. Minor intensity modulation present in Fig. 5.6(d) is due to the remaining B_1^+ non-uniformity of the body coil.

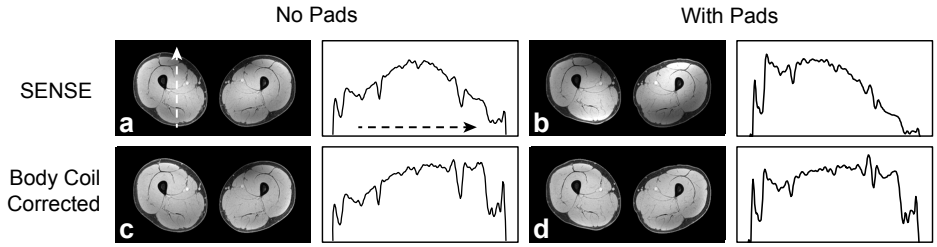

Figure 5.5: Dixon water images using SENSE. Shown are the conventional reconstruction results (**a**,**b**) and those employing the body coil receive sensitivity filter (**c**,**d**), without and with dielectric pads, respectively. Both the transmit and receive non-uniformities of the body coil affect the image uniformity when using conventional SENSE without pads. With dielectric pads and the body coil receive sensitivity filter the areas of shading are largely corrected. Intensity profiles along the dashed line are shown next to each of the images for confirmation.

5.5. DISCUSSION

This study shows that high permittivity pads in combination with a body coil receive sensitivity filter enable homogeneous images to be acquired in the legs at 3T. The particular geometry of the legs represents one of the most challenging applications for achieving uniformity due to their strong asymmetry with respect to the circular symmetry of the body coil, which translates into different regions corresponding to reduced transmit and receive sensitivity, respectively. The high permittivity pads enable localized correction of these B_1^+ non-uniformities from the body coil: however, the B_1^- uniformity of the body coil is decreased as shown both by imaging experiments and electromagnetic simulations. Since surface coil arrays are used for signal reception, and body coil information is incorporated as a reference for coil calibration, this can result in undesired shading in the final image. If not appropriately addressed, this might be ascribed to "negative effects" of the high permittivity materials. This shading can however be overcome by correcting the calibration data before reconstruction, or by correcting the reconstructed images by means of appropriate image-processing using knowledge of the body coil's receive sensitivity as shown in this work. A quantitative B_1^+ map and a simple low tip angle gradient echo were used to estimate the body coil's receive sensitivity profile. With the introduction of very fast volumetric B_1^+ mapping sequences, such as the DREAM method [24], the acquisition of these two additional volumetric datasets requires less than 15 s. The combined approach demonstrates that contrast uniformity using dielectric pads is substantially improved compared to the situation without pads.

It should be noted that, in addition to their effect on the body coil sensitivity profile, dielectric materials also affect the SNR performance of receive array coils, as has been studied extensively by many authors [14, 26, 27]. Similar to the local enhancement of the body coil receptivity, as shown in Figs. 5.2 and 5.3, an increased sensitivity of the receive array is anticipated close to the dielectric material. This may also have some positive implications on the local SNR as well as the geometry factor [18], which improves when the coil sensitivity profiles become significantly different from one another.

The lack of a homogeneous reference at high fields presents a general issue to be con-

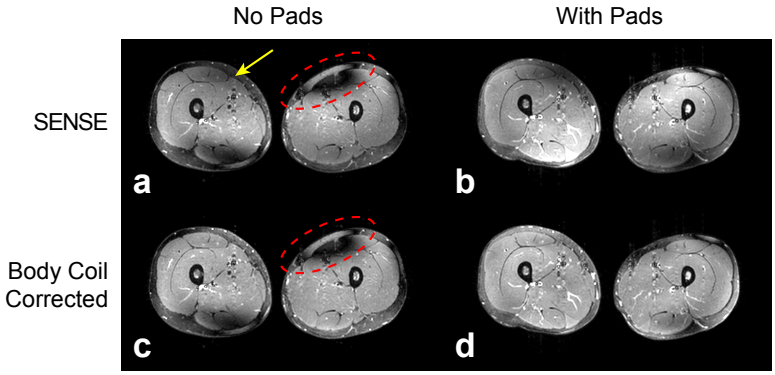

Figure 5.6: STIR-FSE imaging results. (**a**,**b**) show the conventional SENSE reconstructed images whereas (**c**,**d**) show those corrected using the body coil receive sensitivity filter, without and with dielectric pads, respectively. Due to the non-adiabatic inversion pulse, the transmit non-uniformities of the body coil lead to poor fat suppression together with a strong drop-off in local muscle signal (dashed red ellipse), which are improved by using dielectric pads. The receive non-uniformities of the body coil can be corrected using the body coil receive sensitivity filter (**c**,**d**).

sidered during reconstruction and has led to several methods for estimating coil sensitivity profiles. In auto-calibrated approaches such as GRAPPA [19] this problem may not be as severe, since coil sensitivity profiles are not needed for signal unfolding and image combination is typically performed via a sum-of-squares reconstruction. However, in phase-sensitive applications of GRAPPA such as Dixon or phase-contrast imaging, coil sensitivity information is required to preserve the phase of the combined image. Moreover, the intensity of the combined image will be modulated by the sum-of-squares of the coil sensitivity profiles; correction of this term requires knowledge of the coil sensitivity profiles which means that the receive uniformity of the body coil will again define the final image uniformity (cf. Equation (5.3)). Ways to circumvent the need for using the body coil as a reference during receive coil sensitivity estimation include the constructing a body coil surrogate or "virtual" body coil, composed of a weighted combination of the receive array elements [28]. However, the uniformity of the resulting reference coil depends on the geometric arrangement of the receive array elements, and full coverage around the subject is typically not obtained in receive arrays for body imaging. The method presented here is based on combining a low tip angle gradient echo image with a quantitative B_1^+ map to provide an estimate of the B_1^-. Similar methods have been presented in the context of transmit/receive array coil calibration in which B_1^+ and B_1^- maps are derived based on gradient echo images [29, 30]. With a total acquisition time of less than 15 s the current procedure presents only a minor burden to the protocol, which may also prove relevant in other areas regardless of the use of dielectric pads or presence of transmit/receive asymmetry.

Finally, we note that the correction method can be applied independent of the acceleration factor or reconstruction method used. A SENSE accelerated reconstruction has been used here, but similar results would have been obtained when using a non-accelerated Roemer or a uniform-intensity GRAPPA reconstruction.

REFERENCES

[1] Collins CM, Liu W, Schreiber W, Yang QX, and Smith MB. Central brightening due to constructive interference with, without, and despite dielectric resonance. Journal of Magnetic Resonance Imaging 2005; 21:192–196.

[2] Sled JG, and Pike GB. Standing-wave and RF penetration artifacts caused by elliptic geometry: an electrodynamic analysis of MRI. IEEE Transactions on Medical Imaging 1998; 17:653–662.

[3] Willinek WA, Gieseke J, Kukuk GM, Nelles M, König R, Morakkabati-Spitz N, Träber F, Thomas D, Kuhl CK, and Schild HH. Dual-source parallel radiofrequency excitation body MR imaging compared with standard MR imaging at 3.0 T: initial clinical experience. Radiology 2010; 256:966–975.

[4] Hooijmans MT, Dzyubachyk O, Nehrke K, Koken P, Versluis MJ, Kan HE, and Börnert P. Fast multistation water/fat imaging at 3T using DREAM-based RF shimming. Journal of Magnetic Resonance Imaging 2015; 42:217–223.

[5] Nael K, Krishnam M, Nael A, Ton A, Ruehm SG, and Finn JP. Peripheral contrast-enhanced MR angiography at 3.0T, improved spatial resolution and low dose contrast: initial clinical experience. European Radiology 2008; 18:2893–2900.

[6] Childs AS, Malik SJ, O'Regan DP, and Hajnal JV. Impact of number of channels on RF shimming at 3T. Magma 2013; 26:401–410.

[7] Yang QX, Mao W, Wang J, Smith MB, Lei H, Zhang X, Ugurbil K, and Chen W. Manipulation of image intensity distribution at 7.0 T: passive RF shimming and focusing with dielectric materials. Journal of Magnetic Resonance Imaging 2006; 24:197–202.

[8] Sreenivas M, Lowry M, Gibbs P, Pickles M, and Turnbull LW. A simple solution for reducing artefacts due to conductive and dielectric effects in clinical magnetic resonance imaging at 3 T. European Journal of Radiology 2007; 62:143–146.

[9] Franklin KM, Dale BM, and Merkle EM. Improvement in B1-inhomogeneity artifacts in the abdomen at 3T MR imaging using a radiofrequency cushion. Journal of Magnetic Resonance Imaging 2008; 27:1443–1447.

[10] Kataoka M, Isoda H, Maetani Y, Nakamoto Y, Koyama T, Umeoka S, Tamai K, Kido A, Morisawa N, Saga T, and Togashi K. MR imaging of the female pelvis at 3 Tesla: evaluation of image homogeneity using different dielectric pads. Journal of Magnetic Resonance Imaging 2007; 26:1572–1577.

[11] Storey P, Lee VS, Sodickson DK, Santoro D, Zhang B, Lim RP, Atanasova IP, Stoffel DR, Chen Q, and Wiggins GC. B1 inhomogeneity in the thigh at 3T and implications for peripheral vascular imaging. In: Proceedings of the 17th Annual Meeting of ISMRM, Honolulu, Hawaii, USA, Honolulu, 2009; p. 426.

[12] Lindley MD, Kim D, Morrell G, Heilbrun ME, Storey P, Hanrahan CJ, and Lee VS. High-permittivity thin dielectric padding improves fresh blood imaging of femoral arteries at 3 T. Investigative Radiology 2015; 50:101–107.

[13] de Heer P, Brink WM, Kooij BJ, and Webb AG. Increasing signal homogeneity and image quality in abdominal imaging at 3 T with very high permittivity materials. Magnetic Resonance in Medicine 2012; 68:1317–1324.

[14] Brink WM, and Webb AG. High permittivity pads reduce specific absorption rate, improve B1 homogeneity, and increase contrast-to-noise ratio for functional cardiac MRI at 3 T. Magnetic Resonance in Medicine 2014; 71:1632–1640.

[15] Hoult DI. Sensitivity and Power Deposition in a High-Field Imaging Experiment. Journal of Magnetic Resonance Imaging 2000; 12:46–67.

[16] Wang J, Yang QX, Zhang X, Collins CM, Smith MB, Zhu XH, Adriany G, Ugurbil K, and Chen W. Polarization of the RF field in a human head at high field: a study with a quadrature surface coil at 7.0 T. Magnetic Resonance in Medicine 2002; 48:362–369.

[17] Roemer PB, Edelstein WA, Hayes CE, Souza SP, and Mueller OM. The NMR phased array. Magnetic Resonance in Medicine 1990; 16:192–225.

[18] Pruessmann KP, Weiger M, Scheidegger MB, and Boesiger P. SENSE: sensitivity encoding for fast MRI. Magnetic Resonance in Medicine 1999; 42:952–962.

[19] Griswold MA, Jakob PM, Heidemann RM, Nittka M, Jellus V, Wang J, Kiefer B, and Haase A. Generalized autocalibrating partially parallel acquisitions (GRAPPA). Magnetic Resonance in Medicine 2002; 47:1202–1210.

[20] Murakami JW, Hayes CE, and Weinberger E. Intensity correction of phased-array surface coil images. Magnetic Resonance in Medicine 1996; 35:585–590.

[21] Fuderer M, and van Heelsbergen TR. Magnetic resonance imaging method and apparatus. US Patent 5587656. 2002.

[22] Mauconduit F, Massire A, Boulant N, Amadon A, and Vignaud A. Reception Sensitivity Inhomogeneity Correction at Ultra High Field using a Fast Gradient Echo Sequence. In: Proceedings of the 22nd Annual Meeting of ISMRM, Milan, Italy, Milan, 2014; p. 1642.

[23] Christ A, Kainz W, Hahn EG, Honegger K, Zefferer M, Neufeld E, Rascher W, Janka R, Bautz W, Chen J, Kiefer B, Schmitt P, Hollenbach HP, Shen J, Oberle M, Szczerba D, Kam A, Guag JW, and Kuster N. The Virtual Family—development of surface-based anatomical models of two adults and two children for dosimetric simulations. Physics in Medicine and Biology 2010; 55:N23–38.

[24] Nehrke K, and Börnert P. DREAM—A Novel Approach for Robust, Ultrafast, Multi-slice B1 Mapping. Magnetic Resonance in Medicine 2012; 68:1517–1526.

[25] Wang J, Qiu M, Yang QX, Smith MB, and Constable RT. Measurement and correction of transmitter and receiver induced nonuniformities in vivo. Magnetic Resonance in Medicine 2005; 53:408–417.

[26] Yang QX, Rupprecht S, Luo W, Sica C, Herse Z, Wang J, Cao Z, Vesek J, Lanagan MT, Carluccio G, Ryu YC, and Collins CM. Radiofrequency field enhancement with high dielectric constant (HDC) pads in a receive array coil at 3.0T. Journal of Magnetic Resonance Imaging 2013; 38:435–440.

[27] Teeuwisse WM, Brink WM, and Webb AG. Quantitative assessment of the effects of high-permittivity pads in 7 Tesla MRI of the brain. Magnetic Resonance in Medicine 2012; 67:1285–1293.

[28] Buehrer M, Boesiger P, and Kozerke S. Virtual Body Coil Calibration for Phased-Array Imaging. In: Proceedings of the 17th Annual Meeting of ISMRM, Honolulu, Hawaii, USA, Honolulu, 2009; p. 760.

[29] Van de Moortele PF, Akgun C, Adriany G, Moeller S, Ritter J, Collins CM, Smith MB, Vaughan JT, and Uğurbil K. B1 destructive interferences and spatial phase patterns at 7 T with a head transceiver array coil. Magnetic Resonance in Medicine 2005; 54:1503–1518.

[30] Sbrizzi A, Raaijmakers AJE, Hoogduin H, Lagendijk JJW, Luijten PR, and van den Berg CAT. Transmit and receive RF fields determination from a single low-tip-angle gradient-echo scan by scaling of SVD data. Magnetic Resonance in Medicine 2014; 72:248–259.

Chapter 6

High Permittivity Dielectric Pads Improve High Spatial Resolution Magnetic Resonance Imaging of the Inner Ear at 7T

Invest Radiol 2014;49:271–277

Wyger M. Brink
Annerie M.A. van der Jagt
Maarten J. Versluis
Berit M. Verbist
Andrew G. Webb

ABSTRACT

Objectives: The objective of this study was to evaluate the use of dielectric pads for improving high spatial resolution imaging of the inner ear at 7T.

Materials and Methods: Two sets of dielectric pads were designed using electromagnetic simulations and implemented using a deuterated suspension of barium titanate. Their effect on transmit efficiency, contrast homogeneity, and diagnostic image quality was evaluated in vivo ($n = 10$). In addition, their effect on the specific absorption rate was evaluated numerically.

Results: Statistically significant improvements ($P < 0.001$) in several measures of the image quality were obtained by using dielectric pads. The dielectric pads lead to an increase in the transmit efficiency and uniformity at the location of the inner ear, which is reflected in both an increased contrast homogeneity and an increased diagnostic value. Simulations show that the dielectric pads do not increase the peak local specific absorption rate.

Conclusion: Using geometrically tailored dielectric pads enables high spatial resolution magnetic resonance imaging of the human inner ear at 7T. The high spatial resolution improves the depiction of the fine inner ear structures, showing the benefit of magnetic resonance imaging at ultrahigh fields.

6.1. INTRODUCTION

Visualization of the fine structures of the inner ear by magnetic resonance imaging (MRI) is of great importance when evaluating patients with sensorineural hearing loss or deafness, vertigo, and tinnitus to identify infectious, inflammatory, and neoplastic disease or congenital malformations [1–5]. Furthermore, there is an increasing interest in anatomical information and normative measures of the inner ear microstructures and the cochlear nerve regarding cochlear implantation. Feasibility of implantation, development of electrodes, and adjustments in operation technique may be guided by these, particularly in cochlear implant surgery with residual hearing preservation (e.g., electroacoustic stimulation) [6–11].

The value of heavily T_2-weighted magnetic resonance (MR) images for the depiction of the inner ear and internal auditory canal has been recognized since the 1990s when three-dimensional (3D) sequences based on fast spin echo (FSE) or balanced steady-state free precession were introduced. Reported advantages of the FSE technique were reduction of susceptibility artifacts, shorter acquisition time, and maintenance of true T_2 contrast rather than T_2^* contrast of gradient echo sequences [12, 13]. This imaging technique was particularly focused on the visualization of vestibular schwannomas but also provided a good depiction of the inner ear structures. Further improvement of spatial resolution may render a better depiction of the labyrinthine microstructures, particularly in the apex of the cochlea, but attempts to image organs of the membranous labyrinth have been compromised by stop-band artifacts in the case of balanced steadystate free precession sequences and image blurring inherent to FSE sequences [14].

The increased intrinsic signal-to-noise ratio (SNR) afforded by 7T MRI offers an opportunity for improving the depiction of the detailed structures of the inner ear. However, imaging the inner ear at 7T is challenging because of strong inhomogeneities in both the static (B_0) and the transmit radiofrequency (RF; B_1^+) fields, caused by the susceptibility difference between the inner ear fluids and the surrounding bone as well as the elliptical shape of the head, respectively [15]. The B_1^+ nonuniformities in the brain have been studied extensively in neuroimaging at 7T and typically feature areas of low B_1^+ in the temporal lobes, extending down to the temporal bone. The large local B_0 inhomogeneities close to the inner ear suggest that spin echo sequences should be used because of their immunity to resonance frequency offsets; however, their use is limited by the inhomogeneities in the B_1^+ field.

Dielectric pads have previously been used for B_1^+ shimming at 3 and 7T and show potential for improving the B_1^+ distribution without increasing the specific absorption rate (SAR) [16–25]. Suspended metal titanates such as calcium titanate with a relative permittivity of approximately 110 have been used to improve the homogeneity of the B_1^+ field across the brain at 7T [18, 21]. Materials with a higher permittivity, such as suspensions of barium titanate with a relative permittivity of approximately 300, can be used to reduce the required pad thickness because of their stronger interaction with the RF field [22]. These stronger interactions can also be used to increase the B_1^+ locally, albeit at the cost of global B_1^+ homogeneity, while satisfying the geometrical constraints imposed by the close-fitting receiver arrays. This is the mechanism that we aim to exploit in this study to improve the B_1^+ distribution in the inner ear region of interest.

In this work, two sets of dielectric pads, one for male and one for female subjects, are designed using electromagnetic simulations and constructed using a deuterated suspension of barium titanate. The effect of the dielectric pads on SAR is evaluated numerically and their effect on the B_1^+ distribution and image quality is evaluated in vivo. A qualitative comparison of image quality and diagnostic value was performed by two experienced radiologists.

6.2. MATERIALS AND METHODS

ELECTROMAGNETIC SIMULATIONS

Electromagnetic simulations of the transmit RF field were performed using xFDTD (version 7.2; Remcom, Inc, State College, PA) to determine the best geometry of two dielectric pads placed on either side of the head and to assess the effects of these pads on the 10-g averaged SAR distribution. The transmit coil was modeled as a 16-rung high-pass birdcage driven in its fundamental mode using unit voltage sources with an intrinsic impedance of 50 Ω at the capacitor gaps. The inner diameter of the birdcage was 29.8 cm; each rung was 18.0 cm in length and 2.5 cm in width. The outer diameter of the shield was 35.9 cm and its length was 20.0 cm. The configuration was simulated on a 2.5 mm^3 isotropic grid. Male and female subjects were modeled through "Duke" and "Ella" from the Virtual Family data set, with appropriate tissue parameters assigned to each tissue type [26]. All simulated data were normalized to 1 W of dissipated power in tissue.

The design procedure was set up by defining a baseline geometry for both pads of 10 × 10 cm and 1 cm thickness, centered at the ears. The thickness and dielectric properties of the pads were then kept constant, whereas their width and height were varied between 10 and 20 cm in steps of 2 cm to improve the B_1^+ distribution in the inner ear region of interest. The position was finally varied by introducing a positioning offset of up to 5 cm in steps of 1 cm. For each geometry, the B_1^+ distribution was evaluated through a figure of merit formulated in terms of the transmit uniformity, defined as the standard deviation of the B_1^+ divided by its mean value, and the average transmit efficiency, defined as the mean B_1^+ per square root of dissipated power, similar to methods applied earlier in the design of dielectric pads [22–24]. On the basis of this figure of merit, the best geometry was selected for further implementation and evaluation in vivo.

DIELECTRIC PADS

The dielectric pads were constructed using a suspension of barium titanate (–325 mesh powder, Alfa Aesar GmbH & Co. KG, Karlsruhe, Germany) and deuterated water (99.9%, Sigma Aldrich, Zwijndrecht, The Netherlands). Deuterated water was used to suppress the MR signal coming from the dielectric material. The material was characterized using a dielectric probe kit (85070E; Agilent Technologies, Santa Clara, CA) and features a relative permittivity of 286 and electrical conductivity of 0.44 S/m at 298 MHz, which were applied in the electromagnetic simulation model during the numerical design process and SAR evaluation. The mixture was then sealed in polypropene using a manual sealer (420 SBM-2; Audion Elektro, Weesp, The Netherlands) to form rectangular pads with dimensions outlined later in the article.

MR IMAGING

In vivo experiments were performed on a Philips Achieva 7Tesla system (Philips Healthcare, Best, The Netherlands) using a quadrature transmit/receive birdcage coil (NM008A-7P-012; Nova Medical, Wilmington, MA) and a 32-channel receive array (NMSC075-32-7P; Nova Medical, Wilmington, MA). A series of scans was acquired first with dielectric pads in place and centered on the ears; the pads were then removed, and the entire protocol was repeated for comparison.

Local calibration of the transmit gain was performed by acquiring a whole-head B_1^+ map at a spatial resolution of $2.5 \times 2.5 \times 5$ mm^3 using the dual refocused acquisition mode sequence, which takes only 10 seconds to perform [27, 28]. The absence of MR signal coming from the temporal bone obviously limits the accuracy of the B_1^+ estimate in this region; however, an adequate estimate could be obtained from the surrounding tissue. The B_0 field was shimmed to third order using the vendor-supplied image-based shimming routine.

High spatial resolution T_2-weighted images were acquired both with and without dielectric pads in place using a 3D-FSE sequence with the following sequence parameters: field of view, $180 \times 180 \times 24$ mm^3; 0.3 mm^3 isotropic voxels; tip angle/refocusing angle, 90/135°; time of repetition/time of echo/inter-echo time, 3000/200/12.7 ms, with 69 refocusing RF pulses; parallel imaging in two directions with a reduction factor of 2.5 (left-right) × 1.5 (feet-head), which resulted in an acquisition time of approximately 10 min. Data were acquired in 10 healthy volunteers (5 females, 5 males; mean age, 25 years). The study was approved by the institution's ethics board, and written informed consent was obtained in all volunteers.

QUALITATIVE IMAGE ANALYSIS

The high spatial resolution T_2-weighted images obtained with and without dielectric pads were independently scored twice in randomized order by two experienced clinicians (B.V., with 13 years of experience in imaging the temporal bone, and G.H., with 15 years of experience in MRI). The readers were blinded to the subject's name and the acquisition technique used. The contrast homogeneity of the inner ear system, that is, both the right and left inner ears, was rated on a 3-point scale between 1 and 4 as follows: 4, good contrast homogeneity; 2.5, mild contrast inhomogeneity; 1, strong contrast inhomogeneity. The visibility and diagnostic value of the semicircular canals, cochlea, and internal auditory canal (IAC) were rated for both sides individually on a 4-point scale between 1 and 4 as follows: 4, good depiction, high diagnostic value; 3, acceptable visibility, adequate diagnostic value; 2, poor visibility, inadequate diagnostic value; 1, not visible, nondiagnostic image. We note that both ranges were matched to facilitate data interpretation.

STATISTICAL ANALYSIS

Statistical analyses were performed using Statistical Package for the Social Sciences (version 20; IBM, Amsterdam, The Netherlands). To determine the effect of using the dielectric pads, a group analysis was performed per reader by computing the mean score and standard deviation per criteria on the basis of the pooled scores including both observations made. We note that, strictly speaking, a symmetric normal distribution cannot be

assumed given the limited range of the scores; however, this measure gives a reasonable indication of the effect of using the dielectric pads. The scores were deblinded on the basis of the acquisition technique used before computing the mean and standard deviations. Statistical differences were determined using a Wilcoxon signed rank test. The intrarater agreement was determined using the Fisher intraclass correlation coefficient and the interrater agreement was determined using the κ coefficient of Cohen. All tests were 2-tailed and $P < 0.001$ was considered to indicate a statistically significant difference.

6.3. RESULTS

ELECTROMAGNETIC SIMULATIONS

The design process of the dielectric pads led to two slightly different configurations for the male and female body models. In the female model, the best pad geometry was found to be a 10 × 10 cm pad on the left and a 14 × 14 cm pad on the right side of the head. The male model required a 10 × 10 cm pad on the left and an 18 × 14 cm (width × height) pad on the right side of the head; the difference is caused by the larger male head size. Transverse and coronal cross sections of the resulting simulated transmit efficiency for the four configurations (male/female, with/without pads) are shown in Fig. 6.1. The asymmetric size of the pads is required in both models to correct for the B_1^+ asymmetry at the level of the inner ear when having no pads in place [15]. Simulations of the 10-g averaged SAR distribution show that, for a power normalized case, the local SAR does not increase because of the introduction of the dielectric pads. Maximum intensity projections of the local SAR distribution in the transverse and coronal views are shown in Fig. 6.2.

MR IMAGING

The measured effects of the dielectric pads on the transmit uniformity and efficiency are shown in Fig. 6.3. Transverse maximum intensity projections of the resulting images are shown in Fig. 6.4. It is clear that, without pads, the areas of low B_1^+ overlap almost completely with the inner ear, leading to severe signal dropouts and contrast inhomogeneity. The measured transmit efficiency maps, defined here as B_1^+ over square root of transmitted power, show that the B_1^+ is considerably improved locally by introduction of the dielectric pads, which corresponds to an improved contrast homogeneity throughout the imaging region of interest. We note that the transmitted power includes also power lost in the RF chain, which can be as much as 50% of the total power budget. This introduces an offset between the measured and simulated transmit efficiency maps; because the simulations did not include these losses, however, a relative comparison is still valid.

Remaining small relative differences are most likely caused by differences in the head size and shape of individuals with respect to the model used for the simulations. The left/right asymmetry, which can be observed in the images acquired without pads, is adequately compensated by using a different pad size on either side of the head. Moreover, the images acquired in the male subject reflect the stronger B_1^+ inhomogeneity, which indicates the need for a different pad geometry. It should be noted that the central brightening effect can lead to considerable "overtipping" of the magnetization in the

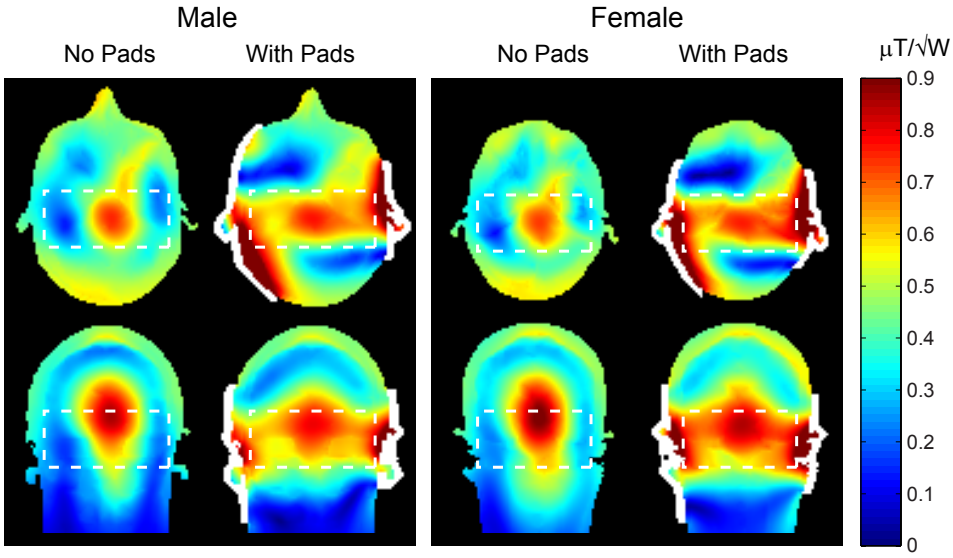

Figure 6.1: Transverse (top) and coronal (bottom) cross sections of the simulated transmit efficiency maps in a male (left) and female (right) body model, without and with dielectric pads. The dielectric pads are illustrated in white and the imaging region of interest of the inner ear is outlined in the dashed box. The maps show the effectiveness of the dielectric pads for locally tailoring the B_1^+ field. The field data are normalized to 1 W of dissipated power in tissue.

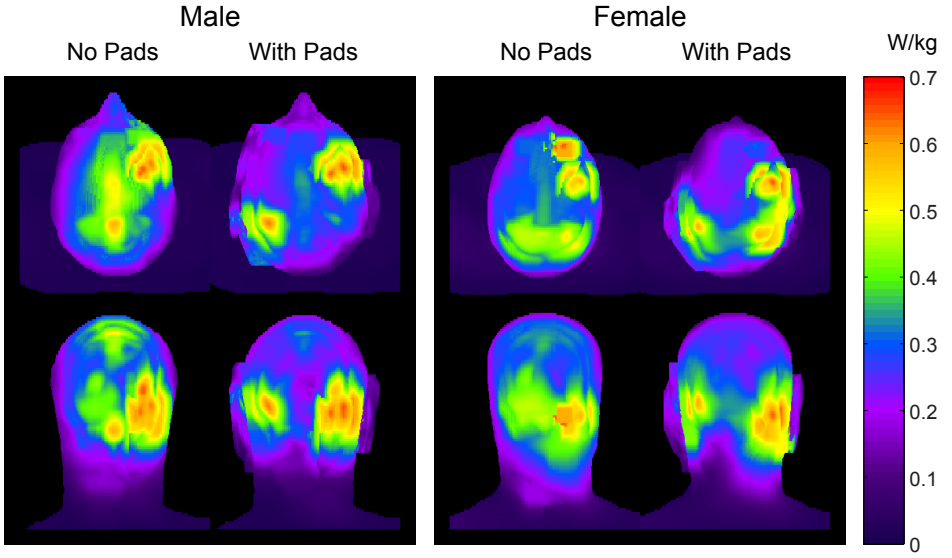

Figure 6.2: Transverse (top) and coronal (bottom) maximum intensity projections of the 10-g averaged SAR distribution for the male (left) and female (right) body model, without and with dielectric pads. Although the dielectric pads change the relative distribution of SAR within the head, they do not lead to an increase in the peak local SAR. All data are normalized to 1 W of dissipated power in tissue.

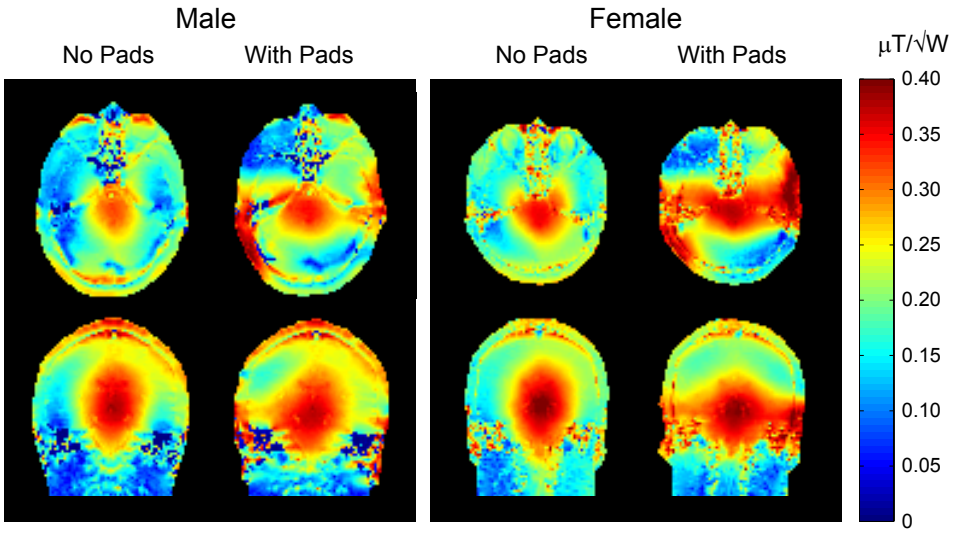

Figure 6.3: Transverse (top) and coronal (bottom) cross sections of the measured transmit efficiency in a male (left) and female (right) subject, without and with dielectric pads. The transmit efficiency maps show the effectiveness of the dielectric pads for locally tailoring the B_1^+ field. The measured field data are normalized to 1 W of transmitted power.

center of the brain; that is, the tip angle produced is higher than that which is optimized for the area of the inner ear. This is seen as a slightly reduced signal in the pons with respect to the inner ear.

Figure 6.5 shows multiplanar reconstructions of a high spatial resolution 3D data set, showing the depiction of fine anatomical structures, such as the modiolus, interscalar septum, and spiral osseous lamina. The isotropic voxels allow for oblique multiplanar reconstructions without loss of image quality, which is convenient for visualizing the different branches of the cochleovestibular nerve.

QUALITATIVE IMAGE ANALYSIS

The group results from the qualitative image analysis are presented in Table 1. The dielectric pads improve the mean scores significantly for all criteria evaluated with the exception of the visibility and diagnostic value of the left IAC, for which the image quality without pads was already very high without the dielectric pads. In addition, the dielectric pads improved the consistency of the image quality, which can be seen from the reduced standard deviations.

Intrarater agreement in both readers was good to very good with an intraclass correlation coefficient greater than 0.83. The interrater agreement was moderate to good with a κ value between 0.61 and 0.75.

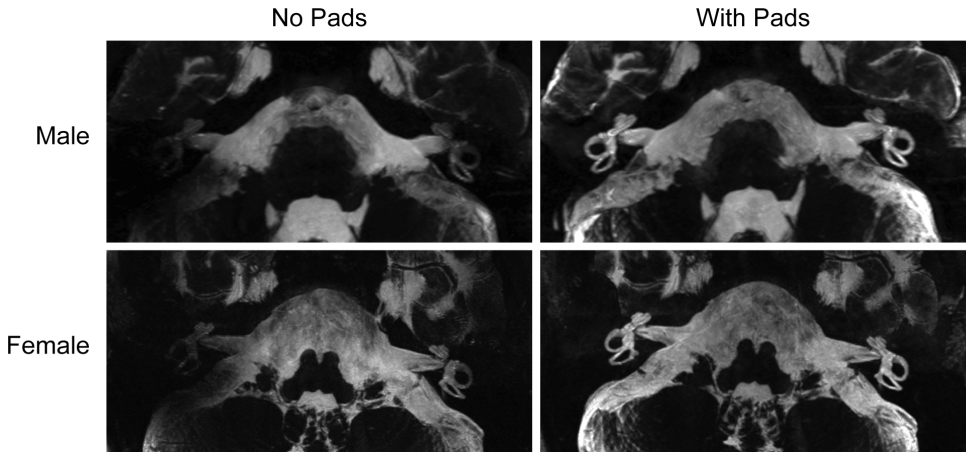

Figure 6.4: Transverse maximum intensity projections of the imaging results for a male (top) and female (bottom) subject, without (left) and with (right) dielectric pads. The introduction of the dielectric pads results in a much improved contrast homogeneity throughout the region of interest.

6.4. DISCUSSION

High spatial resolution MRI of the human inner ear is feasible at 7T by using geometrically tailored dielectric pads, enabling further clinical evaluation of this modality in both anatomical and diagnostic studies. By using dielectric pads filled with suspended barium titanate, which features a high permittivity, the severe B_1^+ inhomogeneities encountered in the temporal bone can be adequately corrected while satisfying the geometrical constraints imposed by the close-fitting 32-channel receiver array. The high spatial resolution improves the depiction of the fine structures of the inner ear, compared with MRI at lower fields, showing the potential benefit from ultrahigh-field MRI.

In this work, we have described two sex-specific geometrical designs for the dielectric pads, for either an average-sized male or female head. In cases wherein the head size deviated substantially from these averages, the design of the pads might have to be altered because the left-right differences in B_1^+ were found to be typically more severe in male subjects with larger head sizes than in female subjects. This trend can also be observed in Fig. 6.4, in which the left inner ear is better depicted in the female subject than in the male subject when no pads are being used.

Whereas imaging at 7T provides a higher intrinsic SNR compared with lower field strength acquisitions, by using a single surface coil for signal reception, scanning at a similar spatial resolution has been performed at 3T [29, 30]. Although a quantitative comparison of SNR has not been performed, the current results indicate that the image SNR at 7T is notably higher. Moreover, the contrast homogeneity is improved at 7T, especially at the IAC, because of the use of the 32-channel receive array instead of a single surface coil for signal reception. Future developments at 7T could incorporate reduced field-of-view imaging techniques to reduce the total imaging time, thereby reducing the potential degradation of the image quality due to physiological or motion-based artifacts [31].

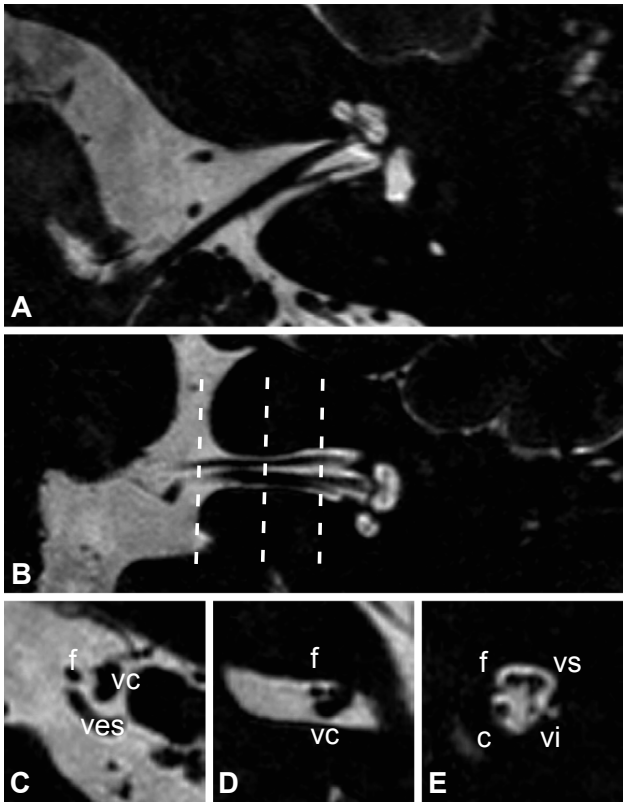

Figure 6.5: Multiplanar reconstructions of a high spatial resolution 3D-FSE data set, in which the depiction of inner ear microstructures can be appreciated (**A**–**B**). On reconstructions perpendicular to the internal auditory canal, the different branches of the cochleovestibular nerves are seen (**C**–**E**). The approximate locations are indicated by the dashed lines in (**B**). **c** indicates cochlear nerve; **f**, facial nerve; **vc**, vestibulochochlear nerve; **ves**, vessel (anterior inferior cerebellar artery); **vi**, inferior vestibular nerve; **vs**, superior vestibular nerve.

The geometrical design study indicated that asymmetrically sized pads were required to obtain a symmetric B_1^+ distribution at the level of the inner ear, which is explained by the intrinsic asymmetry observed when no pads are used. This has been consistently observed in vivo and is reproduced in electromagnetic simulations using a realistic numerical head model with inhomogeneous dielectric properties; which implies that this is a fundamental characteristic rather than related to subject positioning or malfunctioning of the RF coil. This B_1^+ asymmetry is known to increase with field strength [32]. Inhomogeneity of B_1^+, in general, has been studied extensively in the past at various field strengths and has been shown to be related to both the elliptical shape of the phantom and the electrical conductivity of the phantom liquid at 1.5T [15].

The use of dielectric materials for RF shimming has previously been shown to improve the transmit efficacy at high fields, with various applications at 3 and 7T [16–25]. The current work shows that the high permittivity afforded by using barium titanate allows compensation for the strong drop in B_1^+ present in the temporal bone while keeping the pad thickness practical. Care needs to be taken, however, that the field distribution is tailored in the desired way. This can be achieved by considering the initial field distribution, which can be dependent on the subject to a certain degree, and by proper geometrical arrangement of the high dielectric material around the subject. Specifically, a slightly larger pad should be used for male than for female subjects because of the larger head size. This underlines that high permittivity materials offer extended degrees of freedom for tailoring the RF field; however, these need to be addressed with appropriate care.

Correct positioning of the dielectric pads is important to obtain the full advantage of the locally enhanced B_1^+ field. Our approach in this study was to align them centrally with the ears, thus providing an easy anatomical landmark. Furthermore, local calibration of the transmit gain is an important step in obtaining the optimal tip angle at the area of interest, especially given the locally tailored B_1^+ field [33]. After global calibration, which was performed by the scanner in the transverse plane, we observed the estimated tip angle in the petrous bone to vary between 70% and 140% of the target angle because of the inhomogeneous B_1^+ field. Our approach was to obtain an estimate of the B_1^+ magnitude in the petrous bone from measurements of the B_1^+ in the surrounding tissue acquired with the dual refocused acquisition mode method [28]. The advantage of this technique, other than having a very short acquisition time, is its relative independence with respect to relaxation times and resonance frequency offsets. A small error in the B_1^+ estimate in tissues with a very short T_2^* has been observed and analyzed at 7T before; however, this was not a major issue in the current study because the T_2^* of the tissues surrounding the temporal bone is sufficiently long [28]. One remaining source of errors results from the fact that obtaining an estimate of the B_1^+ within the temporal bone was not possible because of the very poor SNR in this area. The accuracy of this may be improved by applying model-based reconstruction methods [34].

An alternative method for B_1^+ shimming at high fields is the use of transmit coil arrays, with dedicated RF signals applied to each channel. Some transmit array designs for imaging the inner ear at 7T have been proposed; however, the additional degrees of freedom present both opportunities as well as challenges with respect to coil implementation and SAR management [35, 36]. Spatially tailored RF pulses can also be used to compensate for B_1^+ inhomogeneities at high field. Although several developments yield

Table 6.1: Group Results of the Qualitative Image Assessment

	Reader A		Reader B	
	No Pads	With Pads	No Pads	With Pads
Contrast Homogeneity	2.0 (0.9)	3.7 (0.5)*	2.0 (0.7)	3.5 (0.6)*
Right ear				
SC	1.9 (0.7)	3.8 (0.4)*	1.8 (1.0)	3.8 (0.4)*
CO	2.4 (0.8)	3.7 (0.5)*	2.2 (1.1)	3.9 (0.3)*
IAC	2.6 (0.9)	3.8 (0.4)*	2.6 (1.0)	4.0 (0.2)*
Left ear				
SC	3.1 (0.6)	4.0 (0.0)*	3.4 (0.6)	4.0 (0.0)*
CO	3.1 (0.6)	3.9 (0.3)*	3.3 (0.7)	4.0 (0.0)*
IAC	3.6 (0.6)	3.7 (0.5)	3.7 (0.5)	4.0 (0.0)

SC indicates semicircular canal; CO, cochlea; IAC, internal auditory canal. Values are expressed as mean (SD). *Significant differences ($P < 0.001$).

promising results in this direction, none of these have yet been applied to high tip angle refocusing pulses of FSE sequences [37, 38]. Adiabatic and composite RF pulses have been applied in two-dimensional FSE and 3D FSE sequences at 7T both for excitation as well as for refocusing and show improvement in the excitation profile; however, this comes at the cost of increased imaging time due to SAR restrictions and increased interecho time, limiting the applicability when a 3D imaging volume is required [39, 40]. The advantages of using dielectric pads in this respect are that no additional hardware or software changes are required and that implementation is independent of vendor and platform, which improves the practicality of using this approach. One future improvement would be to combine the dielectric pads with tailored RF pulses. This would be useful for reducing the subject variability of the contrast homogeneity, by compensating for any remaining left-right asymmetry in B_1^+. Furthermore, tailored RF pulses enable compensation of the area of central brightening, which would improve the contrast homogeneity throughout the pons, for example. We note, however, that, in the clinical setting of inner ear and retrocochlear imaging, the assessment of the brain stem is typically performed by additional sequences that can be optimized separately.

In conclusion, this study shows that in vivo human inner ear imaging is feasible at 7T and that it is significantly improved by using geometrically tailored dielectric pads and renders images with high spatial resolution within reasonable acquisition time. The detailed visualization of the inner ear microstructures as well as cochleovestibular and facial nerve offers opportunities for both anatomical and diagnostic studies. This is of great interest for the development and application of patient-tailored treatment of hearing disorders and vestibular symptoms.

ACKNOWLEDGEMENTS

The authors thank Guido van Haren for his help in scoring the images and Dr. Erik van Zwet for his advice on performing the statistical analyses.

REFERENCES

[1] Horii A, Kitahara T, Osaki Y, Imai T, Fukuda K, Sakagami M, and Inohara H. Intractable benign paroxysmal positioning vertigo: long-term follow-up and inner ear abnormality detected by three-dimensional magnetic resonance imaging. Otology & Neurotology 2010; 31:250–255.

[2] Verbist BM. Imaging of sensorineural hearing loss: a pattern-based approach to diseases of the inner ear and cerebellopontine angle. Insights into Imaging 2011; 3:139–153.

[3] Carlson M, Van Abel K, Driscoll C, Neff BA, Beatty CW, Lane JI, Castner ML, Lohse CM, and Link MJ. Magnetic resonance imaging surveillance following vestibular schwannoma resection. The Laryngoscope 2012; 122:378–388.

[4] Pyykkö I, Nakashima T, Yoshida T, Zou J, and Naganawa S. Meniere's disease: a reappraisal supported by a variable latency of symptoms and the MRI visualisation of endolymphatic hydrops. BMJ open 2013; 3:1–10.

[5] Wippold, Franz J I, and Turski PA. Vertigo and Hearing Loss. American Journal of Neuroradiology 2009; 30:1623–1625.

[6] Wang G, Vannier MW, Skinner MW, Kalender WA, Polacin A, and Ketten DR. Unwrapping Cochlear implants by spiral CT. IEEE Transactions on Bio-Medical Engineering 1996; 43:891–900.

[7] Sobrinho FP Yoo HJ LPR, Lazarini PR, Yoo HJ, de Abreu Júnior L, and Meira AdS. A method for measuring the length of the cochlea through magnetic resonance imaging. Brazilian journal of otorhinolaryngology 2009; 75:261–267.

[8] Herman B, and Angeli S. Differences in cochlear nerve cross-sectional area between normal hearing and postlingually deafened patients on MRI. Otolaryngology–Head and Neck Surgery 2011; 144:64–66.

[9] Fishman AJ. Imaging and anatomy for cochlear implants. Otolaryngologic clinics of North America 2012; 45:1–24.

[10] Gibson D, Gluth MB, Whyte A, and Atlas MD. Rotation of the osseous spiral lamina from the hook region along the basal turn of the cochlea: results of a magnetic resonance image anatomical study using high-resolution DRIVE sequences. Surgical and radiologic anatomy: SRA 2012; 34:781–785.

[11] Kang WS, Hyun SM, Lim HK, Shim BS, Cho JH, and Lee KS. Normative diameters and effects of aging on the cochlear and facial nerves in normal-hearing Korean ears using 3.0-tesla magnetic resonance imaging. The Laryngoscope 2012; 122:1109–1114.

[12] Casselman JW, Kuhweide R, Ampe W, Meeus L, and Steyaert L. Pathology of the membranous labyrinth: comparison of T1- and T2-weighted and gadolinium-enhanced spin-echo and 3DFT-CISS imaging. American Journal of Neuroradiology 1993; 14:59–69.

[13] Naganawa S, Yamakawa K, Fukatsu H, Ishigaki T, Nakashima T, Sugimoto H, Aoki I, Miyazaki M, and Takai H. High-resolution T2-weighted MR imaging of the inner ear using a long echo-train-length 3D fast spin-echo sequence. European Radiology 1996; 6:369–374.

[14] Lane JI, Ward H, Witte RJ, Bernstein MA, and Driscoll CLW. 3-T imaging of the cochlear nerve and labyrinth in cochlear-implant candidates: 3D fast recovery fast spin-echo versus 3D constructive interference in the steady state techniques. American Journal of Neuroradiology 2004; 25:618–622.

[15] Sled JG, and Pike GB. Standing-wave and RF penetration artifacts caused by elliptic geometry: an electrodynamic analysis of MRI. IEEE Transactions on Medical Imaging 1998; 17:653–662.

[16] Yang QX, Mao W, Wang J, Smith MB, Lei H, Zhang X, Ugurbil K, and Chen W. Manipulation of image intensity distribution at 7.0 T: passive RF shimming and focusing with dielectric materials. Journal of Magnetic Resonance Imaging 2006; 24:197–202.

[17] Kataoka M, Isoda H, Maetani Y, Nakamoto Y, Koyama T, Umeoka S, Tamai K, Kido A, Morisawa N, Saga T, and Togashi K. MR imaging of the female pelvis at 3 Tesla: evaluation of image homogeneity using different dielectric pads. Journal of Magnetic Resonance Imaging 2007; 26:1572–1577.

[18] Haines K, Smith NB, and Webb AG. New high dielectric constant materials for tailoring the B1+ distribution at high magnetic fields. Journal of Magnetic Resonance 2010; 203:323–327.

[19] Snaar JEM, Teeuwisse WM, Versluis MJ, van Buchem MA, Kan HE, Smith NB, and Webb AG. Improvements in high-field localized MRS of the medial temporal lobe in humans using new deformable high-dielectric materials. NMR in Biomedicine 2011; 24:873–879.

[20] Yang QX, Wang J, Wang J, Collins CM, Wang C, and Smith MB. Reducing SAR and enhancing cerebral signal-to-noise ratio with high permittivity padding at 3 T. Magnetic Resonance in Medicine 2011; 65:358–362.

[21] Teeuwisse WM, Brink WM, and Webb AG. Quantitative assessment of the effects of high-permittivity pads in 7 Tesla MRI of the brain. Magnetic Resonance in Medicine 2012; 67:1285–1293.

[22] Teeuwisse WM, Brink WM, Haines KN, and Webb AG. Simulations of high permittivity materials for 7 T neuroimaging and evaluation of a new barium titanate-based dielectric. Magnetic Resonance in Medicine 2012; 67:912–918.

[23] de Heer P, Brink WM, Kooij BJ, and Webb AG. Increasing signal homogeneity and image quality in abdominal imaging at 3 T with very high permittivity materials. Magnetic Resonance in Medicine 2012; 68:1317–1324.

[24] Brink WM, and Webb AG. High permittivity pads reduce specific absorption rate, improve B1 homogeneity, and increase contrast-to-noise ratio for functional cardiac MRI at 3 T. Magnetic Resonance in Medicine 2014; 71:1632–1640.

[25] Yang QX, Rupprecht S, Luo W, Sica C, Herse Z, Wang J, Cao Z, Vesek J, Lanagan MT, Carluccio G, Ryu YC, and Collins CM. Radiofrequency field enhancement with high dielectric constant (HDC) pads in a receive array coil at 3.0T. Journal of Magnetic Resonance Imaging 2013; 38:435–440.

[26] Christ A, Kainz W, Hahn EG, Honegger K, Zefferer M, Neufeld E, Rascher W, Janka R, Bautz W, Chen J, Kiefer B, Schmitt P, Hollenbach HP, Shen J, Oberle M, Szczerba D, Kam A, Guag JW, and Kuster N. The Virtual Family—development of surface-based anatomical models of two adults and two children for dosimetric simulations. Physics in Medicine and Biology 2010; 55:N23–38.

[27] Nehrke K, and Börnert P. DREAM—A Novel Approach for Robust, Ultrafast, Multi-slice B1 Mapping. Magnetic Resonance in Medicine 2012; 68:1517–1526.

[28] Nehrke K, Versluis MJ, Webb A, and Börnert P. Volumetric B1+ Mapping of the Brain at 7T using DREAM. Magnetic Resonance in Medicine 2014; 71:246–256.

[29] Lane JI, Witte RJ, Bolster B, Bernstein MA, Johnson K, and Morris J. State of the art: 3T imaging of the membranous labyrinth. American Journal of Neuroradiology 2008; 29:1436–1440.

[30] Giesemann AM, Raab P, Lyutenski S, Dettmer S, Bültmann E, Frömke C, Lenarz T, Lanfermann H, and Goetz F. Improved imaging of cochlear nerve hypoplasia using a 3-Tesla variable flip-angle turbo spin-echo sequence and a 7-cm surface coil. The Laryngoscope 2014; 124:751–754.

[31] Wargo CJ, Moore J, and Gore JC. A comparison and evaluation of reduced-FOV methods for multi-slice 7T human imaging. Magnetic Resonance Imaging 2013; 31:1349–1359.

[32] Shajan G, Kozlov M, Hoffmann J, Turner R, Scheffler K, and Pohmann R. A 16-channel dual-row transmit array in combination with a 31-element receive array for human brain imaging at 9.4 T. Magnetic Resonance in Medicine 2014; 71:870–879.

[33] Takahara T, Hoogduin H, Visser F, Naganawa S, Kwee T, and Luijten PR. Imaging of the Inner Ear at 7T: Initial Results. In: Proceedings of the 18th Annual Meeting of ISMRM, Stockholm, Sweden, 2010; p. 4448.

[34] Sbrizzi A, Raaijmakers AJE, Hoogduin H, Lagendijk JJW, Luijten PR, and van den Berg CAT. Transmit and receive RF fields determination from a single low-tip-angle gradient-echo scan by scaling of SVD data. Magnetic Resonance in Medicine 2014; 72:248–259.

[35] Kim KN, Han GC, Heo P, Jeong H, Hong SM, Park JH, Woo MK, Kim YB, and Cho ZH. Potential and Probability of Inner Ear Magnetic Resonance Imaging at 7 T. In: Proceedings of the 21st Annual Meeting of ISMRM, Melbourne, Australia, 2013; p. 2725.

[36] Kim KN, Heo P, Han GC, Jeong H, Hong SM, Woo MK, Park JH, Kim YB, and Cho ZH. Hybrid RF Coils for Inner Ear Imaging at 7 T MR. In: Proceedings of the 21st Annual Meeting of ISMRM, Melbourne, Australia, 2013; p. 2726.

[37] Setsompop K, Wald LL, Alagappan V, Gagoski BA, and Adalsteinsson E. Magnitude least squares optimization for parallel radio frequency excitation design demonstrated at 7 Tesla with eight channels. Magnetic Resonance in Medicine 2008; 59:908–915.

[38] Grissom WA, Khalighi MM, Sacolick LI, Rutt BK, and Vogel MW. Small-tip-angle spokes pulse design using interleaved greedy and local optimization methods. Magnetic Resonance in Medicine 2012; 68:1553–1562.

[39] van Kalleveen IML, Koning W, Boer VO, Luijten PR, Zwanenburg JJM, and Klomp DWJ. Adiabatic turbo spin echo in human applications at 7 T. Magnetic Resonance in Medicine 2012; 68:580–587.

[40] Moore J, Jankiewicz M, Anderson AW, and Gore JC. Evaluation of non-selective refocusing pulses for 7 T MRI. Journal of Magnetic Resonance 2012; 214:212–220.

PART II

APPLIED ELECTROMAGNETICS IN THE CONTEXT OF MRI

Chapter 7

Ventricular B_1^+ perturbation at 7T – real effect or measurement artifact?

NMR Biomed 2014;27:617–620

Wyger M. Brink
Peter Börnert
Kay Nehrke
Andrew G. Webb

ABSTRACT

The objective of this work was to explore the origin of local B_1^+ perturbations in the ventricles measured at 7T.

The B_1^+ field in the human brain was mapped using four different MRI techniques: dual refocusing echo acquisition mode (DREAM), actual flip-angle imaging (AFI), saturated double-angle method (SDAM) and Bloch–Siegert shift (BSS). Electromagnetic field simulations of B_1^+ were performed in male and female subject models to assess the dependence of the B_1^+ distribution on the dielectric properties of cerebrospinal fluid and subject anatomy.

All four B_1^+ mapping techniques, based on different B_1^+ encoding mechanisms, show "residual" structure of the ventricles, with a slightly enhanced B_1^+ field in the ventricles. Electromagnetic field simulations indicate that this effect is real and arises from the strong contrast in electrical conductivity between cerebrospinal fluid and brain tissue. The simulated results were in good agreement with those obtained in three volunteers.

Measured local B_1^+ perturbations in the ventricles at 7T can be partially explained by the high contrast in electrical conductivity between cerebrospinal fluid and white matter, in addition to effects related to the particular B_1^+ measurement technique used.

7.1. INTRODUCTION

With a steady increase in the static field strengths commercially available for whole body scanning, the concomitant increases in Larmor frequency and associated decreases in RF wavelength lead to wave-propagation-induced RF inhomogeneities, which pose fundamental challenges to very high field MR [1]. Technical developments to manage these inhomogeneities at high field rely on accurate characterization of the transmit RF field (B_1^+), making accurate B_1^+ mapping techniques indispensable. These are needed, for example, for system calibration, RF shimming [2], transmit sensitivity encoding applications [3, 4], image processing to derive quantitative tissue parameters such as relaxation times and proton densities [5], and local specific absorption rate (SAR) estimation [6]. They are also important in specialized techniques such as MR-based electrical property tomography (EPT) [6–8].

Over the past decade, many techniques have been proposed for mapping the B_1^+ field in vivo, each based on different B_1^+ encoding mechanisms and therefore featuring a different sensitivity to resonance frequency offsets or relaxation mechanisms [5, 9–11]. Using these techniques, however, "residual" anatomical structure has been often observed in B_1^+ maps of the brain at 7T, in particular featuring a slightly enhanced value within the ventricles with a "jump" compared with surrounding tissue [12]. This localized perturbation in the ventricles, not to be confused with the global central brightening pattern observed in the brain at high fields, is typically interpreted as a relaxation-time-related artifact associated with the strong contrast in relaxation times between cerebrospinal fluid (CSF) and brain tissue [12, 13]. Much effort therefore has gone into reducing this sensitivity [9, 10, 12–14]. However, it has not been explored whether at least part of the "jump" is a real effect, arising from the high ionic concentrations present in CSF, indicating a high electrical conductivity compared with white matter [15]. This strong electrical contrast can potentially contribute to local distortions of the RF field in the ventricles.

In this work we study the degree of local B_1^+ perturbation in the ventricular system at 7T in four different B_1^+ mapping techniques. In addition, the B_1^+ field is simulated in a male and female subject model using electromagnetic simulations to assess the dependence on the electrical properties of CSF and subject anatomy. These results indicate the degree to which the local B_1^+ perturbation can be related to relaxation-time or other MR-related mechanisms compared with the intrinsic effects of electrical contrast.

7.2. MATERIALS AND METHODS

MRI SYSTEM AND PROTOCOLS

All experiments were performed on a Philips Achieva 7T MRI system (Philips Healthcare, Best, The Netherlands) equipped with a quadrature birdcage transmit–receive head coil and a 32-channel receive-only coil array (Nova Medical, Wilmington, MA, USA). Static magnetic field (B_0) shimming was performed up to the third order using a vendor-supplied image-based shimming routine. Phantom experiments were performed using a 17 cm diameter spherical phantom ("Braino," GE Medical Systems, Milwaukee, WI, USA), with contents as specified in [16]. In vivo experiments were performed on three healthy volunteers (three male, ages 26, 40, and 53 years) with written informed consent obtained. The study protocol was approved by the local medical ethics board.

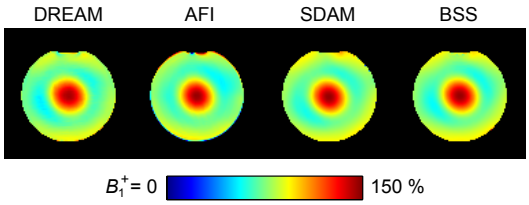

Figure 7.1: Phantom B_1^+ maps acquired with four different mapping techniques. All four techniques are able to capture the large dynamic range in B_1^+ observed at high fields. The scale represents percent of the nominal B_1^+, which was set to 20 µT.

B_1^+ maps were acquired using four different mapping techniques: dual refocusing echo acquisition mode (DREAM), actual flip-angle imaging (AFI), saturated double-angle method (SDAM) and Bloch–Siegert shift (BSS) [5, 9–11]. All data were acquired at a spatial resolution of $2.5 \times 2.5 \times 5$ mm^3 with a field of view of $240 \times 200 \times 25$ mm^3.

In the DREAM method, which was set up as a multi-slice single-shot magnetization-prepared turbo-gradient-echo sequence employing a low–high phase encoding order [12], the following sequence parameters were used: $TR/TE_{STE}/TE_{FID}$ = 6.7/2.3/4.6 ms, nominal STEAM tip angle $\alpha = 50°$, nominal imaging tip angle $\beta = 10°$. To reduce saturation effects resulting from slice profile imperfections [11], a multi-slice sequence was performed with a shot interval of 5000 ms. The AFI method was designed as a three-dimensional interleaved dual-TR gradient-echo sequence (5). The timings were set to $TR_1/TR_2/TE$ = 30/150/1.9 ms and the nominal tip angle was set to 40°. Gradient and RF spoiling were applied to suppress transverse coherences [14]. The SDAM sequence was configured as a multi-slice gradient-echo sequence with echo-planar-imaging readout [9]. Nominal tip angles were set to $\alpha_1/\alpha_2 = 60°/120°$, TR/TE = 5000/4.0 ms and a 500 ms saturation delay was used. Finally, the BSS method was set up as a multi-slice gradient-echo sequence with TR/TE = 200/15.8 ms, using a symmetric frequency offset of ±2 kHz, a pulse duration of 8 ms and an RF envelope with a nominal tip angle of 600° [10].

RF SIMULATIONS

The B_1^+ field was simulated using commercially available software (xFDTD, Remcom, State College, PA, USA). The head coil was modeled as a 16-rung high pass birdcage driven in its fundamental mode using voltage sources at the capacitor gaps, which is sufficient for modeling the local field interactions within the head model [17]. The geometry of the coil was based on the actual transmit coil. The "Duke" and "Ella" models from the Virtual Family dataset were used [18]. The entire configuration was simulated on a 2.5 mm isotropic grid. The dielectric properties of CSF were varied to assess the influence of the strong electric contrast between CSF and the surrounding brain tissue on the B_1^+ distribution. The electrical conductivity of CSF was varied from 0 to 3.0 S/m in steps of 1.0 S/m and its relative permittivity was varied from 1 to 120 in steps of 40. Literature values for the electrical conductivity and relative permittivity of CSF are 2.2 S/m and 73, whereas those for the surrounding white matter are 0.4 S/m and 44, respectively [15]. While studying the effects of varying the electrical conductivity, the relative permittivities of tissues were fixed at these literature values, and vice versa.

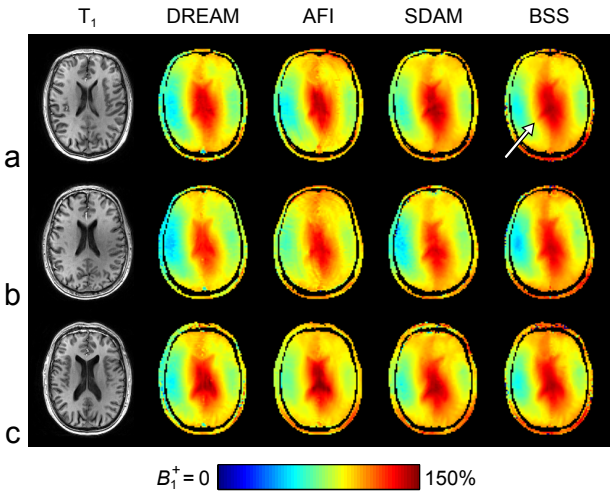

Figure 7.2: In vivo B_1^+ maps showing the ventricular B_1^+ perturbation. The transverse maps were acquired in three volunteers (**a-c**) with four different mapping techniques showing a pronounced local perturbation of the B_1^+ in the ventricles (arrow). The scale represents percent of the nominal B_1^+ (20 μT).

7.3. RESULTS

Figure 7.1 shows experimental B_1^+ maps acquired in the spherical phantom, which demonstrates good agreement between the different mapping techniques used. The central brightening effect is clearly pronounced, with a large inhomogeneity across the diameter of the phantom. This showed that all mapping techniques are essentially able to record the large dynamic range in B_1^+.

Figure 7.2 shows the in vivo B_1^+ maps in the different volunteers obtained using the four different mapping techniques, together with a T_1-weighted anatomical reference image. The local enhancement of B_1^+ in the ventricles is clear in all datasets, with small differences among the acquisition techniques used.

Figure 7.3 shows transverse B_1^+ maps at the level of the ventricles with different dielectric properties assigned to CSF. All simulated B_1^+ maps were scaled to the maximum value in the corresponding axial cross-section. As the electrical conductivity increases (with the relative permittivity kept fixed at its literature value), the local B_1^+ perturbation in the ventricles becomes more pronounced in both subject models, as shown in Fig. 7.3(a). The permittivity of CSF has a much smaller effect, as shown in Fig. 7.3(b). Around the literature values (2.2 S/m and 73 for electrical conductivity and relative permittivity, respectively) the contours of the ventricles are clearly depicted in the simulated B_1^+ maps, meaning that ventricular B_1^+ enhancement is a real effect. Subtle differences around the ventricles between the two subject models can be observed.

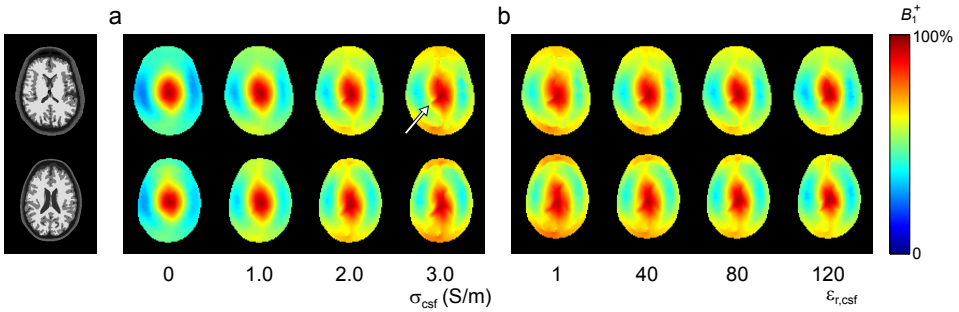

Figure 7.3: B_1^+ maps simulated with different dielectric properties assigned to CSF. Both the male ("Duke," top row) and female ("Ella," bottom row) body perturbation in the ventricles (arrow) and the electrical conductivity of CSF (σ_{csf}) (**a**). Changes in the relative permittivity of CSF ($\varepsilon_{r,csf}$) have a much smaller effect (**b**). All maps are scaled to their respective maxima and literature values were assigned to all tissue parameters that remained fixed.

7.4. DISCUSSION

These results show that local B_1^+ perturbations in the ventricles can be partially explained by the intrinsic strong contrast in electrical conductivity of CSF with respect to brain tissue, in addition to relaxation-time-related and other MR effects. The experimental and simulation data presented here show that the magnitude of the perturbation depends on the dielectric properties of CSF as well as subject anatomy, in addition to the B_1^+ measurement technique used, which indicates that each technique has a slightly different sensitivity to relaxation-time related mechanisms.

The simulation results indicate that the effect is most dependent on the contrast in electrical conductivity between CSF and white matter, which is about a factor of five [15]. The contrast in permittivity is much lower, and the simulations also show that permittivity *per se* has a much lower effect on the local B_1^+ properties, both of which indicate a reduced sensitivity of the B_1^+ to this parameter. Fundamentally, the influence of these parameters can be linked to the induced currents. A local increase in the electrical conductivity can attract induced current densities, which in turn generate a secondary B_1^+ field component that can lead to localized B_1^+ perturbations. The total induced current density $\boldsymbol{J}_i$ is typically written as the sum of the conduction current density $\boldsymbol{J}_c$ and the displacement current density $\boldsymbol{J}_d$, as follows:

$$\boldsymbol{J}_i = \boldsymbol{J}_c + \boldsymbol{J}_d = \sigma \boldsymbol{E} + j\omega\varepsilon \boldsymbol{E} \tag{7.1}$$

in which σ is the electrical conductivity in S/m, ω denotes the angular frequency in rad/s and ε denotes the permittivity. The magnitude ratio of the conduction and displacement current densities can then be written as

$$\frac{|\boldsymbol{J}_c|}{|\boldsymbol{J}_d|} = \frac{\sigma}{\omega\varepsilon} \tag{7.2}$$

which for white matter yields ~0.5, for gray matter ~0.7 and for CSF ~1.8. This means that in CSF the conduction current is intrinsically larger than the displacement current,

which also explains the strong influence of this parameter on the B_1^+ distribution. The higher sensitivity of the B_1^+ field to electrical conductivity in general can be linked to similar findings in EPT, where in a phantom experiment the noise level in the conductivity maps was found to be consistently lower than in the permittivity maps [8]. This indicates a stronger effect of conductivity than permittivity on the B_1^+ distribution.

A strong agreement in the local B_1^+ enhancement of ~6% around the tip of the right posterior ventricular horn can be observed when comparing the B_1^+ maps acquired in the first volunteer (Fig. 7.2(a)) using the BSS method and the B_1^+ maps simulated in the "Duke" model at a realistic conductivity of 2.0 S/m (Figure 7.3(a)). The BSS method has been reported previously to be less sensitive to T_1 effects and improves the B_1^+ estimation in the ventricles at 3T compared with other methods [10]. In the present case, the residual ventricular structure visible in the BSS B_1^+ map is in good agreement with the simulations and therefore should not be interpreted as being merely an artifact; it should be considered as a real effect. The ventricular B_1^+ perturbation appears to be largest for the DREAM method, which indicates that its sensitivity to relaxation time contrasts is higher than in the other techniques studied here. The DREAM method was set up using relatively long echo times, which together with the relatively long shot length of approximately 275 ms is known to lead to a slightly suboptimal B_1^+ estimation in the ventricles. This can be substantially improved by reducing the shot length and changing the sequence timings [12].

The depiction of the ventricles in a B_1^+ map differs from subject to subject, which may originate from anatomical differences as indicated by the simulation results from the male and female body models, as well as from differences in the electrical properties of the tissue. For example, it is known that the dielectric properties of white matter are dependent on age, which changes the electric contrast with CSF in the ventricles [15]. At the same time, the dielectric properties of CSF vary with glucose or protein levels, meaning that the local B_1^+ perturbation can change between and within subjects [19]. The results shown here therefore indicate that, if one aims to reconstruct the subject-specific electrical properties in the human brain, ventricular perturbations of the B_1^+ should not be compensated prior to reconstruction. Other applications in which a correct B_1^+ map is critical include local SAR estimation, for which it is known that strongly conductive tissues such as CSF can produce "hotspots" [20], and imaging sequences that feature a strong signal intensity dependence on B_1^+, for example Fast Spin Echo imaging of short T_2 species [21].

We note finally that in the current study the slice thickness was limited to 5 mm (a commonly used value in B_1^+ mapping sequences) in order to capture the detailed B_1^+ features around the ventricles. Ultimately, these features pose a constraint to B_1^+ mapping at lower spatial resolution, since the B_1^+ estimate around the ventricles can be biased due to partial volume effects.

ACKNOWLEDGEMENTS

We would like to acknowledge the help of Dr. Baolian Yang and Dr. Vincent Boer for implementing parts of the B_1^+ mapping techniques.

REFERENCES

[1] Hoult DI. Sensitivity and Power Deposition in a High-Field Imaging Experiment. Journal of Magnetic Resonance Imaging 2000; 12:46–67.

[2] Metzger GJ, Snyder C, Akgun C, Vaughan T, Ugurbil K, and Van de Moortele PF. Local B1+ shimming for prostate imaging with transceiver arrays at 7T based on subject-dependent transmit phase measurements. Magnetic Resonance in Medicine 2008; 59:396–409.

[3] Katscher U, Börnert P, Leussler C, and van den Brink JS. Transmit SENSE. Magnetic Resonance in Medicine 2003; 49:144–150.

[4] Zhu Y. Parallel excitation with an array of transmit coils. Magnetic Resonance in Medicine 2004; 51:775–784.

[5] Yarnykh VL. Actual flip-angle imaging in the pulsed steady state: a method for rapid three-dimensional mapping of the transmitted radiofrequency field. Magnetic Resonance in Medicine 2007; 57:192–200.

[6] Katscher U, Voigt T, Findeklee C, Vernickel P, Nehrke K, and Dössel O. Determination of electric conductivity and local SAR via B1 mapping. IEEE Transactions on Medical Imaging 2009; 28:1365–1374.

[7] Katscher U, Voigt T, and Findeklee C. Electrical conductivity imaging using magnetic resonance tomography. In: Proceedings of the 31st Annual Meeting IEEE Engineering in Medicine and Biology Society, Minneapolis, 2009; pp. 3162–3164.

[8] van Lier ALHMW, Brunner DO, Pruessmann KP, Klomp DWJ, Luijten PR, Lagendijk JJW, and van den Berg CAT. B1(+) phase mapping at 7 T and its application for in vivo electrical conductivity mapping. Magnetic Resonance in Medicine 2012; 67:552–561.

[9] Cunningham CH, Pauly JM, and Nayak KS. Saturated double-angle method for rapid B1+ mapping. Magnetic Resonance in Medicine 2006; 55:1326–1333.

[10] Sacolick LI, Wiesinger F, Hancu I, and Vogel MW. B1 mapping by Bloch-Siegert shift. Magnetic Resonance in Medicine 2010; 63:1315–1322.

[11] Nehrke K, and Börnert P. DREAM—A Novel Approach for Robust, Ultrafast, Multi-slice B1 Mapping. Magnetic Resonance in Medicine 2012; 68:1517–1526.

[12] Nehrke K, Versluis MJ, Webb A, and Börnert P. Volumetric B1+ Mapping of the Brain at 7T using DREAM. Magnetic Resonance in Medicine 2014; 71:246–256.

[13] Volz S, Nöth U, Rotarska-Jagiela A, and Deichmann R. A fast B1-mapping method for the correction and normalization of magnetization transfer ratio maps at 3 T. NeuroImage 2010; 49:3015–3026.

[14] Yarnykh VL. Optimal radiofrequency and gradient spoiling for improved accuracy of T1 and B1 measurements using fast steady-state techniques. Magnetic Resonance in Medicine 2010; 63:1610–1626.

[15] Peyman A, Holden SJ, Watts S, Perrott R, and Gabriel C. Dielectric properties of porcine cerebrospinal tissues at microwave frequencies: in vivo, in vitro and systematic variation with age. Physics in Medicine and Biology 2007; 52:2229–2245.

[16] Barker PB, Hearshen DO, and Boska MD. Single-voxel proton MRS of the human brain at 1.5T and 3.0T. Magnetic Resonance in Medicine 2001; 45:765–769.

[17] Collins CM, and Smith MB. Signal-to-noise ratio and absorbed power as functions of main magnetic field strength, and definition of "90 degrees" RF pulse for the head in the birdcage coil. Magnetic Resonance in Medicine 2001; 45:684–691.

[18] Christ A, Kainz W, Hahn EG, Honegger K, Zefferer M, Neufeld E, Rascher W, Janka R, Bautz W, Chen J, Kiefer B, Schmitt P, Hollenbach HP, Shen J, Oberle M, Szczerba D, Kam A, Guag JW, and Kuster N. The Virtual Family—development of surface-based anatomical models of two adults and two children for dosimetric simulations. Physics in Medicine and Biology 2010; 55:N23–38.

[19] Lonappan A, Thomas V, Bindu G, Rajasekaran C, and Mathew KT. Analysis of Human Cerebro Spinal Fluid at the ISM Band of Frequencies. Journal of Electromagnetic Waves and Applications 2006; 20:773–779.

[20] Wolf S, Diehl D, Gebhardt M, Mallow J, and Speck O. SAR simulations for high-field MRI: How much detail, effort, and accuracy is needed? Magnetic Resonance in Medicine 2013; 69:1157–1168.

[21] Zwanenburg JM, Visser F, Hendrikse J, and Luijten PR. Unexpected lateral asymmetry in TSE image contrast explained: tissues with short T2 show extreme sensitivity to B1 inhomogeneity. In: Proceedings of the 21st Annual Meeting of ISMRM, Salt Lake City, UT, USA, 2013; p. 368.

Chapter 8

A Forward Model Analysis of Dielectric Shimming in Magnetic Resonance Imaging

Proc ICEAA 2013;528–531

W.M. Brink
A.G. Webb

ABSTRACT

This work evaluates a formulation of the integral equations method to model the field pertubation introduced by a dielectric material in a radiofrequency field typical to a magnetic resonance imaging experiment. The approach incorporates the inhomogeneous body model into the Green's function. The accuracy of the Neumann series expansion is validated against the full numerical solution for different dielectric permittivities and series lengths. This framework can be used for gaining insight into the design considerations and, ultimately, can be embedded in future inverse design strategies.

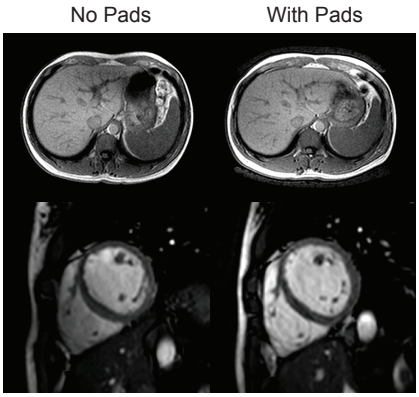

Figure 8.1: Example abdominal (top) and cardiac (bottom) images obtained at a static field strength of 3T, both without (left) and with (right) dielectric pads.

8.1. INTRODUCTION

Increasing the static field strength in magnetic resonance imaging (MRI) increases both the intrinsic SNR but also the technical demands. With the increase in field strength, the increased frequency of the radiofrequency (RF) field introduces standing wave behavior within the subject, which gives rise to inhomogeneities in the sensitivity profile and corresponding intensity artifacts in the images [1].

Various strategies have been developed to overcome these sample-induced inhomogeneities, such as the use of transmit arrays with a variable phase and magnitude on each of the channels to adapt the RF field to a specific body geometry. Another approach introduces additional dielectric materials to tailor the RF field, exploiting the interactions that gave rise to the inhomogeneities in the first place [2]. Two recent examples of these materials applied in MRI body imaging at 3T, which is related to an RF frequency of 128 MHz, are shown in Fig. 8.1 [3, 4]. It has been shown that this approach can outperform the use of multiple transmit channels in terms of homogeneity and tissue power deposition: however, determining the optimal design of these pads remains a non-trivial task. Some analytical models have been proposed which offer insight into some fundamental behavior [5], but fail to incorporate geometrical considerations such as dimensions or positioning of the pads which can be very important in local tailoring of the RF field.

As is often encountered in electromagnetic engineering, one possible strategy to address a design problem is to pose it as an inverse problem. In our case one can define a target field distribution for which one aims, then reconstruct the distribution of dielectric material which tailors the RF field in this way. Initial tests at our institution have indicated that such a procedure is feasible as an iterative method in which a forward problem is solved between each of the material updates. This is, however, a very inefficient strategy. Some methods avoid this by updating both the field and material quantities consecutively at each iteration [6]. However, due to the high permittivity materials often used in the current type of application the convergence speed of this algorithm was found to be even slower.

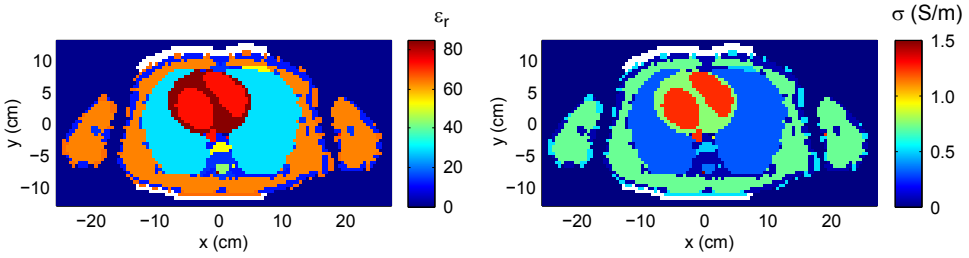

Figure 8.2: Relative permittivity of the two-dimensional configuration, with the dielectric pads displayed in white.

One way of improving the convergence speed in inverse algorithms is by incorporating known parts of the configuration, like a background medium, into the algorithm. In some methods this background medium is taken as a starting point for the algorithm [7], whereas in others it is explicitly incorporated into the Green's function at the expense of additional computational cost [8, 9]. Which method is most suitable depends on the specific inverse problem at hand. Therefore, the analysis of the associated forward problem can provide insight into what strategy would be most suitable.

In this contribution we evaluate a numerical framework for modeling the forward problem regarding the field perturbation or "secondary field" generated by a dielectric pad introduced in a radiofrequency field typical to a magnetic resonance imaging experiment. An approximate solution using the Neumann series expansion is evaluated by testing its accuracy for different values of the permittivity and different extents of the series expansion. This framework can be embedded in future inverse design strategies.

8

8.2. METHODS

8.2.1. TWO-DIMENSIONAL MODEL

Our investigation is guided by a two-dimensional model of a 3T body imaging setup with the body transmit coil modeled through a 30 cm radius circular array of 16 line sources each driven with a unit electric current. The array is driven at a frequency of 128 MHz with a $[0, 2\pi]$ phase evolution along its circumference to set up a circular polarized magnetic field. A transverse cross section of the numerical body model "Duke" from the Virtual Family dataset was used to model the human body [10], centered at the heart. Dielectric pads were introduced on the anterior and posterior side of the thorax as described in [4]. The configuration is present in the computational domain $\mathscr{D} \in \mathbb{R}^2$ in which $\boldsymbol{r} = (x, y)$ denotes the position vector in the transverse plane. The permittivity distribution is illustrated in Fig. 8.2 with the dielectric pads indicated in white. The RF field in the two-dimensional configuration is described using an integral equation approach, in which we choose an $e^{j\omega t}$ time dependence. All numerical computations are performed using the discretized iterative conjugate gradient method as described in [11] using a uniform 5-mm grid.

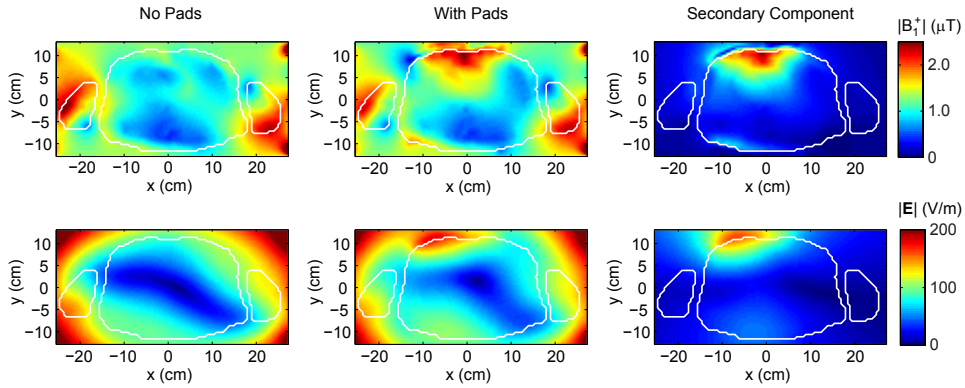

Figure 8.3: Magnitude of the B_1^+ - (top) and $\boldsymbol{E}$-fields (bottom) in the configuration without (left) and with (center) dielectric pads of $\varepsilon_r = 300$ and their corresponding secondary component (right).

8.2.2. FORMULATION OF THE SECONDARY FIELD

In our formulation of the problem we start with the inhomogeneous body model as the background medium, characterised by the complex relative permittivity $\varepsilon_{r,b}$, such that the remaining contrasting material parameter $\Delta\chi$ is related to the dielectric pads. At this stage we note that $\Delta\chi$ is assumed not to overlap with the background medium, i.e. their domains do not intersect. Let $\boldsymbol{E}^b$ and $\boldsymbol{H}^b$ denote the fields present in the background medium, i.e. without any dielectric pads. The total electric field $\boldsymbol{E}$ then satisfies

$$\boldsymbol{E}(\boldsymbol{r}) = \boldsymbol{E}^b(\boldsymbol{r}) + \int_{\boldsymbol{r}'\in\mathscr{D}} g_b(\boldsymbol{r}-\boldsymbol{r}')\Delta\chi(\boldsymbol{r}')\boldsymbol{E}(\boldsymbol{r}')\mathrm{d}V \tag{8.1}$$

in which $g_b(\boldsymbol{r}-\boldsymbol{r}')$ represents the background Green's function, which needs to be evaluated numerically due to the inhomogeneous background medium, and

$$\Delta\chi(\boldsymbol{r}) = \chi(\boldsymbol{r}) - \chi_b(\boldsymbol{r}) \tag{8.2}$$

describes the susceptibility perturbation with $\chi_b = \varepsilon_{r,b} - 1$ denoting the background susceptibility and χ denoting the total susceptibility.

The total magnetic field $\boldsymbol{H}$ follows through the integral expression

$$\boldsymbol{H}(\boldsymbol{r}) = \boldsymbol{H}^b(\boldsymbol{r}) + \int_{\boldsymbol{r}'\in\mathscr{D}} \nabla g_b(\boldsymbol{r}-\boldsymbol{r}') \times \Delta\chi(\boldsymbol{r}')\boldsymbol{E}(\boldsymbol{r}')\mathrm{d}V\,. \tag{8.3}$$

The transmit sensitivity profile in an MRI experiment, denoted as B_1^+, is defined through the forward circular polarized component of the magnetic flux density $\boldsymbol{B} = \mu_0\boldsymbol{H}$, as follows

$$B_1^+(\boldsymbol{r}) = \frac{B_x(\boldsymbol{r}) + \mathrm{j}B_y(\boldsymbol{r})}{2} \tag{8.4}$$

in which the static field is assumed to be oriented in the +z-direction.

Finally, by writing the total field quantities as $\boldsymbol{E} = \boldsymbol{E}^{\mathrm{b}} + \boldsymbol{E}^{\mathrm{s}}$, and $\boldsymbol{H} = \boldsymbol{H}^{\mathrm{b}} + \boldsymbol{H}^{\mathrm{s}}$, we can obtain the expression for the secondary fields

$$\boldsymbol{E}^{\mathrm{s}}(\boldsymbol{r}) = \int_{\boldsymbol{r}' \in \mathscr{D}} g_{\mathrm{b}}(\boldsymbol{r} - \boldsymbol{r}') \Delta\chi(\boldsymbol{r}') \boldsymbol{E}(\boldsymbol{r}') \mathrm{d}V \tag{8.5}$$

and

$$\boldsymbol{H}^{\mathrm{s}}(\boldsymbol{r}) = \int_{\boldsymbol{r}' \in \mathscr{D}} \nabla g_{\mathrm{b}}(\boldsymbol{r} - \boldsymbol{r}') \times \Delta\chi(\boldsymbol{r}') \boldsymbol{E}(\boldsymbol{r}') \mathrm{d}V . \tag{8.6}$$

8.2.3. APPROXIMATE SOLUTION

To reduce the computational cost of the forward problem, an approximate solution to Equation (8.1) is set up by iterating the equation, which is known as the Neumann series expansion. This expansion is given by

$$\boldsymbol{E}(\boldsymbol{r}) = \sum_{n=0}^{\infty} \boldsymbol{E}_{\mathrm{n}}(\boldsymbol{r}) \tag{8.7}$$

in which

$$\boldsymbol{E}_0(\boldsymbol{r}) = \boldsymbol{E}^{\mathrm{b}}(\boldsymbol{r}) \tag{8.8}$$

$$\boldsymbol{E}_{\mathrm{n+1}}(\boldsymbol{r}) = \int_{\boldsymbol{r}' \in \mathscr{D}} g_{\mathrm{b}}(\boldsymbol{r} - \boldsymbol{r}') \Delta\chi(\boldsymbol{r}') \boldsymbol{E}_{\mathrm{n}}(\boldsymbol{r}') \mathrm{d}V . \tag{8.9}$$

The approximated magnetic field values follow from inserting Equation (8.7) into Equation (8.3). The series expansion may be truncated at any desired series length N, depending on the convergence properties of the series and the desired accuracy.

The convergence of the Neumann series is evaluated through the normalized root-mean-square error (RME) of the approximated total B_1^+-field with the full numerical solution $B_{1,\mathrm{full}}^+$ obtained by evaluating the full forward problem with dielectric pads, through the following measure

$$\mathrm{RME} = \frac{\left\| B_1^+ - B_{1,\mathrm{full}}^+ \right\|}{\left\| B_{1,\mathrm{full}}^+ \right\|} \tag{8.10}$$

in which $\|.\|$ denotes the norm over the domain $\mathscr{D}$.

8.3. RESULTS

Fig. 8.3 shows the magnitude of the B_1^+- and $\boldsymbol{E}$-fields in the configuration without and with dielectric pads of $\varepsilon_{\mathrm{r}} = 300$, together with the magnitude of the secondary fields. As can be seen from the amplitude of the secondary fields, the magnitude of the field perturbation is strongest close to the pads, which is explained by the high electric current density in the dielectric material and the spatial decay of the Green's function. Another interesting observation is that the enhancement in the B_1^+-field is mainly inside the body, which explains the effectiveness of this approach in MRI.

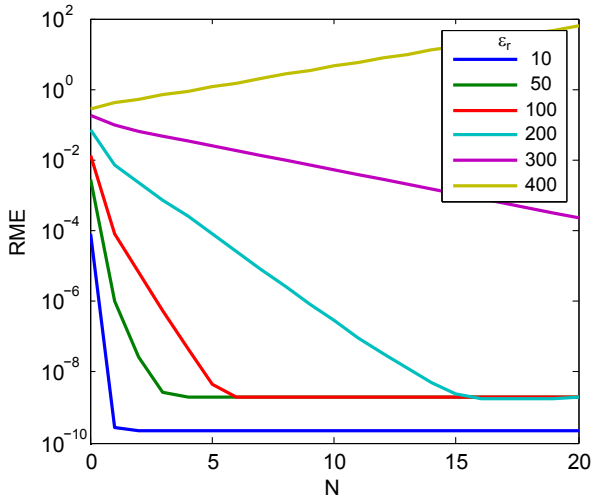

Figure 8.4: Convergence plot of the Neumann series expansion for the secondary field, for different values of the pad permittivity ε_r and series length N.

The convergence of the Neumann series expansion is illustrated in Fig. 8.4 for different values of the pad permittivity and series length N. As can be seen from the graph, in the current configuration the series expansion diverges for values of the pad permittivity $\varepsilon_r \geq 400$. This reflects that the series expansion is only convergent up to a certain level of electromagnetic interaction. We also note that the field error at $N = 0$, which corresponds to the so-called "Born approximation," increases for increasing permittivity. This indicates that the born approximation is not accurate enough for this application. The Neumann series improves the accuracy up to $\varepsilon_r \approx 300$. In the associated inverse algorithm, one could regain accuracy for higher permittivities as well by updating the background medium and recomputing the Green's function, along the lines of the "Distorted Born" method [9]. Finally, we note that the convergence properties might be different in a three-dimensional model due to the increased spatial decay of the Green's function, but this remains a topic for further investigation.

8.4. CONCLUSIONS

The forward problem considering the effects of a dielectric material in the RF field typical to an MRI experiment can be formulated in terms of the field perturbation or "secondary field," which considers the dielectric as the contrasting material parameter and the body as the background medium. By incorporating the background medium into the Green's function, we see that the Neumann series expansion can efficiently approximate the total fields up to a relative permittivity of 300.

ACKNOWLEDGMENTS

The authors acknowledge Dr. Rob Remis for discussions on forward modeling schemes.

REFERENCES

[1] Webb AG, and Collins CM. Parallel transmit and receive technology in high-field magnetic resonance neuroimaging. International Journal of Imaging Systems and Technology 2010; 20:2–13.

[2] Haines K, Smith NB, and Webb AG. New high dielectric constant materials for tailoring the B1+ distribution at high magnetic fields. Journal of Magnetic Resonance 2010; 203:323–327.

[3] de Heer P, Brink WM, Kooij BJ, and Webb AG. Increasing signal homogeneity and image quality in abdominal imaging at 3 T with very high permittivity materials. Magnetic Resonance in Medicine 2012; 68:1317–1324.

[4] Brink WM, and Webb AG. High permittivity pads reduce specific absorption rate, improve B1 homogeneity, and increase contrast-to-noise ratio for functional cardiac MRI at 3 T. Magnetic Resonance in Medicine 2014; 71:1632–1640.

[5] Jayatilake ML, Storrs J, Chu WJ, and Lee JH. Theoretical determination of the dielectric constant for passive RF shimming at high field. In: Proceedings of the 19th Annual Meeting of ISMRM, Montreal, Canada, 2011; p. 3887.

[6] Kleinman RE, and van den Berg PM. A modified gradient method for two- dimensional problems in tomography. Journal of Computational and Applied Mathematics 1992; 42:17–35.

[7] Tijhuis AG, Belkebir K, Litman ACS, and de Hon BP. Multiple-frequency distorted-wave Born approach to 2D inverse profiling. Inverse Problems 2001; 17:1635–1644.

[8] Wang YM, and Chew WC. An iterative solution of the two-dimensional electromagnetic inverse scattering problem. International Journal of Imaging Systems and Technology 1989; 1:100–108.

[9] Chew WC, and Wang YM. Reconstruction of two-dimensional permittivity distribution using the distorted Born iterative method. IEEE Transactions on Medical Imaging 1990; 9:218–225.

[10] Christ A, Kainz W, Hahn EG, Honegger K, Zefferer M, Neufeld E, Rascher W, Janka R, Bautz W, Chen J, Kiefer B, Schmitt P, Hollenbach HP, Shen J, Oberle M, Szczerba D, Kam A, Guag JW, and Kuster N. The Virtual Family—development of surface-based anatomical models of two adults and two children for dosimetric simulations. Physics in Medicine and Biology 2010; 55:N23–38.

[11] Zwamborn P, and van den Berg PM. A Weak Form of the Conjugate Gradient FFT Method for Two-Dimensional TE Scattering Problems. IEEE Transactions on Microwave Theory and Techniques 1991; 39:953–960.

Chapter 9

A Theoretical Approach Based on Electromagnetic Scattering for Analysing Dielectric Shimming in High-Field MRI

Mag Reson Med 2015; ***in press***

W.M. Brink
R.F. Remis
A.G. Webb

ABSTRACT

Purpose: In this study, we analyzed dielectric shimming by formulating it as an electromagnetic scattering problem using integral equations.

Methods: Three-dimensional simulations of the radiofrequency field in two configurations using different materials were analyzed in terms of induced currents and secondary fields. A two-dimensional integral equation method with different backgrounds was used to identify the underlying physical mechanisms. This framework was then used to develop an inversion method for the design of dielectric pads.

Results: The effects of a dielectric pad can be attributed to the interference of a secondary field that is produced by the currents induced in the dielectric pad, radiating in an inhomogeneous background. The integral equation method with inhomogeneous background reduces the complexity of the forward and inverse problem significantly and can be used to optimize the permittivity distribution for a desired B_1^+ field. Agreement with experimental B_1^+ maps was obtained in a cylindrical phantom, demonstrating the validity of the method.

Conclusion: The integral equation method with inhomogeneous background yields an efficient numerical framework for the analysis and inverse design of dielectric shimming materials.

9.1. INTRODUCTION

The use of high permittivity ($\varepsilon_r > 100$) dielectric materials has been shown to be an effective method for addressing transmit (B_1^+) inhomogeneities in various applications of high-field MRI, such as body imaging at 3T [1–5] and neuroimaging at 7T [6–9]. The term "high-field" here denotes that the dimensions of the body part being imaged are comparable to the radiofrequency (RF) wavelength. The resulting standing wave patterns in the subject decrease the B_1^+ uniformity, leading to spatially variant contrast, or image shading, and a decreased diagnostic value. These patterns can be altered significantly by introducing dielectric materials between the RF coil and the subject, a technique sometimes referred to as "dielectric shimming." Various beneficial effects of this approach have been evaluated in the literature, including an improved B_1^+ homogeneity, reduced specific absorption rate (SAR), and increased receive sensitivity [1–11].

Despite significant efforts to characterize and explain the mechanisms underlying these improvements, the existing literature remains limited to intuitive formulations that can at most guide the operator during judicious placement of a dielectric pad. The most general zero-order formulation is that induced currents are produced in the dielectric material, which act as secondary RF sources, effectively superimposing a secondary RF field on the primary RF field produced without dielectric material [1, 3, 10, 12]. This reasoning stems from the time-harmonic form of Ampère's law, given by

$$\nabla \times \boldsymbol{B} = \mu(\boldsymbol{J}_i + \boldsymbol{J}_s) \tag{9.1}$$

where $\boldsymbol{B}$ is the magnetic flux density, $\mu \approx \mu_0$ is the permeability of tissue, and $\boldsymbol{J}_i$ and $\boldsymbol{J}_s$ represent the induced (passive) and source (active) current densities, respectively. The induced current density, which reflects the presence of a dielectric pad, is given by

$$\boldsymbol{J}_i = (\sigma + j\omega\varepsilon_0\varepsilon_r)\boldsymbol{E} \tag{9.2}$$

where σ represents electrical conductivity, j is the imaginary unit, ω represents the angular frequency, ε_0 and ε_r represent the permittivity of free space and relative permittivity of the dielectric pad, respectively, and $\boldsymbol{E}$ represents the electric field strength. This interpretation has supported some empirical observations such as a dielectric pad generally leading to a local increase in B_1^+, which means that the material is best used as close to the region of interest (ROI) as possible, and that higher permittivity materials should be considered at lower fields [2–4, 10]. Based on such a zero-order formulation, a higher ε_r should always be desirable. However, previous studies have shown that this is not the case [8]. The underlying reason for this discrepancy is related to electrical interactions, such as wavelength effects within the pad and body, which are not taken into account in a zero-order formulation. Moreover, because the equation is in a differential form, it can at most relate to local quantities (i.e., at the interface of the high permittivity material and the body). The description therefore remains limited in terms of providing a quantitative prediction of the B_1^+ field within the body. The necessity of a more elaborate understanding of the underlying mechanisms is further emphasized by the continuous increase in high permittivity materials available, some with $\varepsilon_r > 1000$ [13], which produce very strong effects that are likely to exceed the mechanisms described by the zero-order formulation. A better understanding of the underlying mechanisms is therefore required to manage these effects.

Optimizing the design of dielectric pads in terms of their geometry, composition, and placement remains a nontrivial task, because a closed-form solution of their effect has not been demonstrated. The most pragmatic approach so far has been to set up a series of electromagnetic simulations using commercial software for a limited set of configurations, from which the optimal solution is determined a posteriori based on a suitable performance measure [2, 3, 8, 9, 14]. This procedure can lead to long computation times, especially when multiple degrees of freedom (e.g., dimensions, position, material properties, etc) need to be addressed simultaneously, leading to a large set of configurations that need to be evaluated. In some cases, subject specificity may further increase the complexity of the design problem [9]. Some analytical formulations have been proposed that speed up field computation and can be used to analyze fundamental limits [15–20], but they fail to capture these practical design considerations because they do not incorporate a realistic body model. Accurate and efficient modeling methods are therefore highly desirable to improve the design procedure.

There is a vast literature on numerical techniques for the computation of electromagnetic fields in inhomogeneous dielectrics such as the human body. Local methods based on the partial differential form of Maxwell's equations, such as the finite-difference time-domain (FDTD) method, are known for their generality and versatility in many application areas. On the other hand, global methods that start from Maxwell's equations in integro-differential form, such as the integral equation method, offer great flexibility in exploiting certain problem properties by customization of the method (e.g., by reducing the problem to the relevant domain or by incorporating suitable approximations and a priori information). Furthermore, inverse scattering methods from remote sensing based on this formulation may provide a framework for developing a numerical method that can optimize the design of dielectric pads [21–23]. Preliminary work based on the integral equation method has been described for modeling the effect of a dielectric pad, by formulating this as an electromagnetic scattering problem in which the body model is used as a background model [24]. Some approaches in inverse scattering incorporate a priori knowledge such as a background model to formulate an initial estimate of the pertaining fields, while performing subsequent iterations using the free space Green's function. The background model can also be embedded into the Green's function, thereby directly accounting for its electromagnetic interactions at the cost of a more involved numerical procedure for evaluating the Green's function, since a closed-form solution is not available in case of an inhomogeneous background.

The first goal of the current study was to explore the physical mechanisms underlying dielectric shimming in terms of secondary fields and displacement currents when using two different high permittivity materials at 7T. These studies were performed using conventional three-dimensional (3D) electromagnetic simulation software. The second goal was to study the relevance of electrical interactions within the pad and within the body by comparing the zero-order approximation with full-wave results using the integral equation method in a two-dimensional (2D) configuration. Finally, this framework was used to develop an optimization method for the design of dielectric pads by solving the corresponding inverse problem. The particular illustrative application is neuroimaging at 7T, but the approach is applicable to all field strengths and configurations.

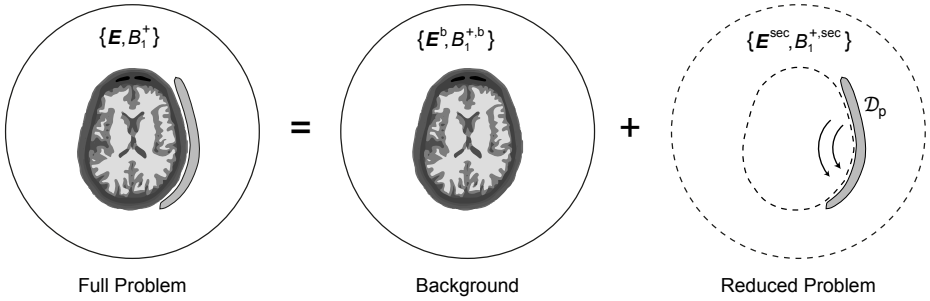

Figure 9.1: Decomposition of a dielectric shimming configuration. The total field $\{\boldsymbol{E}, B_1^+\}$ (left) is decomposed into a primary field produced in the background configuration $\{\boldsymbol{E}^{\mathrm{b}}, B_1^{+,\mathrm{b}}\}$ (without pad; center) and a secondary field $\{\boldsymbol{E}^{\mathrm{sec}}, B_1^{+,\mathrm{sec}}\}$ (right) produced by the currents induced in the dielectric pad radiating in the background configuration. This splits the full problem into a stationary part, which can be evaluated off-line, and a reduced problem confined to the dielectric pad domain $\mathscr{D}_{\mathrm{p}}$.

9.2. THEORY

The starting point for the integral equation method is to decompose the relevant components of the total field $\{\boldsymbol{E}, B_1^+\}$ into a primary field $\{\boldsymbol{E}^{\mathrm{b}}, B_1^{+,\mathrm{b}}\}$ and a secondary field $\{\boldsymbol{E}^{\mathrm{sec}}, B_1^{+,\mathrm{sec}}\}$, as follows:

$$\boldsymbol{E}(\boldsymbol{r}) = \boldsymbol{E}^{\mathrm{b}}(\boldsymbol{r}) + \boldsymbol{E}^{\mathrm{sec}}(\boldsymbol{r}) \tag{9.3}$$

$$B_1^+(\boldsymbol{r}) = B_1^{+,\mathrm{b}}(\boldsymbol{r}) + B_1^{+,\mathrm{sec}}(\boldsymbol{r})\,. \tag{9.4}$$

Here, $\boldsymbol{r} = (x, y, z)$ denotes the position vector. This decomposition is schematically illustrated in Fig. 9.1. The primary field is the field produced in the background configuration, which consists of a body model and possibly also a coil model, without any dielectric pads in place. The secondary field represents the field generated in the background configuration by the currents induced within the dielectric pad. We denote the spatial domain that encompasses the dielectric pad by $\mathscr{D}_{\mathrm{p}}$. Using integral equations, one can then write the total electric field $\boldsymbol{E}$ as

$$\boldsymbol{E}(\boldsymbol{r}) = \boldsymbol{E}^{\mathrm{b}}(\boldsymbol{r}) + \int\limits_{\boldsymbol{r}' \in \mathscr{D}_{\mathrm{p}}} \overline{\overline{\boldsymbol{G}}}^{\mathrm{b}}(\boldsymbol{r}, \boldsymbol{r}')\chi_{\mathrm{e}}(\boldsymbol{r}')\boldsymbol{E}(\boldsymbol{r}')\mathrm{d}V \tag{9.5}$$

where $\overline{\overline{\boldsymbol{G}}}^{\mathrm{b}}$ denotes the Green's tensor relating the electric current to electric field in the background configuration and $\chi_{\mathrm{e}}(\boldsymbol{r}) = (\varepsilon_{\mathrm{r}}(\boldsymbol{r}) - \varepsilon_{\mathrm{r}}^{\mathrm{b}}(\boldsymbol{r}))/\varepsilon_{\mathrm{r}}^{\mathrm{b}}(\boldsymbol{r})$ denotes the electric susceptibility of the total configuration, characterized by $\varepsilon_{\mathrm{r}}(\boldsymbol{r})$, with respect to the inhomogeneous background configuration, characterized by $\varepsilon_{\mathrm{r}}^{\mathrm{b}}(\boldsymbol{r})$. The Green's tensor $\overline{\overline{\boldsymbol{G}}}^{\mathrm{b}}$ represents the electric field radiated in the background configuration by an electric point source located in the pad domain $\mathscr{D}_{\mathrm{p}}$, which can be evaluated numerically as an off-line procedure. It should be noted that Equation (9.5) needs to be treated as an integral equation, which after discretization can be written as a system of linear equations and solved using iterative numerical methods. Obtaining a solution to Equation (9.5) for a given $\boldsymbol{E}^{\mathrm{b}}$ and χ_{e} is commonly referred to as the "forward problem."

Once the electrical interactions within the dielectric pad are solved for, the total B_1^+ field follows from the integral expression

$$B_1^+(\boldsymbol{r}) = B_1^{+,\mathrm{b}}(\boldsymbol{r}) + \int_{\boldsymbol{r}'\in\mathscr{D}_\mathrm{p}} \overline{\overline{\boldsymbol{G}}}^{+,\mathrm{b}}(\boldsymbol{r},\boldsymbol{r}')\chi_\mathrm{e}(\boldsymbol{r}')\boldsymbol{E}(\boldsymbol{r}')\mathrm{d}V \tag{9.6}$$

in which $\overline{\overline{\boldsymbol{G}}}^{+,\mathrm{b}}$ denotes the Green's tensor relating the electric current to the B_1^+ field in the background configuration. This means that propagation of B_1^+ in the background configuration is accounted for via $\overline{\overline{\boldsymbol{G}}}^{+,\mathrm{b}}$. We note that, once the total electric field $\boldsymbol{E}$ is known, Equation (9.6) can be directly evaluated with the minor computational cost of evaluating the associated matrix-vector product.

ZERO-ORDER APPROXIMATION

Approaches to solving Equation (9.5), and subsequently Equation (9.6), include the Neumann series expansion and the Born approximation [25]. Previous studies have indicated that these methods can model moderate field perturbations but diverge for higher permittivities [24]. In this study, we evaluated a modification of the Born approximation by neglecting the electrical interactions within the pad domain, which corresponds to the zero-order approximation as discussed in the Introduction. This amounts to setting $\boldsymbol{E} \approx \boldsymbol{E}^\mathrm{b}$ in Equation (9.6) as follows:

$$B_1^+(\boldsymbol{r}) \approx B_1^{+,\mathrm{b}}(\boldsymbol{r}) + \int_{\boldsymbol{r}'\in\mathscr{D}_\mathrm{p}} \overline{\overline{\boldsymbol{G}}}^{+,\mathrm{b}}(\boldsymbol{r},\boldsymbol{r}')\chi_\mathrm{e}(\boldsymbol{r}')\boldsymbol{E}^\mathrm{b}(\boldsymbol{r}')\mathrm{d}V \tag{9.7}$$

which is only strictly valid in the limit $\chi_\mathrm{e} \to 0$ but allows us to set apart the role of electrical interactions within the pad. We can also neglect the propagation in the background model by using the Green's tensor of free space, denoted by $\overline{\overline{\boldsymbol{G}}}^{+,0}$, for which an expression can be obtained using closed form analytical solutions [26]. This is written as

$$B_1^+(\boldsymbol{r}) \approx B_1^{+,\mathrm{b}}(\boldsymbol{r}) + \int_{\boldsymbol{r}'\in\mathscr{D}_\mathrm{p}} \overline{\overline{\boldsymbol{G}}}^{+,0}(\boldsymbol{r},\boldsymbol{r}')\chi_\mathrm{e}(\boldsymbol{r}')\boldsymbol{E}^\mathrm{b}(\boldsymbol{r}')\mathrm{d}V\,. \tag{9.8}$$

INVERSE PROBLEM FRAMEWORK

In contrast to the forward problem in which a solution to the field is sought for a given pad, the inverse problem is posed in the opposite direction; for a given field, a solution is sought in terms of the dielectric pad. The method is formulated by minimizing a cost function that measures the difference between a desired B_1^+ field and the actual B_1^+ field, which is referred to as the "target field error," by iteratively updating the permittivity distribution in the pad domain $\mathscr{D}_\mathrm{p}$. This cost function F is formulated as

$$F = \left\| B_1^+ - B_1^{+,\mathrm{target}} \right\|^2_{\mathscr{D}_\mathrm{ROI}}, \tag{9.9}$$

where $\mathscr{D}_\mathrm{ROI}$ denotes the ROI (i.e., the spatial domain for which the target field is specified) and B_1^+ depends on the product of χ_e and $\boldsymbol{E}$ as given by Equation (9.6). For fixed

values of the electric field $\boldsymbol{E}$, this function is minimized by updating the permittivity distribution via χ_e. The electric field, however, changes in tandem with updated values of χ_e as shown in Equation (9.5), which means that its values need to be updated as well. The expressions involved in updating χ_e are given in the Appendix.

9.3. METHODS

3D B_1^+ CHARACTERIZATION USING FDTD

3D field simulations of a 7T neuroimaging setup were performed using a commercial software package (xFDTD 7, Remcom Inc., State College, Pennsylvania, USA). The transmit coil was modeled as a 16-rung high-pass birdcage (inner diameter 30 cm; rung length 18 cm) with unit voltage sources with an impedance of 50 V, sinusoidal excitation at 300 MHz, and a 2π phase evolution along its circumference to simulate quadrature excitation in its homogeneous mode. The male body model "Duke" from the Virtual Family dataset was used [27].

A single dielectric pad was introduced on the left side of the head model with dielectric properties of either a calcium titanate ($CaTiO_3$) or a barium titanate ($BaTiO_3$) suspension. These suspensions have relative permittivity values of 110 and 286 and conductivity values of 0.11 S/m and 0.44 S/m, respectively, and have been used in previous neuroimaging studies at 7T [6–8, 11]. The dimensions of the pad were 18 × 18 cm with a thickness of 8 mm. All simulations were performed on a 4-mm isotropic grid.

2D MODELING USING THE INTEGRAL EQUATION METHOD

The integral equation method was implemented for a 2D TM-polarized configuration (electric field vector parallel to the invariance direction) of the neuroimaging setup with dielectric pad. A 2D approach was chosen to reduce the bookkeeping and computational complexity. This leads to an approximation of the fields that is reasonable in the central transverse plane of the coil [28], which is where the effects were analyzed. The inhomogeneous body model was incorporated into the background (hereinafter referred to as the "inhomogeneous background") as opposed to using a free space background. Interactions between the pad and the RF coil are assumed to be negligible (as described in more detail in the Discussion). The primary field (i.e., the field that is present in the background configuration without any pads in place) was generated by simulating a 30-cm-diameter circular array of 16 electric current line-sources, driven at a frequency of 300 MHz with a 2π phase evolution along its circumference, surrounding the transverse cross-section of the "Duke" head model [27]. The Green's tensors were constructed by computing the field response of the inhomogeneous background for all source locations within the pad domain. All computations using the 2D method were performed on a 4-mm isotropic grid using the iterative conjugate gradient method [26]. All customized software code was developed in MATLAB 8.0 (MathWorks, Natick, Massachusetts, USA) and run on a desktop computer: computations took less than 30 s, including all off-line procedures.

To illustrate the relevance of body propagation effects, the zero-order approximation was evaluated in the 2D configuration using either the Green's tensor of free space (Equation (9.8)) or the Green's tensor of the inhomogeneous background (Equation (9.7))

which accounts for the interactions with the body. In both cases, values for the electric field were taken from the primary field. As mentioned in the theory section, the zero-order approximation neglects electrical interactions within the dielectric pad; the relevance of these interactions is illustrated by comparison with full-wave results (Equation (9.6)).

DEVELOPMENT OF A 2D INVERSE DESIGN METHOD

The full-wave 2D integral equation method with inhomogeneous background was used to develop an inversion method in which the algorithm optimizes the design of a dielectric pad by iteratively updating the permittivity within the pad domain through the real part of χ_e via minimization of the target field error. Mathematical details on the update procedure are outlined in the Appendix. To avoid spurious results, we applied a positivity constraint by enforcing negative values of χ_e to zero after each update.

As a proof-of-concept, we evaluated the inversion method both with the free-space as well as the inhomogeneous background for a synthetic target field dataset. The target field was generated by simulating the 2D configuration with a lossless barium titanate pad of homogeneous permittivity ($\varepsilon = 286$). The resulting B_1^+ data in the body was then provided to the algorithm as a target field in complex form (i.e., magnitude and phase). The pad geometry was assumed to be known in advance, and the reconstructed permittivity was allowed to vary within this domain. The accuracy of the reconstruction result was evaluated by measuring the global error in the reconstructed permittivity as follows:

$$\mathrm{ERR}_\varepsilon = \frac{\left\| \varepsilon - \varepsilon^{\mathrm{true}} \right\|_{\mathscr{D}_\mathrm{p}}}{\left\| \varepsilon^{\mathrm{true}} \right\|_{\mathscr{D}_\mathrm{p}}}. \tag{9.10}$$

Experimental validation of the 2D inverse design method was performed in a cylindrical phantom. The phantom was 12 cm in diameter and 24 cm in length and had a measured relative permittivity of 78 and electrical conductivity of 0.9 S/m. The inversion method was set up to aim for a uniform B_1^+ magnitude of 1 µT, which is equal to the peak magnitude of the primary B_1^+ field, within a manually drawn ROI. The algorithm was adapted to handle the target B_1^+ field in magnitude form by transferring the B_1^+ phase of the previous iteration to the target field, which is a common procedure in RF shimming and RF pulse design [29]. Furthermore, the pad domain was defined as a layer of 6-mm thickness surrounding the phantom, in which the permittivity was allowed to vary. Because an inhomogeneous permittivity distribution is currently challenging to implement, a simplified version of the resulting profile was implemented using a homogeneous barium titanate suspension ($\varepsilon_r = 286$) to form a rectangular pad with a length equal to that of the phantom. The required width and position were determined by measuring the extent across which the optimized permittivity distribution was higher than a relative permittivity of 200. Although this approach is somewhat ad hoc, it allows for comparing simulated and experimental data. B_1^+ maps were acquired using the dual refocused echo acquisition mode sequence [30]. The spatial resolution was $2.5 \times 2.5 \times 5.0$ mm^3, the B_1^+ encoding tip angle 50° and the imaging tip angle 10°.

9.4. RESULTS

3D B_1^+ CHARACTERIZATION

Figure 9.2 shows the simulated (xFDTD) B_1^+ field distributions in a transverse cross-section through the head. The calcium titanate pad gives rise to a uniform increase of the B_1^+ in the vicinity of the pad, which is consistent with the zero-order formulation. On the other hand, the barium titanate pad, which has a much higher permittivity, leads to a much stronger but also asymmetric B_1^+ distribution in the anterior/posterior direction. This behavior clearly does not follow the zero-order formulation, which would suggest constructive B_1^+ elevation along the entire extent of the pad. From the magnitude of the secondary field, which is obtained as a complex subtraction of the primary B_1^+ field (without pad) from the total B_1^+ field with the dielectric pad, it can be seen that the calcium titanate pad introduces an evenly distributed secondary field. In addition, the phase difference with respect to the primary B_1^+ field is relatively small ($< 70°$) and, more importantly, rather uniform along the extent of the dielectric. This explains the uniform B_1^+ elevation in the vicinity of the pad. In contrast, the barium titanate pad introduces a secondary B_1^+ field that is asymmetric in magnitude but also features an asymmetric and larger phase difference with respect to the primary B_1^+ field, reaching almost 160° on the posterior side of the brain. Both terms account for the resulting anterior/posterior asymmetry observed in the total B_1^+ field distribution, with constructive interference on the anterior side and destructive interference at the posterior side.

Figure 9.3 illustrates the magnitude of the induced current density Ji in the transverse plane for the three configurations. As can be seen, the induced current density in the barium titanate pad is much stronger than in the calcium titanate pad. Furthermore, the calcium titanate pad supports a rather uniform current density, whereas the induced current density in the barium titanate pad is highly nonuniform. The asymmetric B_1^+ induced by the barium titanate pad also corresponds to the asymmetric induced current density with a strong intensity in the anterior part of the pad.

2D ANALYSIS USING THE INTEGRAL EQUATION METHOD

The 2D simulation results using the integral equation method are shown in Fig. 9.4, showing the secondary B_1^+ field for different levels of model complexity. The zero-order approximation, which does not account for electrical interactions within the pad, is shown both for the Green's tensor of free-space (Equation (9.8)) as well as the Green's tensor of the inhomogeneous background, which accounts for the body model (Equation (9.7)). Clearly, using the Green's tensor of free-space does not yield an accurate representation of the physical case but shows that the spatial structure of the secondary field is governed by the background model, with an increased magnitude close to the pad, and a decreased magnitude at further distance. This is evident since the body is close to the pad, and presents a substantial load to the secondary field. Finally, the full-wave solution (Equation (9.6)) shows the relevance of electrical interactions within the dielectric pad. In the calcium titanate pad, the zero-order approximation with inhomogeneous background was relatively accurate with deviations in the order of 10% in the corresponding total B_1^+ field (data not shown). In the barium titanate pad, however, the accuracy was insufficient and only the full-wave method captured the asymmetric mag-

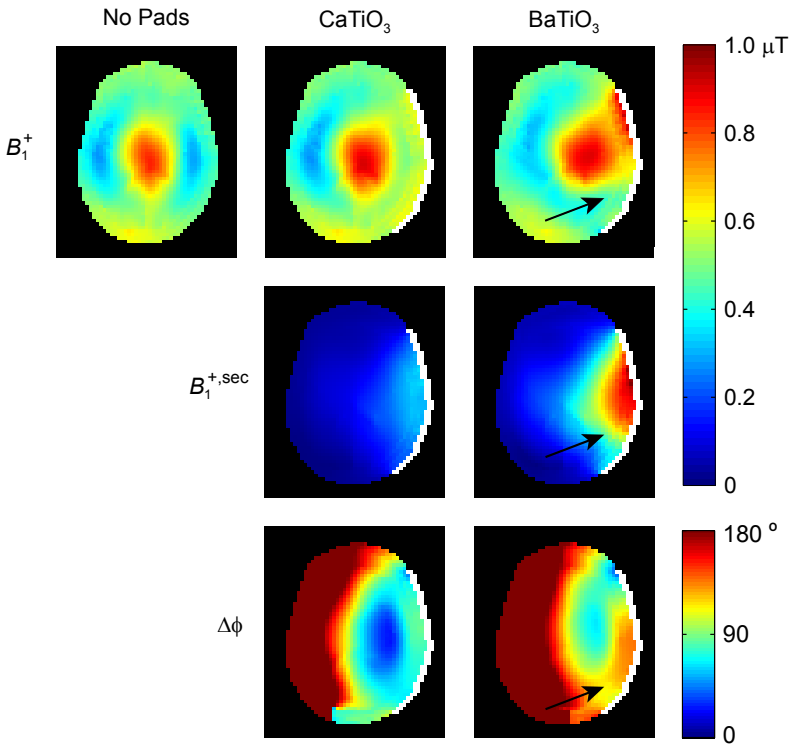

Figure 9.2: Effect of two different dielectric pads on the B_1^+ field. Shown are the 3D simulated transverse cross-sections of the total B_1^+ field (top) and the secondary B_1^+ field in magnitude (middle) and relative phase (bottom). The calcium titanate ($CaTiO_3$) pad induces a uniform increase of the B_1^+ close to the pad. Moving to barium titanate ($BaTiO_3$) introduces a strong anterior/posterior asymmetry in the total B_1^+ field (arrows), which is related to both the magnitude as well as the relative phase of the secondary B_1^+ field. The dielectric pads are shown in white.

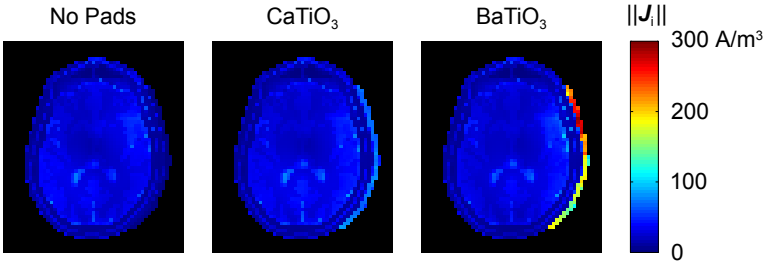

Figure 9.3: Magnitude of the induced current density Ji in the transverse plane, evaluated in the 3D configuration. The calcium titanate ($CaTiO_3$) pad supports a rather uniform induced current density, while the induced current density in the barium titanate ($BaTiO_3$) pad features a strong anterior/posterior asymmetry.

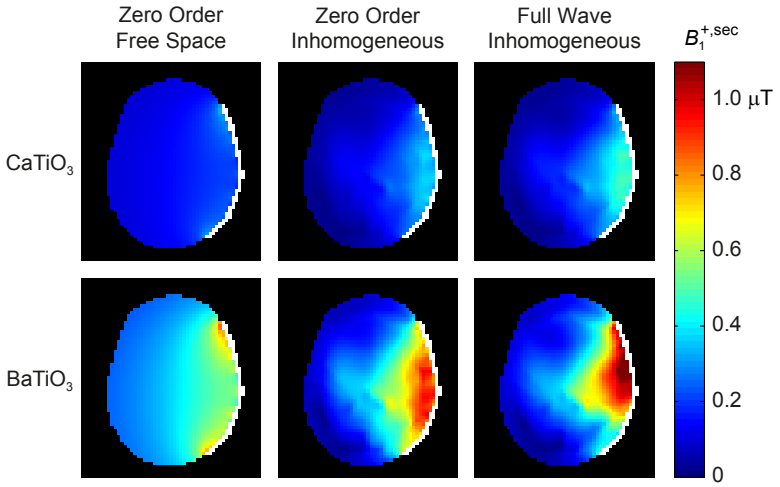

Figure 9.4: Approximations of the secondary B_1^+ field evaluated in the 2D configuration using the integral equation method. The zero-order approximation using either the free space (Equation (9.8)) or inhomogeneous background model (Equation (9.7)) shows the necessity of including body propagation effects. The full-wave method (Equation (9.6)) illustrates the relevance of electrical interactions within the pad, which become significant as the permittivity of the pad increases.

nitude profile as also shown in Fig. 9.2. The added benefit of using the inhomogeneous background in this case was observed in the convergence rate of the solver, which was improved approximately fivefold compared with the conventional 2D full-wave method based on a free-space background.

2D INVERSE DESIGN METHOD

Figure 9.5 shows the proof-of-concept inversion results using either the free space or the inhomogeneous background model. When using the free space background, the inversion method converged to the target field albeit with substantial errors in the reconstructed permittivity, which is reflected in a global permittivity error (Equation (9.10)) of $\mathrm{ERR}_\varepsilon = 12.5\%$. The accuracy of the reconstructed permittivity is much improved in the method based on the inhomogeneous background, with a global error of $\mathrm{ERR}_\varepsilon = 3.9\%$. The convergence of both inversion methods (Equation (9.9)) is shown in Fig. 9.6, which also reflects a much improved convergence rate of the latter method.

Figure 9.7 shows the inverse design results, in which the inversion method with inhomogeneous background was used together with the phase-updating scheme. The target field was defined as a uniform B_1^+ magnitude of 1 μT within a manually drawn ROI and the pad domain was defined as a continuous layer around the cylindrical phantom. Convergence was obtained within five iterations. The optimized dielectric was implemented as a homogeneous pad as shown in Fig. 9.8. The results indicate that the B_1^+ field can be tailored to an arbitrary ROI using the inversion method. Qualitative agreement with experimental B_1^+ maps demonstrates the validity of the method.

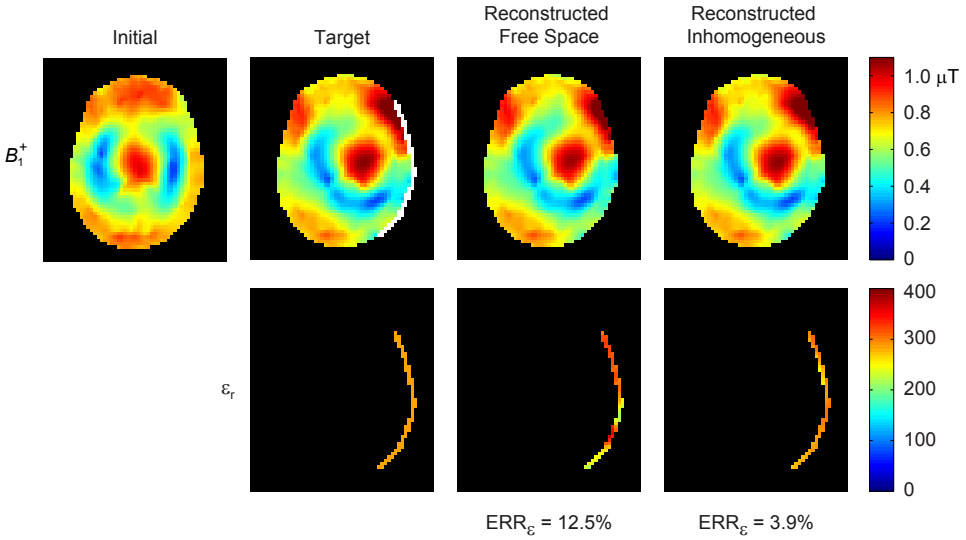

Figure 9.5: Proof-of-concept reconstruction results of the inversion method based on the free space or inhomogeneous background. The agreement between the reconstructed and true permittivity is much improved by using the inhomogeneous background, reducing the global permittivity error (Equation (9.10)) from $ERR_\varepsilon = 12.5\%$ down to $ERR_\varepsilon = 3.9\%$

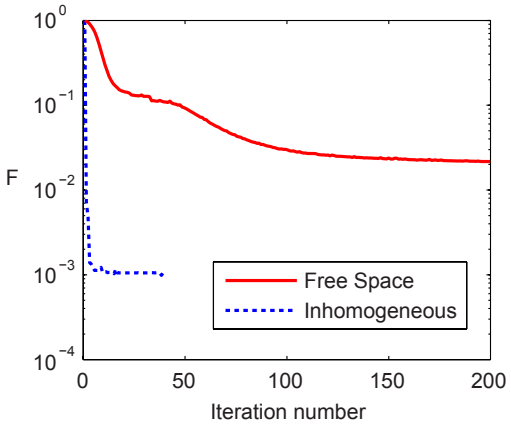

Figure 9.6: Convergence of the target field error in the proof-of-concept inversion experiment. By using the inhomogeneous background model, the inversion method requires many fewer iterations and reaches a lower target field error (Equation (9.9)).

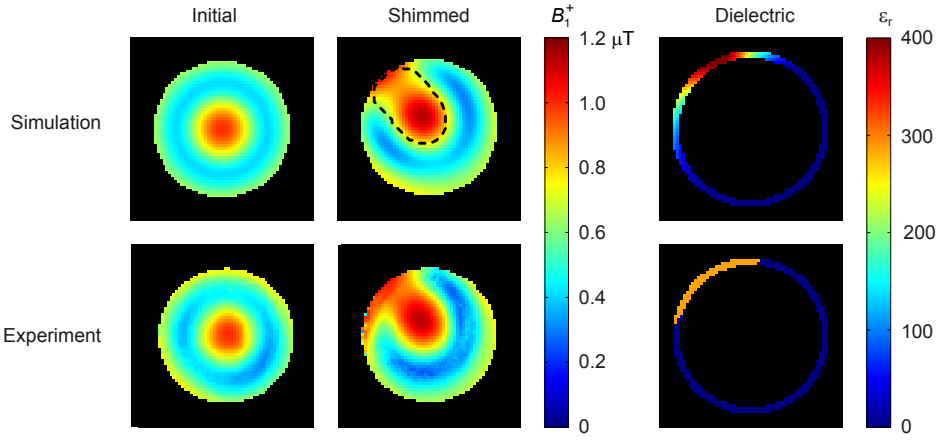

Figure 9.7: Experimental validation of the 2D Inverse design method in a cylindrical phantom. The method aims at obtaining a uniform B_1^+ magnitude of 1 μT within a manually drawn ROI (dashed line), by optimizing the permittivity distribution within a continuous layer surrounding the phantom. The optimized permittivity distribution was implemented as a homogeneous pad using barium titanate ($\varepsilon_r = 286$), its dimensions were obtained by truncating the optimized profile at $\varepsilon_r = 200$. Agreement with experimental B_1^+ maps demonstrates the validity of the method.

9.5. DISCUSSION

In this study, the effects of high permittivity materials on the RF field were analyzed using concepts from electromagnetic scattering. Whereas a calcium titanate pad gave a consistent elevation of the B_1^+ in its vicinity, a barium titanate pad with higher permittivity led to areas of high as well as low B_1^+ close to the pad. This effect can be attributed to the interference of a secondary magnetic field that is produced in the body by the currents induced in the dielectric pad, as embodied in the integral equation method with an inhomogeneous background. A full-wave model based on this formulation provides an efficient method for modeling these effects and improves the convergence of the inversion method substantially. This framework provides a promising starting point for tailored design of dielectric pads.

The scattering formalism applied here to dielectric shimming provides fundamental insight into the physical interactions that take place when a dielectric pad is inserted. Equation (9.6) states that a dielectric pad can be seen as a collection of equivalent currents, which radiate a secondary field into the background configuration. The expression indicates that, for a given electric field, the magnitude of the secondary B_1^+ field is related to both the permittivity as well as the volume of the pad. This relationship has been exploited previously to reduce the thickness of the dielectric pad by using materials with a higher permittivity [2, 7] or by tailoring the geometry of the pad for a given permittivity [3, 9]. However, a quantitative description of the effects cannot be based solely on Equation (9.6) and requires the electric field to be solved based on Equation (9.5). This is further illustrated using the zero-order approximation, which was shown to be reasonably accurate for low levels of electrical interactions, such as with the calcium titanate

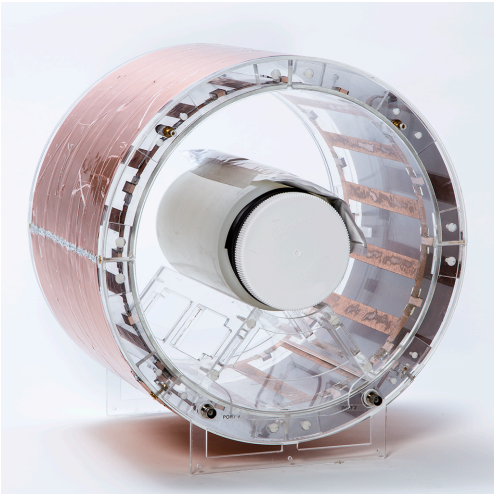

Figure 9.8: Experimental setup used to evaluate the 2D inversion method. The dielectric pad (shown in Fig. 7) is positioned on top of the cylindrical phantom.

pad, but does not account for potential wavelength effects within the pad, as was the case in the higher permittivity pad made of barium titanate. Only the full-wave method could model such effects accurately. This dependence can also be related to the dimensions of the pad with respect to the RF wavelength in the high permittivity material: in the calcium titanate pad, this is about 9.5 cm, whereas for the barium titanate pad it is 5.8 cm. In other words, a calcium titanate pad would also exhibit similar wavelength effects if a much larger pad size were to be considered.

The full-wave method based on the integral equations with inhomogeneous background simplifies the forward problem of computing the fields substantially, since the problem is reduced to resolving only the unknown electrical interactions within the dielectric pad itself, by accounting for all other interactions in an off-line stage. This was found to improve the convergence rate approximately fivefold in the 2D method and is expected to provide even greater improvements in a 3D method, since the relative size of the pad domain is then even smaller. An additional benefit of the approach is that the electric field strength within the heterogeneous body model is available at no additional computational cost. This improves the relevance of the method when compared with analytical methods, which do not allow for realistic evaluation of local SAR because they do not support a heterogeneous body model [31].

In addition to reducing the complexity of the forward problem, introducing the inhomogeneous background also reduces the ill-posedness of the associated inverse problem and provides additional insight into the nature of this optimization problem. Equation (9.6) indicates that designing dielectric pads can be thought of as designing an induced current density within the pad domain such that a desired secondary B_1^+ field is generated. These induced currents, however, are the result of passive electrical interactions within the pad and within the inhomogeneous background, which need to satisfy Maxwell's equations through Equation (9.5). The proposed method reduces the

complexity of both steps significantly, since the field decomposition (e.g., Equation (9.4) and 9.6) provides a direct relationship between the secondary B_1^+ field in the body and the induced currents in the pad domain. Furthermore, because updates of the induced current density are explicitly limited to the pad domain, the effective number of unknowns associated with the inverse problem is reduced significantly, thereby reducing its ill-posedness. The framework also indicates that the optimization problem is nonlinear in the sense that the electric field $\boldsymbol{E}$ and susceptibility χ_e are both unknown and occur as a product in Equation (9.6). This nonlinearity is illustrated in Fig. 9.5, where both algorithms converge to the target field even though not fully reconstructing the actual permittivity, reflecting the presence of local minima in the solution space. It is interesting to note that this property is fundamentally different from RF shimming using multiple independent sources (i.e., a transmit array), because in that case superposition can be applied, representing in principle a linear optimization problem.

In the current implementation of the proposed integral equation method, interactions between the dielectric pad and the RF coil have been neglected (i.e., the inhomogeneous background did not include the RF coil). This means that the Green's tensor only accounts for interactions between the dielectric pad and the body, which is reasonable when the body dominates these coupling effects, for instance in volume coils where the dielectric pad is close to the body and relatively small with respect to the size of the RF coil. This simplification could, however, pose limitations when the size or permittivity of the dielectric pad increases, or when it is positioned closer to the coils' conductors [14, 17]. In such a case, coupling between the dielectric pad and the coil may become significant, which means that the coil would need to be included in the background model in order to account for these effects. We note that in a practical setting, the coil would also be retuned, which effectively compensates for some of these interactions. Other limitations include the 2D approximation of the RF field. This approximation works well for longitudinal configurations, as shown in Fig. 9.7, but loses accuracy when considering for instance a dielectric pad with an axial extent that is short with respect to the RF coil. The method, however, can potentially be extended to 3D configurations in a similar manner, although requiring significant development due to the vectorial nature of the related integral equation [26]. Furthermore, in the inversion method, the permittivity was allowed to vary within the pad domain, which increases the degrees of freedom and flexibility of the algorithm but results in an inhomogeneous permittivity distribution that is more difficult to implement. In the current study, the optimized permittivity distribution was implemented by constructing a homogeneous pad instead; its geometry and position were set to match the area in which the optimized relative permittivity was 200 or higher. This is a very simple approach that is sufficient for the purpose of experimental validation, but the procedure can also be integrated in the algorithm by incorporating appropriate constraints on the permittivity [32, 33].

Finally, we note that the proposed framework is applicable to all field strengths and all dielectric shimming configurations. The method allows for incorporating a realistic body model and can account for dielectric pads of arbitrary shape and composition. This paves the way for exploiting the possibilities of dielectric shimming for addressing B_1^+ inhomogeneity in high field MRI.

APPENDIX A: UPDATING THE ELECTRIC SUSCEPTIBILITY χ_e

The update process of χ_e aims to iteratively minimize the target field error, which is measured through the cost function as given by Equation (9.9), repeated here for convenience:

$$F_n(\chi_{e,n}) = \left\| \rho_n(\chi_{e,n}) \right\|^2_{\mathscr{D}_{ROI}}. \tag{9.11}$$

Here, $\rho_n(\chi_{e,n}) = B_1^+(\chi_{e,n}) - B_1^{+,target}$ denotes the target field error and $\chi_{e,n}$ denotes the electric susceptibility at iteration n. The target field error is minimized by sequentially updating the electric susceptibility $\chi_{e,n}$ and updating the corresponding electric field $\boldsymbol{E}$ by solving a forward problem. The updates for $\chi_{e,n}$ are formulated using a gradient descend approach by defining a sequence of updates in χ_e as

$$\chi_{e,n} = \chi_{e,n-1} + \beta_n \nabla F_n \tag{9.12}$$

where ∇F_n denotes the gradient of the cost function with respect to χ_e, as follows:

$$\nabla F_n(\boldsymbol{r}) = \overline{\boldsymbol{E}(\boldsymbol{r})} \int_{\boldsymbol{r}' \in \mathscr{D}_p} \overline{\overline{\boldsymbol{G}}^{+,b}(\boldsymbol{r}, \boldsymbol{r}')} \rho_{n-1}(\boldsymbol{r}') \mathrm{d}V \tag{9.13}$$

where the overbar denotes a complex conjugate and the scalar step size β_n is obtained using line-minimization.

REFERENCES

[1] Yang QX, Wang J, Wang J, Collins CM, Wang C, and Smith MB. Reducing SAR and enhancing cerebral signal-to-noise ratio with high permittivity padding at 3 T. Magnetic Resonance in Medicine 2011; 65:358–362.

[2] de Heer P, Brink WM, Kooij BJ, and Webb AG. Increasing signal homogeneity and image quality in abdominal imaging at 3 T with very high permittivity materials. Magnetic Resonance in Medicine 2012; 68:1317–1324.

[3] Brink WM, and Webb AG. High permittivity pads reduce specific absorption rate, improve B1 homogeneity, and increase contrast-to-noise ratio for functional cardiac MRI at 3 T. Magnetic Resonance in Medicine 2014; 71:1632–1640.

[4] Yang QX, Rupprecht S, Luo W, Sica C, Herse Z, Wang J, Cao Z, Vesek J, Lanagan MT, Carluccio G, Ryu YC, and Collins CM. Radiofrequency field enhancement with high dielectric constant (HDC) pads in a receive array coil at 3.0T. Journal of Magnetic Resonance Imaging 2013; 38:435–440.

[5] Lindley MD, Kim D, Morrell G, Heilbrun ME, Storey P, Hanrahan CJ, and Lee VS. High-permittivity thin dielectric padding improves fresh blood imaging of femoral arteries at 3 T. Investigative Radiology 2015; 50:101–107.

[6] Snaar JEM, Teeuwisse WM, Versluis MJ, van Buchem MA, Kan HE, Smith NB, and Webb AG. Improvements in high-field localized MRS of the medial temporal lobe in humans using new deformable high-dielectric materials. NMR in Biomedicine 2011; 24:873–879.

[7] Teeuwisse WM, Brink WM, and Webb AG. Quantitative assessment of the effects of high-permittivity pads in 7 Tesla MRI of the brain. Magnetic Resonance in Medicine 2012; 67:1285–1293.

[8] Teeuwisse WM, Brink WM, Haines KN, and Webb AG. Simulations of high permittivity materials for 7 T neuroimaging and evaluation of a new barium titanate-based dielectric. Magnetic Resonance in Medicine 2012; 67:912–918.

[9] Brink WM, van der Jagt MA, Versluis MJ, Verbist BM, and Webb AG. High permittivity dielectric pads improve high spatial resolution magnetic resonance imaging of the inner ear at 7 T. Investigative Radiology 2014; 49:271–277.

[10] Luo W, Lanagan MT, Sica CT, Ryu Y, Oh S, Ketterman M, Yang QX, and Collins CM. Permittivity and performance of dielectric pads with sintered ceramic beads in MRI: early experiments and simulations at 3 T. Magnetic Resonance in Medicine 2013; 70:269–275.

[11] O'Brien KR, Magill AW, Delacoste J, Marques JP, Kober T, Fautz HP, Lazeyras F, and Krueger G. Dielectric pads and low- B1+ adiabatic pulses: complementary techniques to optimize structural T1w whole-brain MP2RAGE scans at 7 tesla. Journal of Magnetic Resonance Imaging 2014; 40:804–812.

[12] Yang QX, Mao W, Wang J, Smith MB, Lei H, Zhang X, Ugurbil K, and Chen W. Manipulation of image intensity distribution at 7.0 T: passive RF shimming and focusing with dielectric materials. Journal of Magnetic Resonance Imaging 2006; 24:197–202.

[13] Rupprecht S, Sica CT, Sahul R, Kwon S, Lanagan MT, and Yang QX. Drastic Enhancement and Manipulation of RF Field with Ultra High Dielectric Constant (uHDC) Material at 3T. In: Proceedings of the 21st Annual Meeting of ISMRM, Salt Lake City, UT, USA, 2013; p. 396.

[14] Oh S, Luo W, Zhang B, Deniz CM, Lanagan MT, Wiggins GC, and Collins CM. Maximized Local B1+ using Optimized Dielectric Pad at 7 T: Numerical Optimization and Experimental Validation. In: Proceedings of the 21st Annual Meeting of ISMRM, Salt Lake City, UT, USA, 2013; p. 4381.

[15] Jayatilake ML, Storrs J, Chu WJ, and Lee JH. Theoretical determination of the dielectric constant for passive RF shimming at high field. In: Proceedings of the 19th Annual Meeting of ISMRM, Montreal, Canada, 2011; p. 3887.

[16] Ketterman MD, Yang QX, Webb AG, Herse Z, Neuberger T, Carluccio G, and Lanagan MT. MRI Signal Enhancement via High-Permittivity Material Pads. In: Proceedings of the 21st Annual Meeting of ISMRM, Melbourne, Australia, 2012; p. 2699.

[17] Carluccio G, Oh S, Yang QX, Erricolo D, Luo W, and Collins CM. Near-Field Wave Impedance Matching with High-Permittivity Dielectric Materials for Optimum Transmittance in MRI Systems. In: Proceedings of the 21st Annual Meeting of ISMRM, Salt Lake City, UT, USA, 2013; p. 4374.

[18] Winkler SA, Sbrizzi A, van den Berg CAT, Luijten PR, and Rutt BK. Optimized Dielectric Shimming in High-Field Magnetic Resonance Imaging: A Theoretical Approach. In: Proceedings of the Workshop Scattering by Aggregates, Bremen, Germany, 2014; pp. 70–73.

[19] Lattanzi R, Vaidya MV, Carluccio G, Sodickson DK, and Collins CM. Effects of high-permittivity materials on absolute RF coil performance as a function of B0 and object size. In: Proceedings of the 22nd Annual Meeting of ISMRM, Milan, Italy, 2014; p. 4818.

[20] Lattanzi R, Vaidya MV, Carluccio G, Sodickson DK, and Collins CM. Signal-to-Noise Ratio gain at 3T using a thin layer of high-permittivity material inside enclosing receive arrays. In: Proceedings of the 22nd Annual Meeting of ISMRM, Milan, Italy, 2014; p. 4814.

[21] Abubakar A, Hu W, van den Berg PM, and Habashy TM. A finite-difference contrast source inversion method. Inverse Problems 2008; 24:1–17.

[22] Endo M, Čuma M, and Zhdanov MS. A multigrid integral equation method for large-scale models with inhomogeneous backgrounds. Journal of Geophysics and Engineering 2008; 5:438–447.

[23] Chen X. Subspace-based optimization method for inverse scattering problems with an inhomogeneous background medium. Inverse Problems 2010; 26:074007.

[24] Brink WM, and Webb AG. A forward model analysis of dielectric shimming in magnetic resonance imaging. In: Proceedings of the 15th Annual Meeting of ICEAA, Torino, Italy, 2013; pp. 528–531.

[25] Newton RG. Scattering Theory of Waves and Particles, 2nd ed. Dover Publications, 2013.

[26] Zwamborn P, and van den Berg PM. The Three-Dimensional Weak Form of the Conjugate Gradient FFT Method for Solving Scattering Problems. IEEE Transactions on Microwave Theory and Techniques 1992; 40:1757–1766.

[27] Christ A, Kainz W, Hahn EG, Honegger K, Zefferer M, Neufeld E, Rascher W, Janka R, Bautz W, Chen J, Kiefer B, Schmitt P, Hollenbach HP, Shen J, Oberle M, Szczerba D, Kam A, Guag JW, and Kuster N. The Virtual Family—development of surface-based anatomical models of two adults and two children for dosimetric simulations. Physics in Medicine and Biology 2010; 55:N23–38.

[28] van den Bergen B, Stolk CC, van den Berg JB, Lagendijk JJW, and van den Berg CAT. Ultra fast electromagnetic field computations for RF multi-transmit techniques in high field MRI. Physics in Medicine and Biology 2009; 54:1253–1264.

[29] Setsompop K, Wald LL, Alagappan V, Gagoski BA, and Adalsteinsson E. Magnitude least squares optimization for parallel radio frequency excitation design demonstrated at 7 Tesla with eight channels. Magnetic Resonance in Medicine 2008; 59:908–915.

[30] Nehrke K, Versluis MJ, Webb A, and Börnert P. Volumetric B1+ Mapping of the Brain at 7T using DREAM. Magnetic Resonance in Medicine 2014; 71:246–256.

[31] Collins CM, Li S, and Smith MB. SAR and B1 field distributions in a heterogeneous human head model within a birdcage coil. Magnetic Resonance in Medicine 1998; 40:847–856.

[32] Crocco L, and Isernia T. Inverse scattering with real data: detecting and imaging homogeneous dielectric objects. Inverse Problems 2001; 17:1573–1583.

[33] Abubakar A, and van den Berg PM. The contrast source inversion method for location and shape reconstructions. Inverse Problems 2002; 18:495–510.

CHAPTER 10

SUMMARY AND GENERAL DISCUSSION

10.1. SUMMARY

This thesis reports on the utility of high permittivity dielectric materials for adjusting the radiofrequency (RF) field in high field MR. The performance-driven trend towards higher static magnetic field strengths drives MR operation into the regime where the dimensions of the body section being imaged are comparable to the RF wavelength. This results in areas of constructive and destructive interference within the body, and associated variations in signal intensity and tissue contrast, which can severely reduce the diagnostic image quality [1]. However, the underlying electromagnetic interactions raise the question of whether these mechanisms may also be exploited to establish a remediation. This approach is termed "dielectric shimming," and is the subject of this thesis.

The first part of this thesis, comprising chapters 2 to 6, presents the evaluation and characterization of dielectric shimming in the context of a number of MR applications at 3T and 7T. Chapter 2 provides a review of dual-channel RF transmission at 3T and gives an overview of clinical applications where this technology has improved diagnostic image quality. The recent introduction of dual-transmit systems by most commercial vendors further emphasizes the clinical need for addressing RF uniformity at high fields.

In chapter 3 we present a quantitative comparison of dielectric shimming with respect to dual-channel RF shimming in functional cardiac imaging at 3T. Two dielectric pads were designed using electromagnetic simulations and implemented using a high permittivity suspension of barium titanate. A significant reduction in SAR, improved B_1^+ homogeneity and contrast-to-noise ratio was obtained with pads, outperforming dual-transmission ($n = 11$). The most consistent image quality was obtained when combining both techniques.

Chapter 4 extends the analysis of combined RF and dielectric shimming in cardiac imaging at 3T. The variation of B_1^+ homogeneity and SAR with respect to the full range of RF-shim settings was evaluated for five numerical body models and corroborated with RF-shim values obtained in vivo. The results indicate that the use of dielectric pads in combination with optimized RF-shim settings result in an improved B_1^+ homogeneity and reduced SAR, indicating the safety of this approach.

In chapter 5 the use of high permittivity pads is evaluated for imaging the thighs at 3T. The dielectric pads show to improve the transmit homogeneity of the body coil but compromise its receive homogeneity, which propagates into reconstruction algorithms in which the body coil is used as a reference for intensity correction. However, by measuring and correcting for the body coil reception profile this effect can be mitigated, leading to an improved image quality compared to the situation without dielectric pads.

Chapter 6 presents an evaluation of geometrically tailored dielectric pads for high spatial resolution imaging of the inner ear at 7T. Two gender-specific sets of dielectric pads were designed and implemented using a high permittivity suspension of barium titanate, which permitted a strong correction of the B_1^+ distribution while accounting for the constraints imposed by the tight-fitting receive coil. This lead to a significantly improved contrast homogeneity and increased diagnostic value ($n = 10$) without increasing local SAR, enabling further clinical evaluation of 7T MRI of the inner ear.

The second part of this thesis, which consists of chapters 7 to 9, discusses some fundamental aspects of RF inhomogeneity at high fields and theoretical aspects of dielectric shimming. Chapter 7 investigates different B_1^+ mapping techniques in the brain at 7T,

which often show residual anatomical structure from the ventricles. The origin of this local perturbation is shown to be partially related to the strong electrical conductivity of cerebrospinal fluid with respect to surrounding tissues, in addition to sequence specific MR effects.

Chapter 8 presents a numerical framework for modeling the field perturbation or "secondary field" generated by a dielectric shimming material. The integral equation method is taken as a starting point, and reformulated to explicitly include the inhomogeneous body model in the background. This reduces the computational domain to that of the dielectric pad, significantly improving the convergence of forward modeling schemes.

In chapter 9 an extended analysis of the integral equation method with inhomogeneous background is presented. The complex interference-effects that can occur during dielectric shimming with high permittivity materials are shown to be related to the phase difference between the primary and secondary B_1^+ field. Based on approximate solutions of the secondary field, we show that both the electrical interactions within the body as well as within the dielectric pad contribute to the observed effects. A simulation method based on this framework is then used to develop a design procedure which can provide guidelines for the tailored design of dielectric pads.

10.2. GENERAL DISCUSSION

The operation of MR requires a strong and uniform transmit RF field to obtain images that are free from artifacts. However, due to the shortening of the RF wavelength as field strength increases, spatial variations in the B_1^+ field amplitude occur and lead to a non-uniform tip angle distribution. Moreover, the increased electrical interactions lead to an increased power deposition, ultimately compromising the imaging speed in vivo.

Many groups have shown that B_1^+ homogeneity at high fields can be improved by means of parallel transmission (PTx). RF-shimming is a very common PTx technique in which the elements of transmit arrays are driven with independent phase and amplitude [2–5]. This approach was motivated theoretically by the fact that any RF field present within an object can be expanded in terms of a current distribution on its surface [6]. These ideas were developed with the prospect of using transmit arrays, however, the underlying equations do not differentiate the *origin* of such a surface current distribution. In other words, it may be generated *actively* by a transmit array, or induced *passively* in a dielectric material. This implies that there is no fundamental difference in the potential of dielectric shimming as opposed to using a transmit array, when considering the RF fields that can be generated. Indeed, simulation studies confirmed that by using dielectric pads in a single-channel 3T system, a B_1^+ homogeneity could be obtained similar to that of an eight-channel RF-shimmed body coil [7].

The main theoretical challenge in dielectric shimming is to determine how to induce such a desired current distribution within the dielectric, when this distribution also needs to satisfy Maxwell's equations as a passive reaction to an external field. An array of electrically-decoupled transmit elements in this context presents a well-controlled situation, since the principle of linear field superposition can be applied. This is not the case in dielectric shimming since the induced current density is in fact the result of electrical coupling between the fields and the material, and it is due to this coupling that the

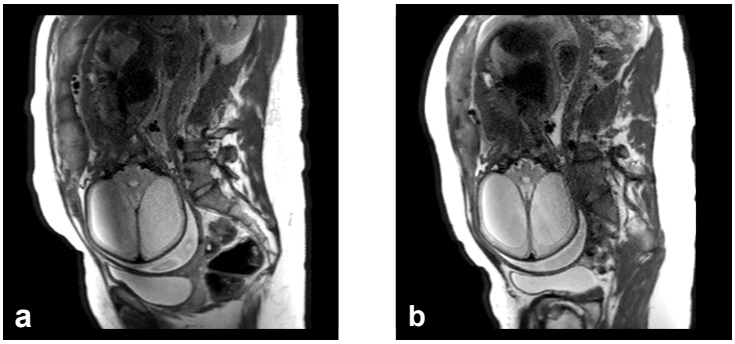

Figure 10.1: Clinical example of RF-shimmed fetal imaging using dual-channel B_1^+ shimming (**a**) and combined with dielectric pad (**b**).

underlying optimization problem is a nonlinear one. This means that the mathematical problem associated with the design of dielectric pads is fundamentally more complex, and no closed form solutions have been reported so far, if even tractable at all.

One obvious advantage of a PTx setup is that it allows for dynamic modulation of the instantaneous B_1^+ field via the individual waveforms, which allows for full spatiotemporal control of the MR excitation process. As a reciprocal of parallel imaging, the spatial sensitivity profiles of individual array elements can also be utilized for spatial encoding during the excitation process, which led to the concept of transmit SENSE [8]. Ultimately, such an approach imposes stronger requirements on the peak RF power and introduces a stronger variability and uncertainty in SAR. Much research effort is therefore invested in design algorithms to handle these degrees of freedom appropriately.

The main drawback of the flexibility offered in a PTx architecture is the more involved RF management that is required to operate such a flexible system. This includes multichannel RF calibration procedures, SAR prediction, safety monitoring as well as online RF pulse design. Although simulation studies indicate that PTx allows for acquiring relatively homogeneous images of the human brain at field strengths up to 14T [9], many of these practical issues need to be addressed before this can be translated into clinical practice. These additional overhead will increase system complexity significantly and inevitably translate into a higher system cost.

It is important to note that the efficiency of any PTx approach in the end depends on the transmit efficiency the decoupling of the individual elements, and in that respect the use of a dielectric material may still further improve the performance of a transmit array. Although the typical consideration for increasing the performance of a PTx system is to increase the number of channels [10, 11], the inclusion of a dielectric shim to add degrees of freedom may be much more cost-effective.

Dielectric materials may also yield an improved starting point for other homogenization approaches, reducing the "correction" that is needed. Combined RF and dielectric shimming was indeed shown to improve the power balance in a two-channel 3T system, as shown in chapter 4, as well as in simulations of an eight-channel system at 3T [7]. The performance of specialized RF pulses used to mitigate B_1^+ homogeneity can also be improved by providing a more homogeneous starting point [12, 13].

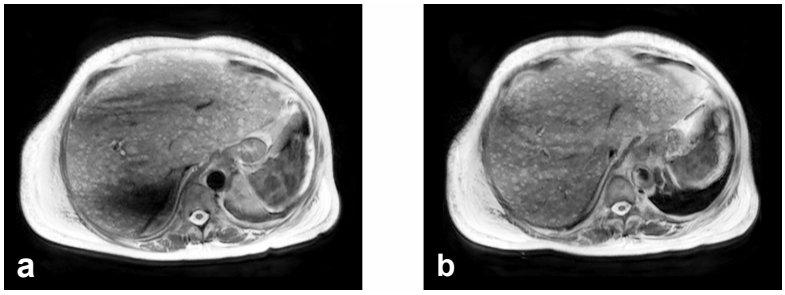

Figure 10.2: Clinical example of RF-shimming in abdominal imaging where RF shading artifacts remained despite of the use of dual-channel B_1^+-shimming (**a**). Combined with a dielectric pad on the posterior side significantly improved the contrast homogeneity (**b**).

Then even when RF-shimming is performed in a PTx system, artifacts can occur, for instance in body imaging using a dual-transmit system at 3T. A clinical example of RF-shimmed fetal imaging is shown in Fig. 10.1, where due to the very strong wavelength effects a strong inhomogeneity at the position of the fetus remains, despite the use of RF shimming. Placement of a high permittivity dielectric pad in this case improved the image quality substantially. Another example concerns that of a patient with hepatomegaly, where due to the enlarged liver strong wavelength effects occurred. This is shown in Fig. 10.2. Again, despite the RF-shim optimization, artifacts remained. Use of the dielectric pad positioned on the posterior side improved the RF shading substantially. The fact that these cases were underperforming is certainly related to the specific pathologies representing a more "extreme" subject as for which the RF-shimming routine is optimized, meaning that the specific design parameters such as the trade-off between SAR and homogeneity may be suboptimal in these cases. Combining both approaches improves this trade-off, as was also shown in chapter 4, further improving the system's robustness.

A final aspect which puts dielectric shimming into perspective is the fact that there are still over 500 clinical 3T systems in operation worldwide with no solution devised to the problem of RF shading. The use of dielectric materials therefore represents a relevant alternative for improving the imaging performance of a single-channel 3T system, for example in cases in which the financial resources are not available to upgrade to the much more expensive dual-transmit architecture.

10.2.1. CONCLUSIONS AND FUTURE PERSPECTIVES

The main conclusions from this thesis are that dielectric shimming presents a very simple and effective method for improving MR operation at high field strength. The high permittivity materials ($\varepsilon_r \approx 300$) allow for either homogenization or focusing of the B_1^+ field, without increasing SAR. The technique improves body applications at 3T as well as neuro applications at 7T, and theoretical foundations are presented to harness and exploit this approach. The obtained solutions are low-cost, vendor-independent, do not require any major hardware or software modifications and can therefore be very easily implemented in clinical protocols.

Finally, there are a number of areas where the approach of dielectric shimming could grow further.

- The development of dielectric materials with lower losses and lower weight can further improve patient comfort. As the losses in a dielectric pad reduce the magnitude of the induced current density, more material mass is needed to generate the desired correction. A higher permittivity may also improve this, however it is important to verify that the net weight does not increase.
- Efficient design methods are needed which harness the degrees of freedom available in dielectric shimming, to deduce appropriate design guidelines for new configurations and applications.
- The combined optimization of a dielectric shim together with PTx excitation may further reduce SAR and improve B_1^+ homogeneity. A dielectric shim could for instance be designed by taking the most SAR-efficient RF-shim setting as a starting point, as this was found to be only weakly affected by the dielectric. This may improve SAR intensive applications such fast-spin-echo (FSE) fetal imaging as well as high resolution prostate imaging at 3T.
- Another promising area is the integration of dielectric materials in receive-array coils. The increased coupling with local tissues by means of a dielectric has long been known to improve SNR of local receive coils, as was also shown in this thesis. However, geometrical optimization studies have so far been oriented towards volume transmit coils only, and this approach should be extended towards receive coil arrays as well.

REFERENCES

[1] Bernstein MA, Huston J, and Ward HA. Imaging artifacts at 3.0T. Journal of Magnetic Resonance Imaging 2006; 24:735–746.

[2] van den Berg CAT, van den Bergen B, van de Kamer JB, Raaymakers BW, Kroeze H, Bartels LW, and Lagendijk JJW. Simultaneous B1+ Homogenization and Specific Absorption Rate Hotspot Suppression Using a Magnetic Resonance Phased Array Transmit Coil. Magnetic Resonance in Medicine 2007; 57:577–586.

[3] Harvey PR, Zhai Z, Morich M, Mens G, van Yperen G, DeMeester G, Graesslin I, and Hoogeveen R. SAR Behavior During Whole-Body MultiTransmit RF Shimming at 3.0T. In: Proceedings of the 17th Annual Meeting of ISMRM, Honolulu, Hawaii, USA, 2009; p. 4786.

[4] Homann H, Graesslin I, Eggers H, Nehrke K, Vernickel P, Katscher U, Dössel O, and Börnert P. Local SAR management by RF Shimming: a simulation study with multiple human body models. Magnetic Resonance Materials in Physics Biology and Medicine 2012; 25:193–204.

[5] Shajan G, Kozlov M, Hoffmann J, Turner R, Scheffler K, and Pohmann R. A 16-channel dual-row transmit array in combination with a 31-element receive array

for human brain imaging at 9.4 T. Magnetic Resonance in Medicine 2014; 71:870–879.

[6] Hoult DI. Sensitivity and Power Deposition in a High-Field Imaging Experiment. Journal of Magnetic Resonance Imaging 2000; 12:46–67.

[7] Brink WM, and Webb AG. Transmit Strategies for Body Imaging at 3T - Comparing Multitransmit and Dielectric Shimming. In: Proceedings of the 21st Annual Meeting of ISMRM, Salt Lake City, UT, USA, Salt Lake City, 2013; p. 2800.

[8] Katscher U, Börnert P, Leussler C, and van den Brink JS. Transmit SENSE. Magnetic Resonance in Medicine 2003; 49:144–150.

[9] Cao Z, Park J, Cho ZH, and Collins CM. Numerical evaluation of image homogeneity, signal-to-noise ratio, and specific absorption rate for human brain imaging at 1.5, 3, 7, 10.5, and 14T in an 8-channel transmit/receive array. Journal of Magnetic Resonance Imaging 2015; 41:1432–1439.

[10] Childs AS, Malik SJ, O'Regan DP, and Hajnal JV. Impact of number of channels on RF shimming at 3T. Magma 2013; 26:401–410.

[11] Wu X, Zhang X, Tian J, Schmitter S, Hanna B, Strupp J, Pfeuffer J, Hamm M, Wang D, Nistler J, He B, Vaughan TJ, Ugurbil K, and de Moortele PFV. Comparison of RF body coils for MRI at 3 T: a simulation study using parallel transmission on various anatomical targets. NMR in biomedicine 2015; 28:1332–1344.

[12] O'Brien KR, Magill AW, Delacoste J, Marques JP, Kober T, Fautz HP, Lazeyras F, and Krueger G. Dielectric pads and low- B1+ adiabatic pulses: complementary techniques to optimize structural T1w whole-brain MP2RAGE scans at 7 tesla. Journal of Magnetic Resonance Imaging 2014; 40:804–812.

[13] Wezel J, Versluis M, Webb A, van Osch M, and Börnert P. Homogeneous neuroimaging at 7 tesla with short tailored radiofrequency pulses using high permittivity dielectric bags. In: Proceedings of the 22nd Annual Meeting of ISMRM, Milan, Italy, 2014; p. 1450.

NEDERLANDSE SAMENVATTING

Dit proefschrift behandelt het nut van diëlektrische materialen van hoge permittiviteit voor het aanpassen van de radiofrequente (RF) veldverdeling in hoogveld MRI. De door beeldkwaliteit gedreven trend naar hogere veldsterktes heeft MR gedreven tot de situatie waarin de afmetingen van het af te beelden lichaamsdeel vergelijkbaar zijn met de RF golflengte. Dit leidt tot gebieden van constructieve en destructieve interferentie binnen het lichaam, en daaraan gerelateerde variaties in signaalintensiteit en weefselcontrast, welke de diagnostische beeldkwaliteit ernstig kunnen verlagen. Evenwel roepen de hieraan ten grondslag liggende elektromagnetische interacties de vraag op of deze mechanismen ook benut kunnen worden om een oplossing te bewerkstelligen. Deze benadering heet "diëlektrisch shimmen," en is het onderwerp van dit proefschrift.

Het eerste deel van dit proefschrift, bestaande uit de hoofdstukken 2 tot en met 6, presenteert de evaluatie en karakterisering van diëlektrisch shimmen in de context van een aantal MR toepassingen op 3T en 7T. Hoofdstuk 2 begint dit deel met een technische beschouwing van twee-kanaals RF transmissie op 3T en overzicht van de klinische toepassingen waarin deze technologie de diagnostische beeldkwaliteit heeft verbeterd. De recente introductie van twee-kanaals systemen door de voornaamste leveranciers van MR systemen benadrukt het klinische belang om tot een oplossing te komen ten aanzien van RF homogeniteit op hoge veldsterktes.

In hoofdstuk 3 presenteren we een kwantitatieve vergelijking van diëlektrisch shimmen met twee-kanaals RF shimmen in functionele cardiovasculaire beeldvorming. Twee diëlektrische kussens zijn ontworpen met behulp van elektromagnetische simulaties en geïmplementeerd middels een hoge permittiviteits suspensie van bariumtitanaat. Een significante verlaging van de SAR, verbeterde B_1^+ homogeniteit en contrast-ruisverhouding was verkregen met de kussens, welke de prestaties van het twee-kanaals systeem overtroffen ($n = 11$). De meest consistente beeldkwaliteit was verkregen door beide technieken te combineren.

Hoofdstuk 4 verlengt de analyse van het gecombineerd RF en diëlektrisch shimmen in cardiovasculaire beeldvorming op 3T. De variatie in B_1^+ homogeniteit en SAR binnen het volledige bereik aan RF-shim instellingen is geëvalueerd aan de hand van vijf numerieke lichaamsmodellen en bevestigd met in vivo metingen. De resultaten geven aan dat het gebruik van diëlektrische kussens in combinatie met geoptimaliseerde RF-shim instellingen leidt tot een verbeterde B_1^+ homogeniteit en verlaagde SAR, wat de veiligheid van deze benadering aangeeft.

In hoofdstuk 5 is het gebruik van diëlektrische kussens van hoge permittiviteit geëvalueerd voor het afbeelden van het bovenbeen op 3T. De diëlektrische kussens verhogen aantoonbaar de zendhomogeniteit van de RF lichaamsspoel maar dit gaat ten koste van zijn ontvangsthomogeniteit, wat propageert in reconstructiealgoritmes die de lichaamsspoel gebruiken als referentie voor intensiteitscorrectie. Echter, dit effect kan worden opgeheven door het ontvangstprofiel van de lichaamsspoel te meten en hier-

voor te corrigeren, wat resulteert in een verhoogde beeldkwaliteit ten opzichte van de situatie zonder diëlektrische kussens.

Hoofdstuk 6 beschrijft de evaluatie van geometrisch aangepaste diëlektrische kussens voor het op hoge resolutie afbeelden van het binnenoor op 7T. Twee paar geslachtsspecifieke kussens zijn ontworpen en geïmplementeerd met een hoge-permittiviteits suspensie van bariumtitanaat, welke een sterke correctie van de B_1^+ verdeling mogelijk maakt binnen de beperkingen opgelegd door de strak omsluitende ontvangstspoel. Dit leidt tot een significant verbeterde contrast homogeniteit en verhoogde diagnostische waarde ($n = 10$) zonder de lokale SAR te verhogen, wat verdere klinische evaluatie van 7T MRI van het binnenoor mogelijk maakt.

Het tweede deel van dit proefschrift, bestaande uit de hoofdstukken 7 tot en met 9, behandelt een aantal fundamentele aspecten van RF inhomogeniteit op hoge veldsterktes en theoretische kanten van diëlektrisch shimmen. Hoofdstuk 7 onderzoekt verschillende methoden voor het afbeelden van de B_1^+ verdeling in het brein op 7T, welke regelmatig resterende anatomische structuur van de ventrikels laten zien. De oorsprong van deze lokale verstoring wordt aangetoond gedeeltelijk gerelateerd te zijn aan de hoge elektrische geleiding van hersenvocht ten opzichte van de omliggende weefsels, naast MR effecten die afhangen van de specifieke acquisitiemethode.

Hoofdstuk 8 presenteert een numerieke opzet voor het modelleren van de veldverstoring of "secundaire veld" welke gegenereerd wordt door een diëlektrisch shim materiaal. De integraalvergelijkingsmethode vormt het startpunt, en wordt herschreven om het inhomogene lichaamsmodel expliciet in de achtergrond op te nemen. Dit reduceert het rekengebied tot dat van het diëlektrische kussen, wat de convergentie van voorwaartse modelleringsmethoden significant verbetert.

In hoofdstuk 9 wordt een verdere analyse van de integraalvergelijkingsmethode met inhomogene achtergrond gepresenteerd. De complexe interferentie effecten die kunnen optreden tijdens het diëlektrisch shimmen met materialen van hoge permittiviteit kunnen worden verklaard aan de hand van de faseverschillen tussen het primaire en secundaire B_1^+ veld. Een simulatiemethode gebaseerd op deze formulering wordt vervolgens gebruikt om een ontwerpmethode te ontwikkelen die richtlijnen kan leveren voor het op maat maken van diëlektrische kussens.

LIST OF PUBLICATIONS

JOURNAL PUBLICATIONS

1. Teeuwisse WM, **Brink WM**, and Webb AG. Quantitative assessment of the effects of high-permittivity pads in 7 Tesla MRI of the brain. Magnetic Resonance in Medicine 2012; 67:1285–1293.

2. Teeuwisse WM, **Brink WM**, Haines KN, and Webb AG. Simulations of high permittivity materials for 7T neuroimaging and evaluation of a new barium titanate based dielectric. Magnetic Resonance in Medicine 2012; 67:912–918.

3. de Heer P, **Brink WM**, Kooij BJ, and Webb AG. Increasing signal homogeneity and image quality in abdominal imaging at 3T with very high permittivity materials. Magnetic Resonance in Medicine 2012; 68:1317–1324.

4. **Brink WM**, and Webb AG. High permittivity pads reduce specific absorption rate, improve B_1 homogeneity, and increase contrast-to-noise ratio for functional cardiac MRI at 3T. Magnetic Resonance in Medicine 2014; 71:1632–1640.

5. **Brink WM**, van der Jagt MA, Versluis MJ, Verbist BM, and Webb AG. High permittivity dielectric pads improve high spatial resolution magnetic resonance imaging of the inner ear at 7T. Investigative Radiology 2014; 49:271–277.

6. **Brink WM**, Börnert P, Nehrke K, and Webb AG. Ventricular B_1^+ perturbation at 7T - real effect or measurement artifact? NMR in Biomedicine 2014; 27:617–620.

7. van der Jagt MA, **Brink WM**, Versluis MJ, Steens SCA, Briaire JJ, Webb AG, Frijns JHM, and Verbist BM. Visualization of human inner ear anatomy with high-resolution MR imaging at 7T: initial clinical assessment. American Journal of Neuroradiology 2015; 36:378–383.

8. **Brink WM**, Gulani V, and Webb AG. Clinical applications of dual-channel transmit MRI: A review. Journal of Magnetic Resonance Imaging 2015; 42:855-869.

9. **Brink WM**, Remis RF, and Webb AG. A theoretical approach based on electromagnetic scattering for analysing dielectric shimming in high-field MRI. Magnetic Resonance in Medicine 2015; *in press.*

10. Oudeman J, Coolen BF, Mazzoli V, Maas M, Verhamme C, **Brink WM**, Webb AG, Strijkers GJ, and Nederveen AJ. Diffusion-prepared neurography of the brachial plexus with a large field-of-view at 3T. Journal of Magnetic Resonance Imaging 2015; *in press.*

11. **Brink WM**, van den Brink JS, and Webb AG. The effect of high-permittivity pads on specific absorption rate in radiofrequency-shimmed dual-transmit cardiovascular magnetic resonance at 3T. Journal of Cardiovascular Magnetic Resonance 2015; 17:82.

12. **Brink WM**, Versluis MJ, Peeters JM, Börnert P, and Webb AG. Passive radiofrequency shimming in the thighs at 3 Tesla using high permittivity materials and body coil receive uniformity correction. Magnetic Resonance in Medicine 2015; *in press*.

CONFERENCE PROCEEDINGS

1. **Brink WM**, and Webb AG. Improvements in Cardiac MRI at 3T using High Permittivity Materials. In: Proceedings of the 21st Annual Meeting of ISMRM, Salt Lake City, UT, USA, 2013; p. 1400.

2. **Brink WM**, and Webb AG. Transmit Strategies for Body Imaging at 3T - Comparing Multitransmit and Dielectric Shimming. In: Proceedings of the 21st Annual Meeting of ISMRM, Salt Lake City, UT, USA, 2013; p. 2800.

3. **Brink WM**, Börnert P, Nehrke K, and Webb AG. Ventricular B_1 Enhancement - Truth or Fiction? In: Proceedings of the 21st Annual Meeting of ISMRM, Salt Lake City, UT, USA, 2013; p. 2592.

4. **Brink WM**, and Webb AG. Electromagnetic Analysis of Dielectric Shimming using High Permittivity Materials. In: Proceedings of the 21st Annual Meeting of ISMRM, Salt Lake City, UT, USA, 2013; p. 4375.

5. **Brink WM**, and Webb AG. A forward model analysis of dielectric shimming in magnetic resonance imaging. In: Proceedings of the 15th Annual Meeting of ICEAA, Torino, Italy, 2013; pp. 528–531.

6. **Brink WM**, van den Brink JS, and Webb AG. Implications of Dielectric Pads on Dual-Transmit SAR Behaviour. In: Proceedings of the 23rd Annual Meeting of ISMRM, Milan, Italy, 2014; p. 321.

7. **Brink WM**, and Webb AG. Appearant B_1^+ Asymmetry in Symmetric Objects at 7T. In: Proceedings of the 23rd Annual Meeting of ISMRM, Milan, Italy, 2014; p. 4815.

8. **Brink WM**, and Webb AG. Integral Equations Based Modeling Approach to Dielectric Shimming. In: Proceedings of the 23rd Annual Meeting of ISMRM, Milan, Italy, 2014; p. 4831.

9. **Brink WM**, Versluis MJ, Peeters JM, Börnert P, and Webb AG. Considerations for Parallel Imaging when using High Permittivity Pads in the Thighs at 3T. In: Proceedings of the 23rd Annual Meeting of ISMRM, Toronto, Canada, 2015; p. 2426.

10. **Brink WM**, Noureddine Y, Kraff O, Bitz AK, and Webb AG. RF Safety Validation of High Permittivity Pads at 7 Tesla. In: Proceedings of the 23rd Annual Meeting of ISMRM, Toronto, Canada, 2015; p. 3108.

CURRICULUM VITÆ

Wyger Brink was born in Berghem on May 10, 1987. After graduating from the Titus Brandsma Lyceum in Oss in 2005, he continued his studies in Electrical Engineering at the Delft University of Technology. In 2010, he finished his master degree in Telecommunications with distinction, after writing his master thesis on electromagnetic focused hyperthermia. In 2011, he persued his Ph.D. degree at the Leiden University Medical Center in the field of MRI in the group of prof.dr. Andrew Webb which resulted in this thesis. He is currently appointed as postdoctoral researcher at the same group to persue further developments in dielectric shimming and applied electromagnetic in the context of MRI, in collaboration with the Delft University of Technology.

Wyger Maurits Brink

10-05-1987 Born in Berghem, the Netherlands

EDUCATION

1999–2005 Grammar school, Titus Brandsma Lyceum in Oss

2005–2010 Electrical Engineering at the Delft University of Technology
Major in Telecommunications, with distinction (cum laude)
Thesis: Non-Invasive Electromagnetic Ablation of Female Breast Tumors

2011–2015 PhD researcher at the Leiden University Medical Center
Thesis: Dielectric Shimming – Exploiting Dielectric Interactions in High Field MRI

2015 Postdoctoral researcher at the Leiden University Medical Center

AWARDS

2013 ISMRM Merit Award Magna Cum Laude
Abstract: Improvements in Cardiac MRI at 3T using High Permittivity Materials

2013 ISMRM Merit Award Magna Cum Laude
Abstract: Ventricular B_1 Enhancement - Truth or Fiction?

2014 1st Place Poster Presentation at the ISMRM High Field Systems & Applications Study Group
Abstract: Integral Equations Based Modeling Approach to Dielectric Shimming

ACKNOWLEDGEMENTS

The results described in this thesis conclude four years of constructive research at the C.J. Gorter Center. Being part of this group has been a great joy and this is due to the contributions and support of many individuals.

First I would like to express my gratitude to my promotor Andrew. Thank you for the opportunity to grow in this research as a member of your group. Your down-to-earth approach on research is very inspiring, your engagement in research is remarkable and very supporting. Thank you for being such an open leader to the group.

The second warm voice coming from the other side of the hallway would be that of Peter. Peter, you have a keen eye on having 'fun' in research and your presence and curiosity has been a true positive driving force to me. Thank you for your constructive reviews on these manuscripts, your guidance and support, and thank you for stepping up as copromotor during my PhD.

I also would like to thank Wouter for taking me up initially, training me in and around the scanner and in the lab, and for all support throughout these years. Maarten, thank you for your continued consultation, troubleshooting and help when unraveling various mysteries of the scanner. Your input has always been very valuable to me.

Berit, many thanks for proofreading this thesis. Your enthusiasm and engagement with the C.J. Gorter Center truly stimulates clinical research at 7T. Annerie, thanks for all help and time spent together scanning, analyzing, processing, anonymizing.

Rob, thanks for your availability these past years, your help and support on various topics. Jeroen, I'm very glad you have joined our team of Maxwellians and I look forward to taking many more steps together with you advancing this field!

I also thank all other members of the Gorter Center for all support as well as positive distractions in the form of afternoon drinks and social events. Nathalie, thanks for making our room feel like 'home' when returning at the lab. Sophie, thanks for all your support both in contacting volunteers for the group as well as sharing your creations both individually as well as next to the coffee machine. Hermien, thanks for keeping an eye on me, sharing ideas and experiences on this unknown profession of parenting. Itamar and Carson, thanks for sharing a glimpse of the art of diffusion weighted spectroscopy. Melissa, Matthijs and Paul, thanks for initiating various trips abroad.

A special thanks to Maarten for all his time and effort spent on designing the front cover. This really finishes the thesis in style!

I also want to thank my family and friends for many precious moments and memories. In specific I thank my parents who supported our stay in Delft and fostered new possibilities. Thank you Jurre and Mara for being such a joy to raise, and for preserving your parents precious night time. Finally, I thank Anthilde for her endless patience, tolerance, love and support.